

OPEN JOURNAL OF

NANAN



ISSN:2147-0081

Volume:9, Issue: 1, Year: 2024

A JOURNAL ABOUT
NANOSCIENCE

Open Journal of Nano

Editor in Chief

Dr. Mustafa CAN, Sakarya University of Applied Sciences, Turkey
mustafacan@subu.edu.tr

Editorial Board

Dr. Emrah ÖZAKAR, Ataturk University,
Erzurum, Turkey.
emrahozakar@atauni.edu.tr

Dr. Hamza ŞİMŞİR, Karabuk University,
Turkey.
hamzasimsir@karabuk.edu.tr

Dr. Harun GÜL, Sakarya University of
Applied Sciences, Turkey.
harungul@subu.edu.tr

Dr. Mustafa Zahid YILDIZ, Sakarya
University of Applied Sciences, Turkey.
mustafayildiz@sakarya.edu.tr

Dr. Numan GÖZÜBENLİ, Harran
University, Turkey.
gnuman@harran.edu.tr

Dr. Oğuz SARIBIYIK, Gümüşhane
University, Gumushane, Turkey.
oysaribiyik@gumushane.edu.tr

Dr. Tuğrul ÇETİNKAYA, Sakarya
University, Turkey.
tcetinkaya@sakarya.edu.tr

Dr. Yasin AKGÜL, Karabuk University,
Turkey.
yasinakgul@karabuk.edu.tr

Field Editors

Dr. Hasan HACİFAZLIOĞLU, İstanbul
University-Cerrahpaşa, İstanbul, Turkey.
hasanh@istanbul.edu.tr

Dr. Mithat ÇELEBİ, Yalova University,
Turkey.
mithat.celebi@yalova.edu.tr

Dr. Zafer Ömer ÖZDEMİR, University of
Health Sciences, Turkey.
zaferomer.ozdemir@sbu.edu.tr

Dr. Erol ALVER, Hitit University, Turkey.
erolalver@hitit.edu.tr

Dr. Kamal YUSOH, University Malaysia
Pahang, Malaysia.
kamal@ump.edu.my

Dr. Tetiana TEPLA, Lviv Polytechnic
National University, Ukraine.
tetiana.l.tepla@lpnu.ua

Dr. Birgül BENLİ, İstanbul Technical
University, Turkey.
benli@itu.edu.tr

Dr. Deniz ŞAHİN, Gazi University, Turkey.
dennoka1k@hotmail.com

Statistics Editor

Dr. Özer UYGUN, Sakarya University,
Sakarya, Turkey.
ouygun@sakarya.edu.tr

Open Journal of Nano

Editorial Assistants

Mücahid SARI, Sakarya University of Applied Sciences, Sakarya, Turkey.
<https://dergipark.org.tr/en/pub/@mucahidsari>

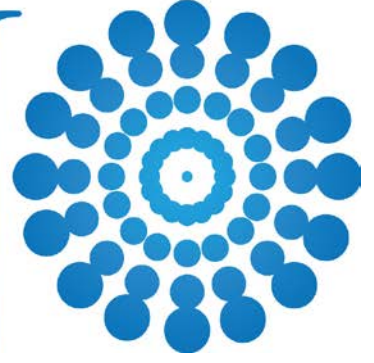
Dr. Hamza ŞİMŞİR, Karabuk University, Turkey.
hamzasimsir@karabuk.edu.tr

Engin Deniz PARLAR, Sakarya University of Applied Sciences, Sakarya, Turkey. denizparlar-97@hotmail.com

Nadir ATMACA, The Istanbul Metropolitan Municipality, Istanbul, Turkey.
nadiratmaca@gmail.com

Halid ÖZGÜR, FreshForty Media, Turkey
halid@freshforty.media

Enis AKSOY, Areya illüstrasyon, Sakarya, Turkey
enisaksoy@gmail.com

**Contents****Volume: 9, Issue: 1, Year: 2024****Colloidal Silica Production with Resin from Sodium Silicate and Optimization of Process**
(Research Article) 01-10Buse AKKAYA, Jiyan ASLAN, Rukiye TAŞDEMİR, İlker ERDEM, **Mehmet GÖNEN****City of Bacteria**
(Review Article) 11-21
Nurdan FİLİK, Fethi FİLİK**Structural, Morphological and Magnetic Investigation of Half-Doped La_{0.5}Ba_{0.5}MnO₃ Perovskite Nanoparticles**
(Research Article) 22-34
Yusuf SAMANCIOĞLU**Development Of Aluminum Matrix Rgo Reinforced Composites By Electric Current Assisted Sintering**
(Elektrik Akım Destekli Sinterleme Yöntemiyle Alüminyum Matrisli Rgo Takviyeli Kompozitlerin Geliştirilmesi) 35-44
(Araştırma Makalesi)
Yakup PEHLİVAN, Harun Gül**Blood Glucose Level Estimation Using Photoplethysmography (PPG) Signals with Explainable Artificial Intelligence Techniques**
(Review Article) 45-62
Gökhan ADİGÜZEL, Ümit ŞENTÜRK, Kemal POLAT**Sonochemical Removal of Highly Toxic Aqueous Cd²⁺ and Cr⁶⁺ Ions Using Dandelion-like Co₃O₄ Nanoflowers**
(Arratum) 63-76
Elif Aybike BERBEROĞLU, Mümin Mehmet KOÇ, Nurdan Kurnaz YETİM, **Cemile ÖZCAN**



Colloidal Silica Production with Resin from Sodium Silicate and Optimization of Process

¹Buse AKKAYA , ¹Jiyan ASLAN , ¹Rukiye TAŞDEMİR , ²İlker ERDEM , *¹Mehmet GÖNEN 

¹ Süleyman Demirel University, Chemical Engineering Department, Isparta, Türkiye
² Abdullah Gül University, Nanotechnology Engineering Department, Kayseri, Türkiye

* Corresponding author, e-mail: mehmetgonen@sdu.edu.tr

Submission Date: 09.11.2023

Acceptation Date: 01.01.2024

Abstract - Colloidal silica is a stable and homogeneously dispersed form of amorphous silicon dioxide (SiO₂) nanoparticles in water. Colloidal silica has been the focus of research due to large surface area, biocompatibility, low toxicity and chemical and thermal stability. It has been used in a wide variety of industrial applications, including pulp and paper, chromatography, electronics, foods, and colloids, as well as in the ceramics and glass industry. In this study, colloidal silica was produced using cationic resin and sodium silicate and process conditions were optimized. Temperature (50-80 °C), mixing speed (200-500 rpm) and time (20-120 min.), which significantly affect the particle size, were selected as parameters. Particle size distribution (PSD) analyzes of colloidal silica particles were performed to determine appropriate levels of the parameters. The most suitable process conditions are 50°C temperature, 40 min. and 300 rpm. The average particle size of colloidal silica produced in optimum conditions was measured as 80 nm.

Keywords: Colloidal Silica, Optimization, Sodium Silicate, Particle Size

1. Introduction

Silica and silica-derived materials are widely used in the glass, ceramics and silicon industries due to their availability and easy recovery. Colloidal silica, generally known as silica sol used as a term corresponding to a stable distribution of amorphous silica particles. Silica sols first synthesized in 1861 by Graham who investigated the production of dilute silica sol by dialysis by adding hydrochloric acid to an aqueous solution of sodium silicate. Silica sol including 10% SiO₂ was marketed for the first time in 1933 [1]. Colloidal silica is the form of amorphous silicon dioxide nanoparticles in the range of 1-100 nm, distributed in a stable and homogeneous manner in water. Sodium silicates, unlike colloidal silica, consist of silicate monomers. Sodium silicates have a SiO₂/Na₂O ratio of approximately 2.0-3.4. The SiO₂/Na₂O ratio of colloidal silica is greater than 50. Sodium silicate solutions having 3 modules are commonly used in colloidal silica production. Reactions used in the chemical preparation of colloidal silica can be divided into three main groups: reduction-oxidation reaction, hydrolysis of salts and ion displacement reactions [2].

Colloidal silica particles have many advantageous properties such as almost spherical shaped particles and narrow size distribution. However, it is one of the least understood systems due to the complexity of the physical and chemical nature of the surface. Although, there are Si-O-H and Si-O-Si functional groups on the colloidal silica surface, the distribution and amount of groups have a significant effect on the surface charge and structure [3]. The interest in research on colloidal silica, an inorganic and nanoparticulate structured material, stems from its numerous advantages, including its large surface area, low toxicity, apparent biocompatibility, optical transparency, chemical, thermal and colloidal stability [4]. Colloidal silica has been used for many years in a wide variety of industrial applications such as chromatography, healthcare, paper and pulp, electronics, foods, gels and colloids, as well as in the ceramics and glass industry [3-5]. Its current usage areas have expanded and it can be used as a coating material for various core materials, as drug carriers, as a support material for

¹ Corresponding author phone: 90-505-8130355

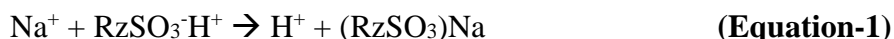
E-mail: mehmetgonen@sdu.edu.tr

biosensors and catalysts, and as an additive for paints-varnishes-coatings with the surface modification of colloidal silica [6-7].

Colloidal silica is widely used in the casting industry in the production of ceramic molds, in the construction industry in concrete production, in thermal insulation, in the paper industry to ensure the non-slip properties of paper, in the paint industry to increase the scratch resistance of the paint applied to the surface, and in the beverage industry as a clarifying agent to ensure clarity. SiO₂ content of colloidal silica used in the industry changes between 15-50% and the particle size varies between 5-60 nm. When the colloidal silica use increased in novel application areas, products with different particle size distributions are needed in those areas [8]. The main producers of colloidal silica in the world market are in countries, including the United States, Germany, Japan and China. Considering the production data of 2012, commercial silica production has a market value of 3.6 billion US dollars with a production of 2.4 million tons [1].

To produce colloidal silica different methods have been suggested such as sol-gel method, hydrothermal reaction and chemical vapor deposition (CVD) [9]. However, colloidal silica can be synthesized by hydrolysis and condensation of Tetraethyl orthosilicate (TEOS) or Tetramethyl orthosilicate (TMOS) known as polymeric sol-gel method, peptization silica gel or powder, oxidation of silicon powder and electro dialysis of hydrous silicates [7-10]. The sol-gel method having the advantage of controlling particle size and morphology by systematic control of reaction parameters at ambient temperature is widely used. Colloidal silica can be produced from sodium silicate solution by ion exchange method without using expensive starting materials and emitting toxic wastes [11-9]. The ion-exchange method has the advantages of being the most used process and being able to control the particle size and distribution. However, the regeneration of ion exchange resins is seen as a significant problem in financial and environmental terms. In addition, any Na ions remaining in the product may reduce the purity and stability of the colloid [7].

The ion exchange method is a process in which sodium ion is removed from liquid sodium silicate solution by using an ion exchange resin. Liquid sodium silicate is used as starting material by diluting to 2-6 %wt SiO₂ content. Active silicic acid is produced by removing sodium ions from diluted sodium silicate solution by passing it through cation exchange resin column [10]. Colloidal silica is produced industrially from sodium silicate solution [4]. Sodium ion is removed from diluted sodium silicate by passing it through ion-exchange cationic resin and active silicic acid is produced [6]. The ion exchange reaction between sodium ions and hydrogen ions of the cation exchange resin takes place as shown in Eqn.-1 [5].



In equation 1, SiO₃H is the sulfonic acid group and Rz is the styrene-divinyl benzene copolymer. Since the ionic bond strength of sodium ion is stronger than that of a hydrogen ion, it is easily replaced by sodium ions in water glass solution [11]. The silica sol then forms a dilute silica sol via nucleation from active silicic acid. It includes the stages of growing acid and discrete silica particles by polymerization and concentrating the dilute silica sol [1-10]. Different raw materials can be used in the production of colloidal silica. Examples of these materials include silicon metals, ethyl silicate, silicon tetrachloride, silica powder and sodium silicate [1]. Sodium silicate is generally preferred as a starting material in the industry due to its lower cost compared to other silicates available on the market [8]. Also, colloidal silica produced by the ion exchange method have homogeneous particles, higher silica content, and lower residual sodium ions [11]. In general, colloidal silica is stable in the pH range of 10-11, and the gelation time is short in the pH range of 3-8. Therefore, before using the colloidal silica in some new applications, its surface must be modified, especially if it is going to be used in the acidic range [12]. Although extensive research has been carried out on the production of colloidal silica, studies are still being carried out to determine the stability of the silica sols produced. Tsai, 2004 [13] produced colloidal silica by using a continuous

process column via sodium silicate. Differently, in our study, colloidal silica was produced in a batch process by using the separated part of the starting material as appropriate to industrial production, diluted sodium silicate, instead of KOH, without the need for the use of additional materials.

In this study, colloidal silica was produced from sodium silicate solution using ion exchange method. Before running the experiments, the amount of ion exchange resin was determined by measuring pH of the solution. Temperature (50-80 °C), mixing speed (200-500 rpm) and time (20-120 min.), which affect significantly particle size, were selected as parameters and they were optimized. PSD analyses of colloidal silica particles were performed to determine appropriate levels of the parameters. Formed products were characterized by using XRD and FTIR analyses.

2. Materials and Methods

2.1. Materials

In this study, sodium silicate ($\text{Na}_2\text{O} \cdot 3\text{SiO}_2$ having Na_2O , 8%; SiO_2 , 27%, Özkimsan) and Purolite C160H cation exchange resin were used as received without any treatment. The regeneration process was carried out using HCl (37%, Merck). Deionized water was used for all experiments.

2.2. Methods

The sodium silicate solution was diluted with deionized water to obtain a solution having 3% SiO_2 . The prepared dilute sodium silicate solution was divided into two parts by volume in a ratio of 1:7. The excess volume was treated with ion exchange resin to obtain active silicic acid. pH of the solution was measured at certain periods during the ion exchange process to determine the optimum amount of resin. The 40 g of resin was used in all experiments after determining the minimum resin required that lowers the pH to the range of 2-3. The mixture was filtered under vacuum of 700 mmHg to separate the resin from the solution. pH was measured at regular intervals by adding active silicic acid solution to the slightly dilute sodium silicate solution allocated at the beginning. Thus, because of the nucleation and growth of silica particles, colloidal silica formation was achieved in the stable pH range (pH=10-11). To concentrate the colloidal silica, mixture was evaporated by heating for a certain period of 20-120 min., at different temperatures of 50-80 °C and at stirring rate of 200-500 rpm. The used Purolite C160H cation exchange resin was regenerated by using 2 M HCl to exchange Na^+ ions to H^+ ions and reuse of the resin in the ion-exchange process [11]. A block diagram used for colloidal silica production was shown in Figure 1. Particle size analyses of colloidal silica samples prepared under above parameters were performed. The most suitable production conditions of colloidal silica nanoparticles were determined.

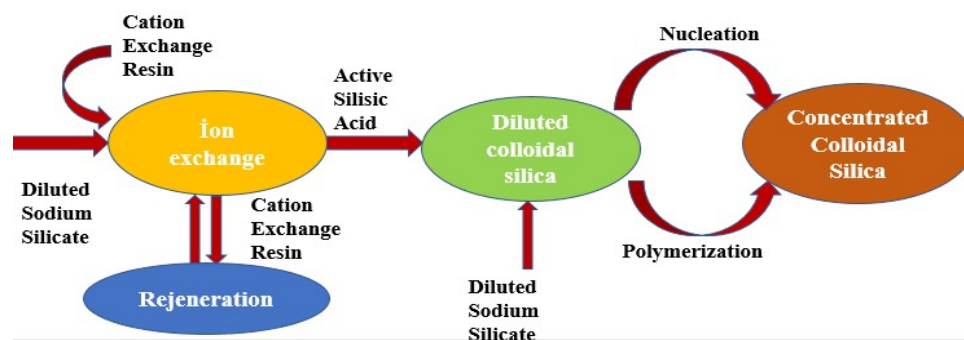


Figure 1. Block diagram of colloidal silica production process.

2.3. Characterization

Investigation of the amorphous structure of colloidal silica samples was investigated by using X-ray diffraction diffractometer (XRD) (BRUKER D8 ADVANCE TWIN-TWIN). Fourier transform infrared (FTIR) spectrum of silica nanoparticles were obtained by using FTIR spectrometer (FT/IR-4700 typeA). Solid silica particles after the drying at 105°C was examined in FTIR spectroscopy and XRD. In the study, the particle size distribution (PSD) analysis was performed by dynamic laser light scattering technique (Nano ZS, Malvern Co. UK). Before PSD analyzes samples were used by shaking the briefly in a tube shaker. Three readings were made for each sample and the average results were recorded.

3. Results and Discussions

Infrared spectroscopy is a characterization method used to analyse organic or inorganic compounds qualitatively and quantitatively. It is used to determine the chemical bonds in the molecule with the absorption peaks that occur because of the vibration of the bonds between the atoms that make up the substance [14].

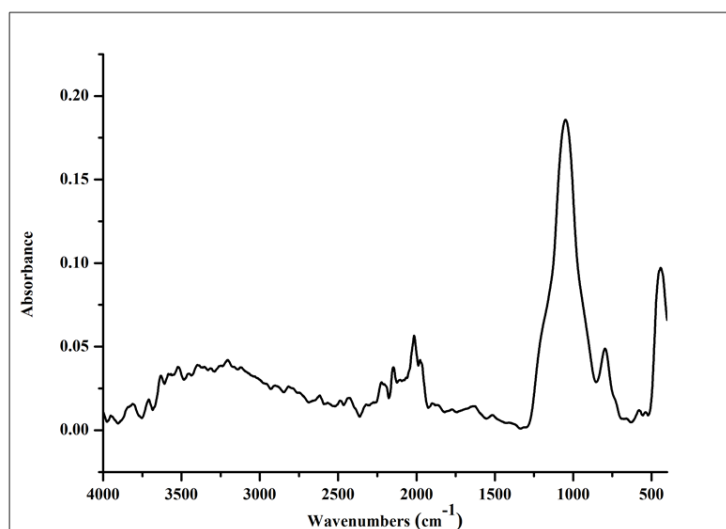


Figure 2. FTIR spectrum of colloidal silica.

The FTIR spectrum of the produced colloidal silica is given in Figure 2. FTIR spectrum of colloidal particles consists of asymmetric vibrations of Si–O 1090 cm^{-1} and Si–O–Si 1080 cm^{-1} [15], peaks arising from the asymmetric vibration of Si–OH (950 cm^{-1}) [16]. These peaks are overlapping in the spectrum shown in Fig. 2. In the absorption band, the peak of the symmetric vibration of Si–O is seen at 795 cm^{-1} . Absorption bands between $850\text{--}1260\text{ cm}^{-1}$ are defined as the overlap of various SiO₂ peaks and peaks arising from Si–OH bonds [17]. An intense characteristic absorption band was observed between $3000\text{--}3800\text{ cm}^{-1}$, which is assigned to the hydrogen bonds and O–H stretching of water. Additionally, this band is supported by the shear bending vibration of molecular water seen around 1635 cm^{-1} [17].

XRD is the most suitable characterization method to study the crystal structure of mesoporous materials and colloidal materials. The sample to be analysed is usually in the form of fine-grained powders. XRD analysis of crystalline compounds shows a diffraction pattern consisting of a narrow and prominent peak. Amorphous materials, on the other hand, do not form clear peaks. Instead, it produces spotted peaks or short rows of bumps in the diffraction pattern [1].

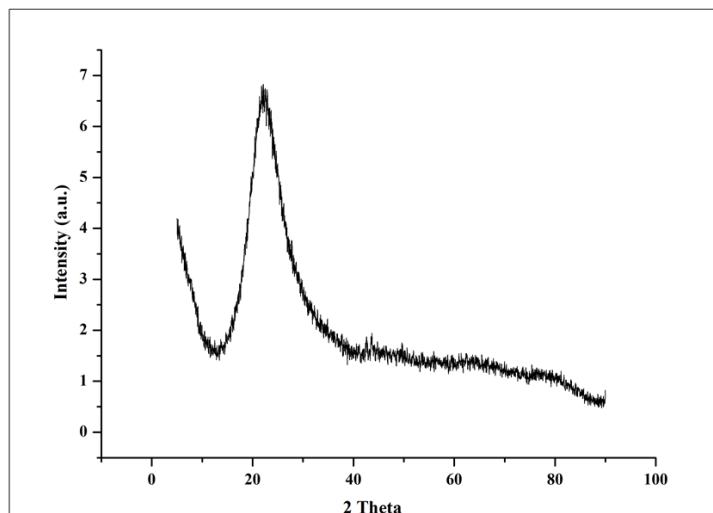


Figure 3. XRD spectrum of solid product obtained from colloidal silica.

As depicted in Figure 3 shows a broad peak observed between 15-30° at the 2θ angle confirms the amorphous nature of colloidal silica [16-18]. An amorphous peak was seen at 2θ = 21.8° [16]. They reported that the amorphous peak of colloidal silica was observed at 2θ = 21.8° [19], and in their study where they produced amorphous silica with the sol-gel procedure, they stated that the amorphous peak was recorded at 2θ = 23° at the end of the heat treatment.

The pH change versus resin amount during the formation of active silicic acid during the ion exchange process is given in Figure 4. The amount of resin to be used is determined as 40 g from the chart.

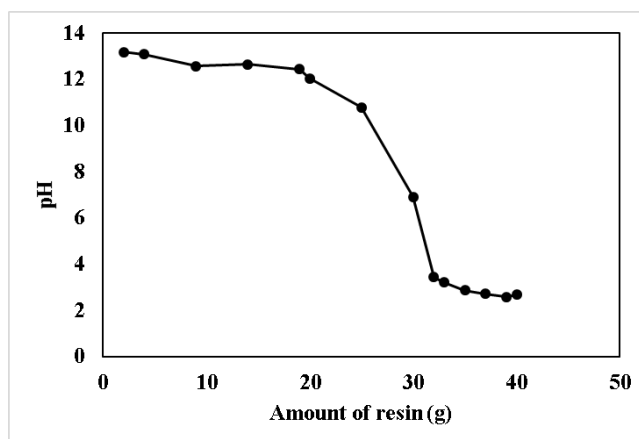


Figure 4. pH change for different amounts of resin during the formation of active silicic acid.

By adding active silicic acid solution onto dilute sodium silicate, colloidal silica formation was achieved in the stable pH range (pH = 10-11) [19] as a result of the nucleation and growth of silica particles. Generally, colloidal silica is stable in the pH range of 10-11. Colloidal silica, which is unstable in the pH range of 3-8, has a short gelation time [6]. To concentrate the colloidal silica, heating was carried out for a certain period (20-120 min.) at different temperatures (50-80 °C) with stirring of (200-500 rpm). Experiments were carried out at 4 different levels with time, mixing speed and temperature parameters using sodium silicate solution and cationic resin. Average particle size distribution analyses of the produced colloidal silica samples were performed and the change in particle size distribution of colloidal silica in response to heating time is given in Figure 5.

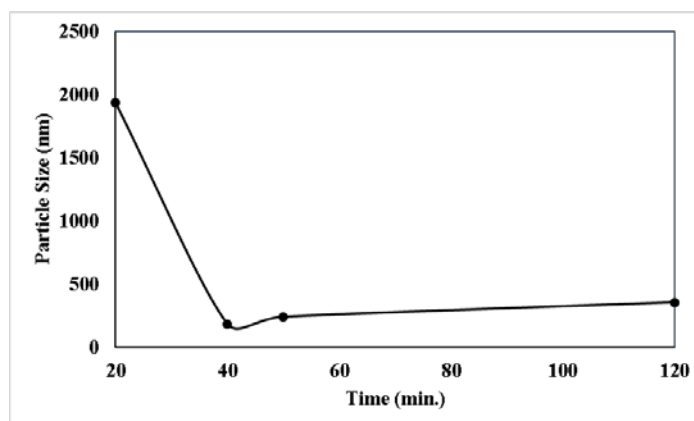


Figure 5. Particle size distribution of colloidal silica produced in different times.

As seen in Figure 5, the particle size corresponding to 20 minutes of heating time has the highest value. As a result of the sudden growth of colloidal silica produced over time, unstable particles larger than the desired particle size were formed. Minimum particle size was determined at 40 minutes as 184 nm for the colloidal silica obtained. After the heating period, the increase in time caused the particle size to increase. In line with these data, it was observed that the value closest to the desired particle size was obtained at 40 minutes of heating.

The temperature range to be used for colloidal silica production was chosen as 50-80 °C. It has been stated that when temperatures exceed 80 °C, deterioration occurs in the amorphous structure of SiOHs in colloidal silica. It has been determined that colloidal silica produced below 50 °C gels because it is not in a stable structure. Figure 6 shows the change in particle size distribution of the produced colloidal silica with temperature.

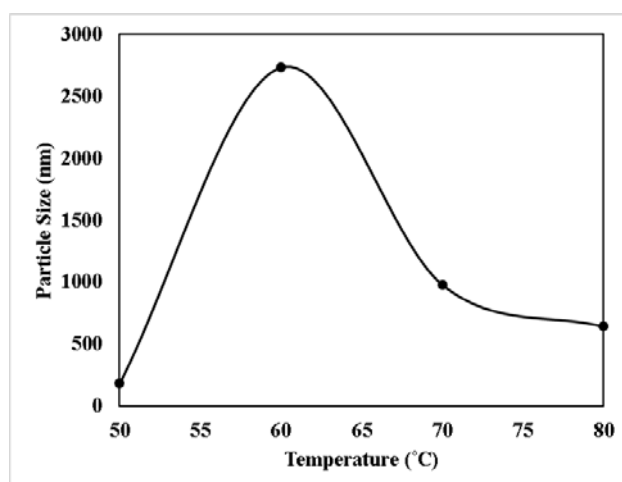


Figure 6. Particle size distribution of colloidal silica produced at different temperatures.

It has been determined that as the temperature increases, the particle size of the produced colloidal silica increases and moves away from the reported particle size range [20]. As it was stated that the addition of alkaline (pH = 8-10.5) at moderate temperature, colloidal silica was produced at a temperature of at least 60 °C to ensure nucleation, polymerization and particle growth [21]. Thus, a stable dilute colloidal silica solution is formed. In this study, concentrated colloidal silica was produced by investigating the duration of the heat treatment process. A temperature of 60 °C increased polymerization and particle growth occurred with the rising temperature. The reason for the decrease in particle size above 70 °C may be that hydrolysis and condensation proceed much faster, leading to the formation of secondary particles. The temperature dependence of particle growth is related to changes in hydrolysis and nucleation rate, which decrease significantly with lowering the reaction temperature. Higher temperatures in alkaline regions increase Ostwald ripening of colloidal silica and



coarsening of particles. Thus, smaller particles accumulate and combine on larger particles to form larger aggregates [22].

Table 1. Experimental data for optimization of colloidal silica process conditions.

Experiment	Concentration % wt.	Temperature (°C)	Heat. Time (min)	Mixing Speed (rpm)	Av. Part. Size (d.nm)	pH
1	3	50	50	200	242	10.5
2	3	50	120	200	357	10.6
3	3	50	20	200	1935	10.6
4	3	50	40	500	1081	10.4
5	3	50	20	400	460	9.8
6	3	50	20	300	205	9.9
7	3	50	40	200	184	10.4
8	3	50	40	300	80	10.4
9	3	50	40	400	7027	10.7
10	3	80	40	200	642	9.7
11	3	70	40	200	981	9.5
12	3	60	40	200	2735	10.3

When the average particle sizes of colloidal silica samples are compared in Table 1, the most suitable process conditions for the sample having the lowest particle size are 50°C temperature, 40 minutes of heating and 300 rpm stirring rate. Particle size analysis of colloidal silica produced under these conditions is given in Figure 7-a and Figure 7-b, based on volume and intensity, respectively. Analysis of particle size distribution and average particle size were performed. The smallest average particle size was obtained in experiment 8. The highest one was occurred in experiment 9. This result shows that lower mixing speed leads to a lower average particle size [7].

Particle size analysis results of 3% colloidal silica samples prepared at four different mixing speeds at 50 °C are included. According to these results, it was determined that colloidal silica samples prepared at mixing speed of 400-500 rpm had the highest particle size. Particle size analysis of the colloidal silica sample prepared at a stirring speed of 300 rpm is within the colloidal silica particle size range previously stated [1].

Colloidal silica is obtained by stably dispersing solid silica particles in water in the particle size range of 4-100 nm [4]. When the average particle sizes of colloidal silica samples are compared, the most suitable process conditions for the sample with the lowest particle size are 50°C temperature, 40 min. heating time and 300 rpm stirring rate.

While the volumetric distribution results are proportional to the 3rd power of the particle diameter (D^3), the size distribution displayed based on intensity is proportional to the 6th power of the diameter (D^6), so the relatively large particles in the suspension can be seen more clearly in the intensity-based distribution. When the size distribution by volume given in Figure 7a is examined, the average particle size of colloidal silica produced under the most suitable process conditions was determined as 80 nm and is within the particle size range used in the industrial field (4-100 nm) [4]. It is understood from the analysis based on Intensity in Figure 7b that there are three different particle size groups in the colloidal silica sample. It was evaluated that some of silica particles formed agglomerated and the average particle size increased.

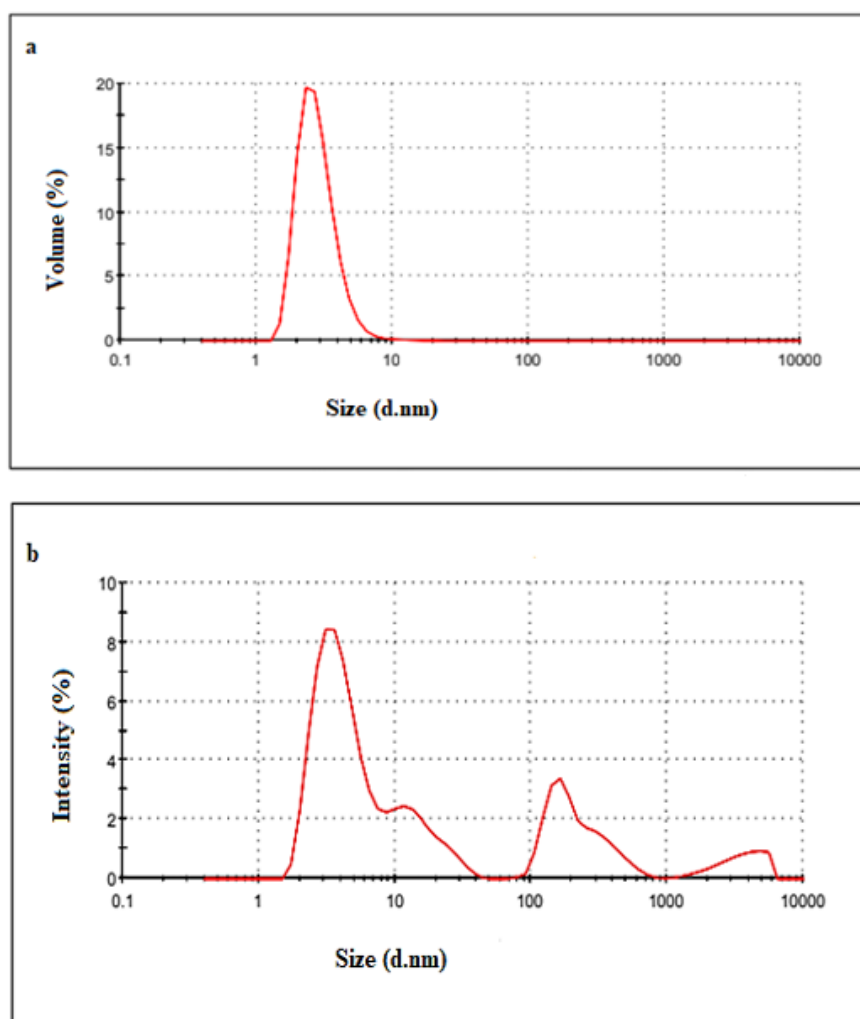


Figure 7. Particle size analysis of colloidal silica produced under optimum conditions.

4. Conclusions

Colloidal silica was produced from sodium silicate solution using ion exchange resin. Appropriate process conditions were determined by analyzing the particle size distribution of the produced colloidal silica. According to the particle size distribution range, the most suitable colloidal silica production parameters are 50°C temperature, 40 minutes time and 300 rpm stirring. The average particle size of colloidal silica produced at the mixing speed of 300 rpm was found to be 80 nm. The chemical bond structure and amorphous structure of colloidal silica were confirmed by FTIR and XRD analyses, respectively.

The study is important as it provides the advantages of producing colloidal silica in the industrially used particle size range from sodium silicate as the starting material, regenerating the resin utilized and reusing it repeatedly.

Peer-review: Externally peer - reviewed.

Author contributions: Concept B. A., J. A., R. T. & M. G.; Data Collection &/or Processing - B. A., J. A., R. T., İ. E. & M. G.; Literature Search - B. A., J. A., R. T. & M. G.; Writing - B. A., J. A., R. T. & M. G.

Conflict of Interest: This paper has been presented at the UKMK-15 (15th National Chemical Engineering Congress) held in Çanakkale (Turkey), September 4-7, 2023.)

Financial Disclosure: This study was supported by Tübitak with a Project No. 1919B012107996 in Tübitak 2209/A category.

References

- [1] Bergna, H. E. (1994). Colloid chemistry of silica: An overview. *The Colloid Chemistry of Silica Chapter 1*. Advances in Chemistry 234(1994), 1-47. DOI: 10.1021/ba-1994-0234.ch001
- [2] Asghar, K., Gholam Reza, V., Mohammad, A., & Mehdi, F. (2008). Preparation and characterization of colloidal silica in alkaline and constant range of pH. *Iranian Journal of Chemistry and Chemical Engineering*, 27(4).
- [3] Blute, I., Pugh, R. J., van de Pas, J., & Callaghan, I. (2007). Silica nanoparticle sols. 1. Surface chemical characterization and evaluation of the foam generation (foamability). *Journal of Colloid and Interface Science*, 313(2). <https://doi.org/10.1016/j.jcis.2007.05.013>
- [4] Hyde, E. D. E. R., Seyfaee, A., Neville, F., & Moreno-Atanasio, R. (2016). Colloidal Silica Particle Synthesis and Future Industrial Manufacturing Pathways: A Review. In *Industrial and Engineering Chemistry Research* (Vol. 55, Issue 33). <https://doi.org/10.1021/acs.iecr.6b01839>
- [5] Falamaki, C. (2002). Mass transfer mechanisms in the fixed-bed ion-exchange process for dilute colloidal silica manufacture. *Chemical Engineering and Technology*, 25(9). [https://doi.org/10.1002/1521-4125\(20020910\)25:9<905:AID-CEAT905>3.0.CO;2-8](https://doi.org/10.1002/1521-4125(20020910)25:9<905:AID-CEAT905>3.0.CO;2-8)
- [6] Kobayashi, M., Juillerat, F., Galletto, P., Bowen, P., & Borkovec, M. (2005). Aggregation and charging of colloidal silica particles: Effect of particle size. *Langmuir*, 21(13). <https://doi.org/10.1021/la046829z>
- [7] Asadi, Z., & Norouzbeigi, R. (2017). Optimization of colloidal nanosilica production from expanded perlite using Taguchi design of experiments. *Ceramics International*, 43(14). <https://doi.org/10.1016/j.ceramint.2017.05.332>
- [8] Kong, H., Huo, J., Liang, C., Li, S., Liu, W., & Song, Z. (2016). Polydisperse spherical colloidal silica particles: Preparation and application. *Chinese Physics B*, 25(11). <https://doi.org/10.1088/1674-1056/25/11/118202>
- [9] Qomariyah, L., Sasmita, F. N., Novaldi, H. R., Widiyastuti, W., & Winardi, S. (2018). Preparation of Stable Colloidal Silica with Controlled Size Nano Spheres from Sodium Silicate Solution. *IOP Conference Series: Materials Science and Engineering*, 395(1). <https://doi.org/10.1088/1757-899X/395/1/012017>
- [10] Cho, G. S., Lee, D. H., Lim, H. M., Lee, S. H., Kim, C., & Kim, D. S. (2014). Characterization of surface charge and zeta potential of colloidal silica prepared by various methods. *Korean Journal of Chemical Engineering*, 31(11). <https://doi.org/10.1007/s11814-014-0112-5>
- [11] Kim, T., Hwang, S., & Hyun, S. (2008). Development of a continuous manufacturing process for silica sols via the ion-exchange of a waterglass. *Industrial and Engineering Chemistry Research*, 47(18). <https://doi.org/10.1021/ie071009d>
- [12] Tsai, M. S., & Wu, W. C. (2004). Aluminum modified colloidal silica via sodium silicate. *Materials Letters*, 58(12–13). <https://doi.org/10.1016/j.matlet.2003.12.006>
- [13] Tsai, M. S. (2004). The study of formation colloidal silica via sodium silicate. *Materials Science and Engineering: B*, 106(1), 52-55.
- [14] Igci, N., & Ozel Demiralp, F. D. (2020). A Fourier Transform Infrared Spectroscopic Investigation of *Macrovipera lebetina lebetina* and *M. l. obtusa* Crude Venoms. *European Journal of Biology*, 79(1). <https://doi.org/10.26650/EurJBiol.2020.0039>

- [15] Chana, C. K., Pengb, S. L., Chua, I. M., & Ni, S. C. (2001). Effects of heat treatment on the properties of poly(methyl methacrylate)/silica hybrid materials prepared by sol-gel process. *Polymer*, 42(9). [https://doi.org/10.1016/S0032-3861\(00\)00817-X](https://doi.org/10.1016/S0032-3861(00)00817-X)
- [16] Musić, S., Filipović-Vinceković, N., & Sekovanić, L. (2011). Precipitation of amorphous SiO₂ particles and their properties. *Brazilian Journal of Chemical Engineering*, 28(1). <https://doi.org/10.1590/S0104-66322011000100011>
- [17] Beganskienė, A., Sirutkaitis, V., Juškėnas, R., Kareiva, A., & Kurtinaitienė, M. (2004). FTIR, TEM and NMR investigations of stöber silica nanoparticles Sol-gel coatings for optical and bioapplications View project FTIR, TEM and NMR Investigations of Stöber Silica Nanoparticles. *MEDŽIAGOTYRA*, 10(4).
- [18] Liu, K., Feng, Q., Yang, Y., Zhang, G., Ou, L., & Lu, Y. (2007). Preparation and Characterization of amorphous silica nanowires from natural chrysotile. *Journal of Non-Crystalline Solids*, 353(16–17). <https://doi.org/10.1016/j.jnoncrysol.2007.01.033>
- [19] Martinez, J. R., Palomares, S., Ortega-Zarzosa, G., Ruiz, F., Chumakov, Y., (2006). Rietveld refinement of amorphous SiO₂ prepared via solgel method. *Materials Letters*, 60 (29-30), 3526-3529
- [20] Yoshida, A., (2006). Silicic acids and colloidal silica. In: Bergna, H. E., Roberts, W. O. (eds) Colloidal silica: fundamentals and applications; surfactant science series, vol. 131. *CRC Press Taylor & Francis Group*, Boca Raton, 37–39.
- [21] Zou, H., & Schlaad, H. (2015). Thermoresponsive PNIPAM/silica nanoparticles by direct photopolymerization in aqueous media. *Journal of Polymer Science, Part A: Polymer Chemistry*, 53(10). <https://doi.org/10.1002/pola.27593>
- [22] Lazaro, A., Van De Griend, M. C., Brouwers, H. J. H., & Geus, J. W. (2013). The influence of process conditions and Ostwald ripening on the specific surface area of olivine nano-silica. *Microporous and Mesoporous Materials*, 181. <https://doi.org/10.1016/j.micromeso.2013.08.006>

City of Bacteria

*¹Nurdan FİLİK , ²Fethi FİLİK 

¹ Suleyman Demirel University, 32260, Isparta, Turkey. ¹ORCID number: <https://orcid.org/0000-0003-4376-7298>

²ORCID number: <https://orcid.org/0000-0003-3564-8782>

* Corresponding author, e-mail: nurdansal@hotmail.com

Submission Date: 04.03.2024

Acceptation Date: 29.03.2024

Abstract: Especially living tissues, implants, catheters, pacemakers, prosthetic heart valves, composite resins, glass ionomer cements, chronic wounds, contact lenses and ceramic materials, etc. It has now been proven that bacteria on all surfaces live a micro-social lifestyle by using Quorum Sensing System (QS), communicating through *N*-Acyl Homoserine Lactone (AHL) signaling molecules, and forming biofilm layer, which is one of most vital virulence factors. In 1978, with discussions of Robert Koch's hypotheses published in 1884, Bill Costerton warned about magnitude of biofilm damage in chronic infections. In 2012, Father of biofilm Bill Costerton broke new ground in his research on biofilm. The concept of "Cell-to-cell communication", which Smith first brought to agenda in 1905, has brought infectious diseases to huge scientific level with QS system and biofilm, which is most important virulence factor of this system. Within the biofilms, bacteria can easily reproduce and communicate with each other, there's actually a fiber optic system that bacteria communicate with each other at speed of light, QS. Biofilm was defined as a 'City of Microbes' by Watnick and Kolter, (2000). Biofilm is mixture of different microorganisms that are held together and protected by glue-like film. It's a slimy matrix and coating that bacteria, fungi, yeast, mold, mycotoxins, viruses and parasites create in order to stay protected and elude immun system. A dysregulated nervous system can lead to taxed immune system. This layer of glue-like slime creates a protective 'sleeping bag' for bacteria, so they can continue to do what they do best, which is thriving in you, while creating chronic diseases. The immune system fully recognizes bacteria, however, can't get to them due to the protective layer as biofilm, thus many times creating an autoimmune situation or cannot effective. In summary, understanding of biofilm is vital to manage and to eradicate biofilm-related diseases. The current review is, therefore, an effort to encompass the current concepts in biofilm, biofilm architectural and its implications in all living creature health and disease.

Keywords: City of bacteria, Bacteria, Biofilm, Quorum Sensing System (QS), Immune system

Bakteriler Şehri

Öz: Özellikle canlı dokular, implantlar, kateterler, kalp pilleri, protez kalp kapakçıkları, kompozit reçineler, cam iyonomer simanlar, kronik yaralar, kontakt lensler ve seramik malzemeler vb. artık tüm yüzeylerdeki bakterilerin mikro-sosyal bir yaşam tarzı yaşadıkları kanıtlanmıştır. Quorum Sensing System (QS), *N*-Açıl Homoserin Lakton (AHL) sinyal molekülleri aracılığıyla iletişim kurarak hayati önemdeki virülens faktörlerinden biri olan biyofilm katmanını oluşturur. Robert Koch'un 1884 yılında yayınlanan varsayımlarının tartışılmasıyla 1978'de Bill Costerton, kronik enfeksiyonlarda biyofilm hasarının büyüklüğü hususunda uyarılarda bulundu. 2012 yılında Biyofilmin babası Costerton'un biyofilm konulu araştırmaları çığır açtı. Smith'in 1905 yılında ilk kez gündeme getirdiği "Bakteri-bakteri iletişimi" kavramı QS sistemiyle, bu sistemin en önemli virülens faktörü olan biyofilm, enfeksiyon hastalıklarını devasa bilimsel bir boyuta geçirmiştir. Biyofilmlerin içinde bakteriler kolaylıkla üreyebiliyor ve birbirleriyle iletişim kurabiliyor, aslında bakterilerin birbirleriyle ışık hızında QS iletişim kurduğu bir fiber optik sistem vardır. Biyofilm, Watnick ve Kolter (2000) tarafından 'Mikroplar Şehri' olarak tanımlanmıştır. Biyofilm, tutkal benzeri bir filmle bir arada tutulan ve korunan farklı mikroorganizmaların bir karışımıdır. Bakterilerin, mantarların, mayaların, küflerin, mikotoksinlerin, virüslerin ve parazitlerin korunmak ve bağışıklık sisteminden kaçmak için oluşturduğu sümüksü bir matris ve kaplamadır. Düzensiz bir sinir sistemi, bağışıklık sisteminin vergilendirilmesine yol açabilir. Bu tutkal benzeri balçık tabakası bakteriler için koruyucu bir 'uyku tulumu' oluşturur, böylece bir yandan kronik hastalıklar yaratırken bir yandan da içinde gelişmek olan en iyi yaptıkları şeyi yapmaya devam edebilirler. Bağışıklık sistemi bakterileri tam olarak tanıyacak ancak biyofilm gibi koruyucu bir tabaka nedeniyle onlara ulaşamaz ve çoğu zaman otoimmün bir durum yaratır veya etkili olamaz. Özetle, biyofilmin anlaşılması, biyofilimle ilişkili hastalıkların yönetilmesi ve ortadan kaldırılması için hayati öneme sahiptir. Bu nedenle mevcut inceleme, biyofilm, biyofilm mimarisi ve bunun tüm canlıların sağlığı ve hastalıkları üzerindeki etkilerini kapsayan güncel kavramları tartışmaktadır.

Anahtar kelimeler: Bakteriler şehri, Bakteri, Biyofilm, Çevreyi Algılama Sistemi (QS), Bağışıklık sistemi

1. Introduction

Biofilm occurs early in fossil record (~3.25 billion years ago) [1]. The first awareness of biofilm existence in natural environments began in the 1970s [2]. Angst, E.C. 1923 reported the slime formation under ships caused by bacteria. In the early 1930s, the term 'film' was referred to as bacterial attachment, aggregation and proliferation on surfaces, and the term 'sessile' bacteria, which adhere to the surface as opposed to free-swimming 'planktonic' bacteria, was firstly used in marine microbiology. [4] studied the growth and adhesion of bacteria on underwater glass surfaces in seawater, and Scientist Characklis studied microbial slime in industrial water systems in the early 1970s [5]. The first biofilm publication reported using term 'biofilm' was by Mack et al. in 1975. In 1977, first microscopic image of biofilm was published and for first time it was shown that dense slime structure surrounded adherent bacteria. Term biofilm was defined in medical field by Costerton in 1985, and concept of biofilm infections and their importance began 40 years ago, with structure of dental pellicles by Jendresen and Høiby's observation of *Pseudomonas aeruginosa* cells in chronically infected cystic fibrosis cases [6].

Biofilm is a cluster of microorganisms to which cells adhere to each other and/or to the surface on which they are located. These interconnected cells are usually embedded in a self-produced Extracellular Polymeric Substance (EPS). Biofilm EPS is a polymeric complex composed of DNA, proteins, and polysaccharides. Biofilms can form on living or non-living surfaces and represent the dominant aspect of microbial life [1].

If biofilm is break down the immune system senses these bacteria, but cannot reach them, then host will occur autoimmune, MCAS, pain, odd neurological issues, buzzing in brain, weird vibrations. In additional, can see reactivation and repeating cycles of chronic diseases. They Exchange DNA that converge together to form new stronger protective organisms. Biofilm is typically clear, White, nude, jellyfish appearance, slippery, slimy, egg white 'feel' and look.

In general, bacterial biofilms show resistance against human immune system, as well as against antibiotics. Health related concerns talk loud due to the biofilm potential to cause diseases, utilizing both device-related and non-device-related infections.

The implications of biofilm architecture, survival and propagative mechanisms of biofilm in the context of both the multidirectional natural environment and infectious diseases are be discussed in this review.

2. Biofilm Structure

Biofilm begins with contact of microorganisms with a surface within their living spaces, and thanks to the various extracellular biopolymers they secrete, they can attach to many different surfaces such as metal, plastic, implants and cell tissue. In many cases, the cost of damage caused by biofilm reaches billions of dollars. Biofilm systems have many negative effects. Antibiotics used to destroy microorganisms do not have sufficient effectiveness on biofilm. In one study, catheter cuffs were coated with silver ions, which are known to have antimicrobial activity, but diffusion of silver ions into environment over time caused coating to lose its antimicrobial activity. The use of antibiotics as coating materials causes microorganisms to become resistant to the antibiotic used and the application loses its effectiveness [7-8].

In medical terms, biofilm formation occurs in 5 steps (Fig. 1). The initial adhesion of the bacteria is be called reversible adhesion and the cells can be easily detached from the surfaces again [9]. The initial weak interactions that develop between bacterial cells and surface are been referred to as reversible adhesion. Various long chain interactions that influence the reversible adhesion process are van der Waals attractive forces, electrostatic forces and hydrophobic interactions. During this stage,

bacteria show Brownian motion and can easily move with fluid force [10]. Electron transfer between the cell surface and the biofilm layer also plays an important role in bacterial adhesion to inorganic and organic surfaces [11].

Initial adhesion between inanimate surfaces and bacteria generally occurs through nonspecific interactions such as hydrophobic. Adhesion to living surfaces generally occurs through specific molecules. During biofilm development, cell-cell adhesion on inanimate surfaces can be achieved by specific adhesion [12]. Once adhesion occurs, the bacteria goes through a number of adaptation stages. Among these, the production of EPS and the development of resistance to antimicrobial agents are the most important [13]. Following reversible binding of bacteria, bacterial cells proliferate and produce EPS [14].

During initial adhesion, there is a bulk flow of organic and inorganic molecules. These molecules are transported across the surface by diffusion or turbulent flow [14]. In turbulent flow, small turbulent turns that may occur suddenly can drag small particles contained in bacterial cells in a direction parallel to the surface, and these small particles can neutralize the Gibbs energy barrier required by the bacteria communicating with a surface, and this Gibbs energy barrier; In fact, van der Waals interactions include all common attractive forces and electrostatic interactions [15]. It has been determined that the adhesion abilities of microorganisms are higher in the logarithmic growth phase, and it has been reported that this is due to the increased hydrophobic properties of the cell wall in the growth phase [16].

Irreversible adhesion of cells is the next important stage in biofilm development. Repulsive forces often prevent bacterial cells from making direct contact with the surface, but this contact occurs through cell surface extensions of bacteria such as flagella, fimbriae, pili and EPS fibrils [17]. For transition from reversible adhesion to irreversible adhesion, various short-chain interactions are required, including dipole-dipole interactions, hydrogen, ionic and covalent bonds, and hydrophobic interactions. Thanks to the interactions between these polymeric fibrils, a bridge is formed between bacterial cells and surface, resulting in irreversible relationship with surface [14]. Irreversibly adherent bacterial cells develop and divide with the use of nutrients offered in mature biofilm layers and are surrounded by fluid. This causes microcolonies structures and the surface covered with cells expands to form an integrated layer. During this process, adherent cells also produce EPS, and EPS stabilizes colony against fixation of surface cells and environmental movements [18]. Here, because the bacteria produce exopolysaccharides, the attached microorganisms have hard time breaking away from the surfaces, and as a result, they cling tightly to the surface when complete biofilm matrix is formed [9].

The third and fourth stages, biofilm maturation, result in formation of complex structure containing water channels. And this complex structure is affected by biological factors such as hydrodynamic properties and cell-cell signals, growth rate of bacteria, EPS production, and bacterial motility [19]. Maturing biofilms can separate from biofilms and disperse in order to survive [20-21]. Bacterial proliferation never stops in the mature biofilm layer. Just as a single cell can be detached, a cluster of cells with a diameter of 500 μM can also be detached from the surface [22].

Fragmentation is a different process and is a periodic dispersal of a sizeable fraction of biomass from biofilm. It may be due to flow dynamics, shear effect of liquid volume, presence of certain chemicals in liquid environment, changes in surface properties of bacteria or layer [21]. The released bacteria can be transported to new regions and the biofilm process begins again [10]. It has been reported that the number of cells detached from biofilm disintegration varies between 10 and 300 cells, depending on the bacterial species [23].

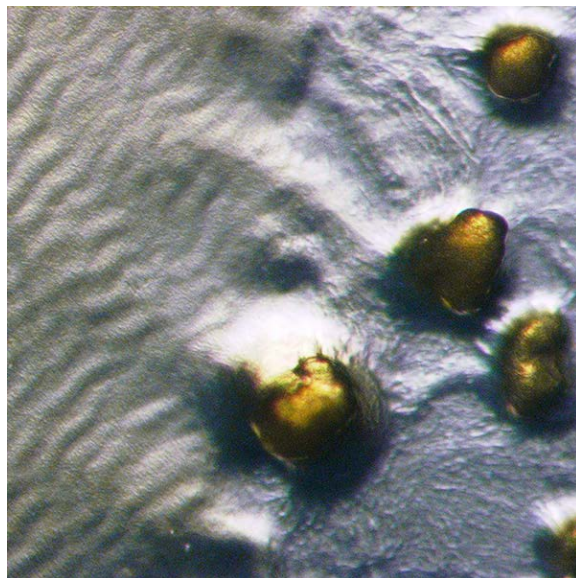


Figure 1. A colony of Biofilm [24].

3. Role of Infections

Pathogens can enter the human body through trauma, medical treatments, dental procedures, or other methods. Biofilms are harmful when they come into touch with exposed wounds. It is estimated that about 65% of all bacterial infections are associated with bacterial biofilms. These include both, device- and non-device-associated infections [25].

Most research on bacterial pathogenesis has focused on acute infections, but these diseases are now being supplemented by new category, chronic infections, caused by bacteria growing within biofilms. Biofilm infections, such as chronic wounds and fibrinous peritonitis infections, affect millions of fish in world every year and cause many deaths. However, in cases where bacteria manage to form biofilm within their host, the infection often proves incurable and can become chronic. The key to chronic biofilm infections is extreme resistance to antibiotics and evasion of host defenses. Bacteria have similar lifestyle (biofilm) in both living environments, but struggle for survival and dominance is different [26].

Bacterial contamination on implants and prosthetic medical instruments causing infections can be life-threatening, chronic infections and mortal [27]. A mature biofilm layer is sticky formation that can be seen even with naked eye. In the presence of biofilm, it is impossible to cure the infection with antibiotic treatment alone [28].

Biofilm infections is their resistance mechanism against antimicrobial agents. EPS, which forms basic structure of biofilm matrix and forms outer layer of biofilm, prevents antimicrobial agents from diffusion. Microbial agents that cannot overcome the EPS barrier cannot reach the microorganism cells within biofilm structure and cannot show their effects. In studies in literature; It has been shown that microorganisms in biofilm form are 1000 times more resistant to antimicrobial agents than free cells. Microorganisms within biofilm structure also cause emergence of multidrug resistance by transferring resistance genes they have developed [29].

Antibiotic resistance is complex in biofilms. Most importantly, biofilm-specific features such as differential expression of multiple gene networks, extracellular matrix, and metabolic heterogeneity of subpopulations within a biofilm colony contribute greatly to antibiotic resistance [30].

Bacteria that form biofilms can transfer plasmids carrying resistance genes to each other by conjugation. As a result, resistance mechanisms develop against various types of antibiotics, and there

is an increase in the incidence of cases in which antibiotics are inadequate even when used multiple times. In its report published in 2013, The United States Centers for Disease Control and Prevention (CDC) states that 23,000 of the more than 2 million bacterial infections occurring in the USA resulted in death due to antibiotic resistance [31].

The European Center or Disease Prevention and Control (ECDC) explains that 25,000 of the bacterial infections occurring in Europe result in death due to antibiotic resistance. Bacteria are among that cause high rates of infection with the biofilm form they form [32-33].

4. Biofilm scenario and biofilm popular spaces

Although researchers such as Henrici and Zobell studied presence of surface-attached bacteria almost 70 years ago, meaning of biofilm communities is only now being understood. Moreover, perspective on microbiology has also changed as bacteria began to be viewed from perspective of multicellular act. Considering that there are countless bacteria that can communicate and countless types of polysaccharides that can be produced, number of different types of biofilms that can be achieved is approaching infinity. For this reason, biofilms formed by single species are very rarely in nature, and biofilms formed by more than one organism are more common [12].

The three major components required for biofilm are microorganisms, solid surface and liquid flow. Oral cavity contains all three components and is susceptible to biofilm formation in short time. It provides conducive environment. Because bacterial community embedded in extracellular polysaccharide matrix that adheres to surfaces such as teeth and surrounding tissues, root canals, implant components, restorative and prosthetic materials is called oral biofilm. Oral biofilm; It is considered clinically important microbiological process because it causes primary and secondary caries, failure of endodontic treatments, periodontal diseases and implant loss due to effect of cariogenic bacteria, depending on surface on which it occurs in mouth.

The National Institutes of Health (NIH) reported that among all microbial infections, 65% and 80%, respectively, are associated with biofilm [25-28].

[34] showed that the adhesion of *Streptococcus spp.* was reversible less than a hundred times in less than 10 minutes. [35] reported that irreversible adhesion of cells to a cleaned surface occurred within 30 min after exposure to a fresh suspension containing *A. flavithermus* B12-Cm cells. [36] found that "*Streptococcus thermophilus* and *Bacillus cereus* cultures reversibly adhered to stainless steel in less than 60 seconds. [12] described that exopolysaccharides and/or specific ligands lock bacteria onto surfaces and form complexes with the surface through the production of pili or fimbriae. After this stage, very strong physical or chemical forces such as scraping, brushing or chemical cleaners are required to remove bacteria from surfaces [10-37].

5. Discussion

Biofilms widely spanning from natural surroundings like rivers and oceans to human-made constructs like pipelines, medical instruments, and even dental plaque in your mouth. They exhibit capacity to flourish in challenging environments, including depths of deep-sea hydrothermal vents and highly acidic hot springs.

Biofilm structures act as shields, permitting the bacteria to cluster together and form a sac-like biofilm. These biofilms serve as defensive effect, making it difficult for the immune system to challenge infections effectively.

Biofilm architecture create challenging situation for immune system by making it harder to combat infections effectively. While immune system recognizes presence of biofilms as foreign entities, it struggles to reach and eliminate them because of their protective structure.

By using in experimental phase drugs and some disruptors, it becomes possible to combat infections that hide within biofilms more effectively. These natural compounds can break down the protective structure of biofilms, rendering them more vulnerable to the immune system.

The difficulty in antibiotic penetration into matrix is quite striking. In *P. aeruginosa* infection, ciprofloxacin reaches the infection site in 40 seconds if there is no biofilm, while it reaches the infection site in 21 minutes if there is biofilm [28].

When oral biofilm is be evaluated, dental plaque is defined as complex communities of microorganisms attached to tooth surface, and with this features it is similar to biofilm structure. For this reason, plaque is be considered as biofilm according to many studies conducted in recent years. When viewed as whole, biofilm contains approximately 700 types of bacteria. New species are still being isolated [38-39].

When food biofilm is be investigated, a single powerful biological agent can weaken biofilms, but is insufficient to destroy mature biofilms formed by bacterial species in foods. The right combination of two or more control approaches, called “barrier technology”, is be thought to overcome this problem [40].

In *P. aeruginosa* infection, mechanical (sonication, etc.) destruction/removal of medical biofilm, immune modulation (low dose azithromycin, doxycycline), local antimicrobials (silver or tobramycin), drugs with good biofilm penetration (e.g. rifampicin (combined), daptomycin, echinocandin use) are eradication methods [28].

Toushik et al. 2020 was reported that "Fighting with old foes: The pledge of microbe-derived biological agents to defeat mono- and mixed-bacterial biofilms concerning food industries" entitled manuscript. Microbe-derived biological agents constitute a “green” biofilm-suppressor approach. Biofilm agents as an alternative to a physical or chemical treatment approach. Biological compounds are effective in preventing both mono-bacterial and mixed-bacterial biofilms. A mixture of biological agents can exhibit broad-spectrum anti-biofilm efficacy.

Foods safety are obligatory for survive. It has been estimated that 250 known and many unknown diseases are transmitted to humans majority by foods unsafety contaminated with pathogenic microorganism, causing diseases of more than 600 million people globally, including 420,000 deaths annually. [41]. The National Institutes of Health in the USA reported that 65% of microbial and 80% of chronic infections, including major foodborne diseases, are primarily caused by microorganisms associated with biofilms [25].

Destroying natural biofilm is much more complex than examining single-species biofilms created experimentally. However, biofilms must investigated in order to successfully apply the knowledge obtained from the experimental environment to the industrial environment. Better model systems and more reliable techniques for evaluating control strategies must be developed. Technological developments in preventing biofilm or eliminating the biofilm that has formed show the importance and currency of the biofilm issue.

6. Conclusion

In 17th century, Antoine Von Leeuwenhoek, for the first time observed a type of creature on his own teeth, discovery considered to biofilm [42]. Zobell in 1943 stated that “the surrounding sea water have less number of bacteria than on the surface” [43]. Even at the end of 1960 and the start of 1970, physical and chemical properties of biofilms were not investigated [44]. [45] observed “Bottle Effect”

of marine microorganisms – the growth and activity enhances when they are attached to a surface [45-25].

Counting live bacteria is important in monitoring biofilm [46]. Adversely, the large doses of antibiotics used to treat biofilms clinically have also contributed to the development of antibiotic-resistant bacteria strains. Also it has been seen that some bacteria within biofilms, called “persister cells” are dormant variants that exhibit antibiotic tolerance and can become active when the therapy is withdrawn [47].

Papadopoulos et al. 2024 was reported that further use X-ray computed microtomography to image spatial distribution of biofilms and computational fluid dynamics to link biofilm. By combining the advantages of additive manufacturing for the creation of reproducible 3D porous microarchitectures with flow control and instrumentation accuracy of microfluidics, system provides a platform to study dynamics of biofilm in 3D porous media and to rapidly test in process engineering [48].

Watnick and Kolter, 2000 ‘Biofilm, city of microbes’ title manuscript this concept, which was termed for the first time, is very impressive, emphatic and shed light on this compilation [49].

Bacteria living in biofilms produce a protective matrix, which makes them difficult to kill. Due to the widespread distribution of biofilms in diseases and their resilience to numerous antimicrobial treatments, biofilm research is receiving more attention. Owing to increasing antimicrobial resistance, the focus of current research is shifting from targeting bacterial growth/division that causes cell death or dormancy, towards novel approaches. Recently, biofilm-related infections have been increasing and have become almost unpreventable. So, new treatment, biofilm drugs and prophylaxis strategies are been needed.

Biofilms are associated with two third of all infections especially chronic and device-related infections. The effects of antibiotic applications on resistance genes should be examined in infection modeling with in vivo model organisms.

QS, major features of biofilm, such as surface adherence, EPS structure, architectural of biofilm, cell features within biofilm and highly regulated biofilm maturation - dispersal are being examined as targets for biofilm-specific treatments.

This very dangerous biofilm formation, which has existed for a long time and whose research continues to this day, has been studied by many scientists. It seems that this vital virulence force, the biofilm, will continue to be a system where bacteria socialize, communicate, easily transfer genes, and in short, will continue to increase their risk of disease.

Peer-review: Externally peer - reviewed.

Author contributions: Concept – N.F.; F.F.; Data Collection &/or Processing – F.F.; Literature Search – N.F.; Writing – N.F.

Conflict of Interest: The authors declare that there is no conflict of interest.

Financial Disclosure: The authors have no financial disclosure to report.

Ethics committee approval: Ethics committee approval is not required for this research.

References

- [1] Hall-Stoodley, L., Costerton, J. W., & Stoodley, P. 2004. Bacterial biofilms: from the natural environment to infectious diseases. *Nature reviews microbiology*, 2(2), 95-108. <http://doi.org/10.1038/nrmicro82>
- [2] Costerton, J.W., Cheng, K., Geesey, G.G., Ladd, T.I., Nickel, J.C., Dasgupta, M. and Marrie, T.J. 1987. Bacterial biofilms in nature and disease. *Annual Reviews in Microbiology*, 41(1); 435-464. <http://doi.org/10.1146/annurev.mi.41.100187.002251>
- [3] Angst, E.C. 1923. The fouling of ship bottoms by bacteria. Report, Bureau Construction and repair. United States Navy Department, Washington, DC.
- [4] Zobell, C.E. and Allen, E.C. 1935. The significance of marine bacteria in the fouling of submerged surfaces. *Journal of Bacteriology*, 29(3); 239. <https://doi.org/10.1128/jb.29.3.239-251.1935>.
- [5] Donlan, R.M. 2002. Biofilms: microbial life on surfaces. *Emerging Infectious Diseases*, 8(9); 881-890. <http://doi.org/10.3201/eid0809.020063>
- [6] Høiby, N. 2014. A personal history of research on microbial biofilms and biofilm infections. *Pathogens and Disease*, 70(3); 205-211. <http://doi.org/10.1111/2049-632X.12165>
- [7] He, W., Liu, H., Wang, Z., Tay, F. R., & Shen, Y. 2024. The Dynamics of Bacterial Proliferation, Viability, and Extracellular Polymeric Substances in Oral Biofilm Development. *Journal of Dentistry*, 104882. <https://doi.org/10.1016/j.jdent.2024.104882>
- [8] Filik, F. 2019. Bazı bakteriyel balık patojenlerinde biyofilm oluşumuna farklı maddelerin in vitro etkisinin tespiti (Master's thesis, Lisansüstü Eğitim Enstitüsü).
- [9] Wang, L., Gu, B., Zhang, L., & Zhu, Z. (Eds.). 2024. Recent Advances in Bacterial Biofilm Studies: Formation, Regulation, and Eradication in Human Infections.
- [10] Marshall, K.C., 1992. Biofilms: an overview of bacterial adhesion activity and control at surfaces. *American Society for Microbiology News*, 58; 202–207.
- [11] Poortinga, A.T., Bos, R. and Busscher, H.J. 2001. Charge transfer during staphylococcal adhesion to tin oxide coatings with different specific resistivity. *Biophysical Chemistry*, 91(3), 273-279.
- [12] Dunne, W.M. 2002. Bacterial adhesion: Seen any good biofilms lately? *Clinical Microbiology Reviews*, 15(2); 155-166. <http://doi.org/10.1128/CMR.15.2.155-166.2002>
- [13] O'Toole, G., Kaplan, H.B. and Kolter, R. 2000. Biofilm formation as microbial development. *Annual Reviews in Microbiology*, 54(1); 49-79.
- [14] Liu, X., Xia, X., Liu, Y., Li, Z., Shi, T., Zhang, H., & Dong, Q. 2024. Recent advances on the formation, detection, resistance mechanism, and control technology of *Listeria monocytogenes* biofilm in food industry. *Food Research International*, 114067. <https://doi.org/10.1016/j.foodres.2024.114067>
- [15] Vadillo-Rodriguez, V., Busscher, H.J., van der Mei, H.C., de Vries, J. and Norde, W. 2005. Role of lactobacillus cell surface hydrophobicity as probed by AFM in adhesion to surfaces at low and high ionic strength. *Colloids and Surfaces B: Biointerfaces*, 41(1); 33-41. <https://doi.org/10.1016/j.colsurfb.2004.10.028>
- [16] Ning, Z.; Xue, B.; Wang, H. 2021. Evaluation of the Adhesive Potential of Bacteria Isolated from Meat-Related Sources. *Applied Sciences* 11(22); 10652. <https://doi.org/10.3390/app112210652>
- [17] Hancock, I.C. 1991. Microbial cell surface architecture. *Microbial Cell Surface Analysis*, 23-59.
- [18] Characklis, W.G. and Marshall, K.C. 1990. *Biofilms*. John Wiley, New York.

[19] Stoodley, P., Sauer, K., Davies, D.G. and Costerton, J.W. 2002. Biofilms as complex differentiated communities. Annual Review of Microbiology, 56;187-209. <https://doi.org/10.1146/annurev.micro.56.012302.160705>

[20] Dayton, H., Kiss, J., Wei, M., Chauhan, S., LaMarre, E., Cornell, W. C., ... & Dietrich, L. E. (2024). Cellular arrangement impacts metabolic activity and antibiotic tolerance in *Pseudomonas aeruginosa* biofilms. Plos Biology, 22(2), e3002205. <https://doi.org/10.1371/journal.pbio.3002205>

[21] Cao, M., Su, J., Zhang, L., Ali, A., Wang, Z., Wang, Y., & Bai, Y. 2024. Loofah sponge crosslinked polyethyleneimine loaded with biochar biofilm reactor for ecological remediation of oligotrophic water: Mechanism, performance, and functional characterization. Bioresource Technology, 130567. <https://doi.org/10.1016/j.biortech.2024.130567>

[22] Telgmann, U., Horn, H. and Morgenroth, E. 2004. Influence of growth history on sloughing and erosion from biofilms. Water Research, 38(17); 3671-3684. <https://doi.org/10.1016/j.watres.2004.05.020>

[23] Wilson, S., Hamilton, M.A., Hamilton, G.C., Schumann, M.R. and Stoodley, P. 2004. Statistical quantification of detachment rates and size distributions of cell clumps from wild-type (PAO1) and cell signaling mutant (JP1) *Pseudomonas aeruginosa* biofilms. Applied and Environmental Microbiology, 70(10); 5847-5852. <https://doi.org/10.1128/AEM.70.10.5847-5852.2004>

[24] Lucinda Hampton, 2019. Physiopedia. Biofilms Role in Chronic Infections. https://commons.wikimedia.org/wiki/File:Myxococcus_xanthus_rippling.png https://www.physio-pedia.com/Biofilms_Role_in_Chronic_Infections#cite_note:-2-1

[25] Jamal, M., Ahmad, W., Andleeb, S., Jalil, F., Imran, M., Nawaz, M.A., Hussain, T., Ali, M., Rafiq, M., Kamil, M.A. 2019. Bacterial biofilm and associated infections. Journal of the Chinese Medical Association. 2018 Jan 1;81(1):7-11. Available from: <https://www.sciencedirect.com/science/article/pii/S1726490117302587> (last accessed 7.10.2019) Last accessed 05.02.2024

[26] Cavallo, I., Sivori, F., Mastrofrancesco, A., Abril, E., Pontone, M., Di Domenico, E. G., & Pimpinelli, F. 2024. Bacterial Biofilm in Chronic Wounds and Possible Therapeutic Approaches. Biology, 13(2), 109. <https://doi.org/10.3390/biology13020109>

[27] Khatoun, Z., McTiernan, C.D., Suuronen, E.J., Mah, T.F., & Alarcon, E.I. 2019. Bacterial biofilm formation on implantable devices and approaches to its treatment and prevention. Heliyon. 2018 Dec 1;4(12):e01067. Available from: <https://www.ncbi.nlm.nih.gov/pmc/articles/PMC6312881/> (last accessed 7.10.19) Last accessed 05.02.2024

[28] Siqueira, F. D. S. 2021. Estudos químicos, moleculares, microbiológicos e toxicológicos de novas moléculas eficazes contra biofilmes de *Pseudomonas aeruginosa* e micobactérias de crescimento rápido (Doctoral dissertation, Universidade Federal de Santa Maria). <http://repositorio.ufsm.br/handle/1/22467>

[29] Hale, S. J., Cameron, A. J., Lux, C. A., Biswas, K., Kim, R., O'Carroll, M., ... & Wagner Mackenzie, B. 2024. Polymyxin B and ethylenediaminetetraacetic acid act synergistically against *Pseudomonas aeruginosa* and *Staphylococcus aureus*. Microbiology Spectrum, e01709-23. <https://doi.org/10.1128/spectrum.01709-23>

[30] Zhou, Z., Tang, J., Tang, K., An, M., Liu, Z., Wu, Z., ... & He, C. 2024. Selective enrichment of bacteria and antibiotic resistance genes in microplastic biofilms and their potential hazards in coral reef ecosystems. Chemosphere, 352, 141309. <https://doi.org/10.1016/j.chemosphere.2024.141309>

[31] Solomon, S. L., & Oliver, K. B. 2014. Antibiotic resistance threats in the United States: stepping back from the brink. Am Fam Physician, 89(12), 938-941.

[32] Hogberg, L. D., Magiorakos, A. P., Heuer, O. E., & Monnet, D. L. 2014. Antimicrobial resistance surveillance in Europe: regional pooling of national data from a small number of sites can be misleading. *Diagn Microbiol Infect Dis*, 80(1), 90. <http://doi.org/10.1016/j.diagmicrobio.2014.03.015>

[33] Weist, K., & Diaz Hogberg, L. (2014). ECDC publishes 2013 surveillance data on antimicrobial resistance and antimicrobial consumption in Europe. *Euro Surveill*, 19(46). doi:10.2807/1560-7917.es2014.19.46.20962

[34] Meinders, J., Van der Mei, H. and Busscher, H. 1995. Deposition efficiency and reversibility of bacterial adhesion under flow. *Journal of Colloid and Interface Science*, 176(2); 329-341.

[35] Parkar, S., Flint, S. and Brooks, J.D. 2004. Evaluation of the effect of cleaning regimes on biofilms of thermophilic bacilli on stainless steel. *Journal of Applied Microbiology*, 96(1); 110-116.

[36] Flint, S.H., Brooks, J. & Bremer, P. 1997. The influence of cell surface properties of thermophilic streptococci on attachment to stainless steel. *Journal of Applied Microbiology*, 83(4); 508-517. <http://doi.org/10.1046/j.1365-2672.1997.00264.x>

[37] Palmer, J., Flint, S., & Brooks, J. 2007. Bacterial cell attachment, the beginning of a biofilm. *Journal of Industrial Microbiology and Biotechnology*, 34(9); 577-588.

[38] Ten Cate JM. 2006. Biofilms, a new approach to the microbiology of dental plaque. *Odontology*, 2006,94(1):1-9

[39] Mizuta, M., & Suzuki, I. 2024. *Streptococcus mutans* Membrane Vesicles, Containing Insoluble Glucan Synthase and Extracellular DNA, Contribute to the Promotion of Initial Attachment and Colonization of *Actinomyces oris*. *International Journal of Oral-Medical Sciences*, 22(2), 57-68. <https://doi.org/10.5466/ijoms.22.57>

[40] Tousehik, S.H., Rahaman Mizan, M.F., Hossain, M.I., Ha, S.D. 2020. Fighting with old foes: The pledge of microbe-derived biological agents to defeat mono and mixed-bacterial biofilms concerning food industries. *Trends in Food Science & Technology*, 99, 413-425. <https://doi.org/10.1016/j.tifs.2020.03.019>

[41] World Health Organization, WHO, 2019. Food safety <https://www.who.int/news-room/fact-sheets/detail/food-safety/> (2019), Accessed 7th Oct 2019

[42] Percival, S. L., Malic, S., Cruz, H., & Williams, D. W. 2011. Introduction to biofilms. *Biofilms and veterinary medicine*, 41-68.

[43] Zobell, C. E. 1943. The effect of solid surfaces upon bacterial activity. *Journal of bacteriology*, 46(1), 39-56.

[44] Wyatt, J. E., Hesketh, L. M., & Handley, P. S. 1987. Lack of correlation between fibrils, hydrophobicity and adhesion for strains of *Streptococcus sanguis* biotypes I and II. *Microbios*, 50(202), 7-15.

[45] Heukelekian, H., & Heller, A. 1940. Relation between food concentration and surface for bacterial growth. *Journal of bacteriology*, 40(4), 547-558.


[46] Prigent-Combaret, C., Brombacher, E., Vidal, O., Ambert, A., Lejeune, P., Landini, P., & Dorel, C. 2001. Complex regulatory network controls initial adhesion and biofilm formation in *Escherichia coli* via regulation of the *csgD* gene. *Journal of bacteriology*, 183(24), 7213-7223. <https://doi.org/10.1128/jb.183.24.7213-7223.2001>

[47] Upadhyay, A., Pal, D., & Kumar, A. 2024. Interrogating *Salmonella Typhi* biofilm formation and dynamics to understand antimicrobial resistance. *Life Sciences*, 339, 122418. <https://doi.org/10.1016/j.lfs.2024.122418>

[48] Papadopoulos, C., Larue, A. E., Toulouze, C., Mokhtari, O., Lefort, J., Libert, E., ... & Davit, Y. 2024. A versatile micromodel technology to explore biofilm development in porous media flows. *Lab on a Chip*, 24(2), 254-271.

[49] Watnick, P., & Kolter, R. 2000. Biofilm, city of microbes. *Journal of bacteriology*, 182(10), 2675-2679. <https://doi.org/10.1128/jb.182.10.2675-2679.2000>

Structural, Morphological and Magnetic Investigation of Half-Doped La_{0.5}Ba_{0.5}MnO₃ Perovskite Nanoparticles

¹Yusuf Samancıoğlu 

¹Muğla Sıtkı Koçman University, Vocational School of Health Services, Department of Medical Services and Techniques, Opticianry, Marmaris, Muğla, Turkey.

Corresponding author, e-mail: ysamancioglu@mu.edu.tr , <https://orcid.org/0000-0002-3540-5011>

Submission Date: 09.02.2024

Acceptation Date: 17.05.2024

Abstract: This study investigated the effect of barium (Ba) substitution for lanthanum (La) on the magnetic properties of the half-doped perovskite manganite compound La_{0.5}Ba_{0.5}MnO₃ (LBMO). The LBMO sample was prepared via the sol-gel method and sintered in air at 1000°C for 24 hours. Scanning electron microscopy (SEM)-energy dispersive X-ray spectroscopy (EDS) analysis revealed random formation of BaMnO₃ nanorods on the LBMO surface. The LBMO perovskite exhibited a particle size distribution of approximately 60 nm, while the BaMnO₃ nanorods possessed widths ranging from 100-250 nm and lengths between 5-20 µm. X-ray diffraction (XRD) analysis found that the main perovskite compound (LBMO) exhibits a cubic crystal structure ($a = 3.9108 \text{ \AA}$), while the nanorods (BaMnO₃) possess a hexagonal crystal structure ($a = 5.6454 \text{ \AA}$, $c = 4.8224 \text{ \AA}$). The Curie temperature (T_C) was determined to be approximately 323 K, close to room temperature, zero field cooling (ZFC) and field cooling (FC) curves to elucidate the magnetic properties. Furthermore, magnetization measurements yielded a magnetic entropy change (ΔS_M) of 0.62 J/kgK at 1 T and 2.25 J/kgK at 6 T.

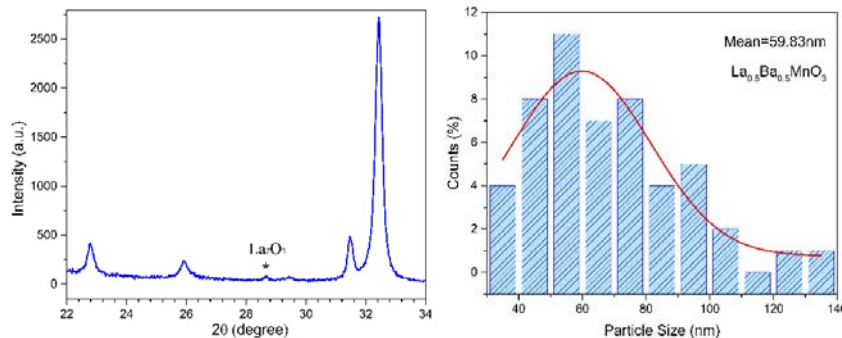
Keywords: Half-doped perovskite manganites, BaMnO₃, nanorods, Curie temperature

Yarı-Katkılı La_{0.5}Ba_{0.5}MnO₃ Perovskit Nanoparçacıklarının Yapısal, Morfolojik ve Manyetik Özelliklerinin İncelenmesi

Öz: Bu çalışma La_{0.5}Ba_{0.5}MnO₃ (LBMO) yarı katkılı perovskit manganit bileşiminde lantan (La) yerine baryum (Ba) yer değişiminin manyetik özellikleri üzerindeki etkisi araştırıldı. Numune sol-jel yöntemi kullanılarak hazırlandı ve 1000°C'de 24 saat ısı işleme tabi tutuldu. Taramalı elektron mikroskobu (SEM)-enerji dağılım spektroskopisi (EDS) analizi LBMO yüzeyinde rastgele BaMnO₃ nano çubuk oluşumunu ortaya çıkardı. LBMO perovskit bileşiminin parçacık boyutu dağılımının yaklaşık 60 nm olduğu bulundu. Ayrıca, analizler sonucunda BaMnO₃ nano çubukların genişliği 100-250 nm ve uzunluğu 5-20 µm aralığında değiştiği gözlemlendi. X-ışını kırınımı (XRD) analizi, ana perovskit bileşiminin (LBMO) kübik kristal yapıda ($a = 3.9108 \text{ \AA}$) olup, nano çubukların ise altıgen ($a = 5.6454 \text{ \AA}$, $c = 4.8224 \text{ \AA}$) kristal yapıya sahip olduğu gösterildi. Manyetik özelliklerin ortaya konabilmesi için sıfır alan soğutma (ZFC) ve alan altında soğutma (FC) eğrilerinden yararlanarak Curie sıcaklığını oda sıcaklığına yakın (T_C) 323 K olduğu tespit edildi. Manyetizasyon ölçümleri verileri kullanılarak hesaplanan manyetik entropi değişiminin ($-\Delta S_M$), 1 T'de 0,62 J/kgK ve 6 T'de 2,25 J/kgK olduğu bulundu.

Anahtar kelimeler: Yarı katkılı perovskit manganitler, BaMnO₃, nanoçubuklar, Curie sıcaklığı.

Graphical Abstract:



¹ Corresponding author: Tel: 0 252 211 56 22

E-mail: ysamancioglu@mu.edu.tr

1. Introduction

Perovskite oxides are a class of materials with the general formula ABO_3 , where A^{3+} and B^{2+} are metal cations and O^{2-} is oxygen. These materials have attracted significant attention in recent years due to their diverse and intriguing electronic, magnetic, and structural properties. One of the most promising members of this family is $La_{1-x}A_xMnO_3$ ($A=Ca^{2+}, Sr^{2+}, Ba^{2+}, \dots$ etc.), a half-doped perovskite manganite $La_{0.5}Ba_{0.5}MnO_3$ (LBMO) with a Curie temperature close to room temperature [1]–[3]. Previous studies have selected half-doped perovskites of this type for the creation of dielectric ferromagnets with high-frequency properties and self-magnetization. Additionally, they are being investigated due to their high magnetoresistance and manyetocaloric properties. The nature of perovskite manganites is not fully understood [4]. This makes LBMO a promising candidate for a wide range of applications, including spintronic devices, magnetic sensors, catalytic materials, and other electronic devices [5-8]. Differences in the cations of the perovskite compound as a result of Ba substitution for La have also been reported in literature studies. One of the key factors that influences the properties of $La_{0.5}^{3+}Ba_{0.5}^{2+}Mn_{0.5}^{3+}Mn_{0.5}^{4+}O_3^{2-}$ is the ratio of La^{3+} to Ba^{2+} cations. For this compound, the ionic radius incompatibility and the presence of complex valences cause the manganite structure to exhibit a complex phase diagram and contain multiple phases together [9]. Ba^{2+} substitution for La^{3+} leads to a number of changes in the manganese atoms (Mn^{3+}, Mn^{4+}), including increased carrier concentration, reduced lattice distortion, and enhanced ferromagnetism. And then T_c of these perovskite compounds exhibits a strong dependence on the Mn^{3+}/Mn^{4+} ratio [10]. In addition, the atomic radius of the Ba^{2+} atom is quite larger than La^{3+} , so Ba^{2+} substitution can also cause the formation of $Ba^{2+}Mn^{4+}O_3^{2-}$ through a process known as self-assemble. Literature reports suggest that upon approaching designated doping rates, the manganese ions in the 50% Ba-substituted perovskite compound exhibit changes in their valence state. This phenomenon is further reinforced by the application of high-temperature heat treatment under atmospheric conditions, leading to valence fluctuations in manganese ions ($Mn^{2+}, Mn^{3+}, Mn^{4+}, \dots$ etc.) exceeding a 47% doping contribution rate[9]–[12]. In the case of LBMO, the second phase is $BaMnO_3$ (BMO), which forms during the sol-gel synthesis process [13]. The sol-gel method is widely used for producing bulk perovskite manganite compounds due to its cost-effectiveness, ease of synthesis, and ability to produce homogeneous samples, as well as for allowing adjustments in transition temperatures through various element doping rates. The hydrothermal synthesis method is frequently used in the literature for the production of LBMO and BMO perovskite nanorods or nanocrystals [14]. However, it is reported that this synthesis method suffers from limitations, particularly in controlling particle size and shape, as well as achieving a homogeneous distribution due to the emergence of undesirable impurities during production [15]–[18]. In this study, the structural, morphological and magnetic properties of the LBMO compound produced by the sol-gel method were comprehensively examined. The formation of nanorods on LBMO can have a significant impact on the magnetic properties of the material. It is known that materials reduced to nano size have different chemical and physical properties than their bulk counterparts [17]. Today, it is reported in the literature that perovskite manganites, which are very difficult to produce at nanoscale, exhibit different magnetic and electrical properties and that obtaining magnetic nanosensors has become difficult due to the inability to provide a stable electronic balance in these compounds [19]. $BaMnO_3$ nanorods on the compound surface exhibit antiferromagnetic properties by creating new magnetic interactions [20]. In addition, the nanorods can also be used to tailor the magnetic properties of LBMO for specific applications. Although it has been understood late that the antiferromagnetic properties occurring in perovskite manganite materials can be used, compounds such as perovskite ($BaMnO_3-LaMnO_3-LaFeO_3$) can be used in spintronic devices, solid oxide fuel cells (SOFC), energy storage, electrodes, dielectric materials and drug delivery [13], [17], [21]. We believe that our study will provide new insights into the relationship between Ba substitution and the formation of $BaMnO_3$ nanorods in LBMO. Our

findings will also be valuable for the development of LBMO-based materials with tailored magnetic properties for particular applications.

2. Materials and Methods

The LBMO sample was synthesized using the sol-gel method and utilization of consumables of high purity was employed, including 99.9% La_2O_3 (Sigma-Aldrich), 98.5% $\text{Mn}(\text{NO}_3)_2 \cdot 4\text{H}_2\text{O}$ (Merck), 99% $\text{Ba}(\text{NO}_3)_2$ (Merck). To initiate the synthesis, the consumables were dissolved in a solution containing HCl and NH_3 . The resulting solution was mixed using a magnetic heater stirrer at a temperature of 150°C . Subsequently, ethylene glycol and citric acid were added to the mixture, and the temperature was raised to 300°C , resulting in gelation. After the gelation process was completed, the organic compounds were eliminated by subjecting the gel to burn at 600°C for 12 hours. The resulting powder compound was then ground in an agar mortar for 6 hours to ensure homogeneity and optimized distribution. To prepare the sample for analysis, approximately 1 gram of the powder was accurately weighed and pressed into a mold with a diameter of 13 mm and a thickness of 2 mm, applying a pressure of 3 bar. The bulk sample was subsequently heat treatment (controlled with a temperature increase of 5.5°C per minute) in a 1000°C furnace for 24 hours to enhance its crystallinity and stability. The crystal structure of the synthesized samples was formed during heat treatment [28]. To investigate the crystallographic characteristics of the samples, X-ray diffraction (XRD) measurements were conducted using the Rigaku SmartLab X-ray diffractometer. The samples were placed in the diffractometer and scanned at room temperature, covering an angular range between 20 to 100 degrees with a precise step size of 0.01 degrees. Surface analysis of samples subjected to 24 hours heat treatment at 1000°C which was using Jeol 7600F Scanning Electron Microscope (SEM). This advanced SEM allows for high-resolution imaging of sample surfaces at different magnifications and also offers chemical composition analysis through Energy Dispersive X-ray Spectroscopy (EDS). This SEM analysis was performed using electrons focused under an acceleration voltage of about 20 keV. The Physical Property Measurement System (PPMS) Quantum Design DynaCool-9 served as a pivotal tool in conducting an exhaustive exploration into the distinctive magnetic properties inherent to the samples under scrutiny. These analyses were executed using the PPMS in conjunction with a closed-cycle helium cryostat, ensuring an environment of controlled thermal stability. This advanced apparatus operates within a controlled temperature range spanning from 1.8 K to 400 K, thus facilitating meticulous analyses across a substantial thermal spectrum. Furthermore, this configuration affords the precise application of magnetic fields, spanning from 0 T to 6 T, thereby creating an ideal environment for a comprehensive investigation into the magnetic behaviors of materials under investigation.

3. Results and Discussions

3.1. XRD Analysis

X-ray diffraction (XRD) analysis was employed to determine the crystal structure of the synthesized material. Rietveld refinement, a comprehensive technique for analyzing XRD data, was utilized. As shown in Figure 1, the FullProf program was used for Rietveld analysis, and the obtained XRD data were compared with simulated diffraction patterns based on established crystallographic information [22]. This analysis provided valuable insights into the crystallographic properties, lattice parameters, and symmetry of the samples. In the Rietveld analyses conducted in previous studies, a very common occurrence observed during $x = 0.5$ doping of the Ba element is the formation of the BMO phase along with the LBMO main phase. The addition of Ba to the structure alters the electrical charge balance, resulting in changes in the Mn–O–Mn bond angle and length due to radius

incompatibility, leading to the emergence of BMO impurities in the perovskite structure. The XRD results presented in Table 1 revealed that the main phase, the LBMO perovskite compound, exhibited a cubic crystal structure ($Pm\bar{3}m$ space group) [9], [17], [21]. Conversely, the $BaMnO_3$ nanorods, identified as the second phase, adopted a hexagonal crystal structure and space group $P6_3/mmc$ [4], [18], [23]. The small peak marked with * in the XRD pattern between 28.65° and 29.43° was attributed to La_2O_3 [24]–[27]. In the XRD analysis, trace amounts of La elements, which could not incorporate into the main structure, were detected as impurities in the form of the La_2O_3 compound.

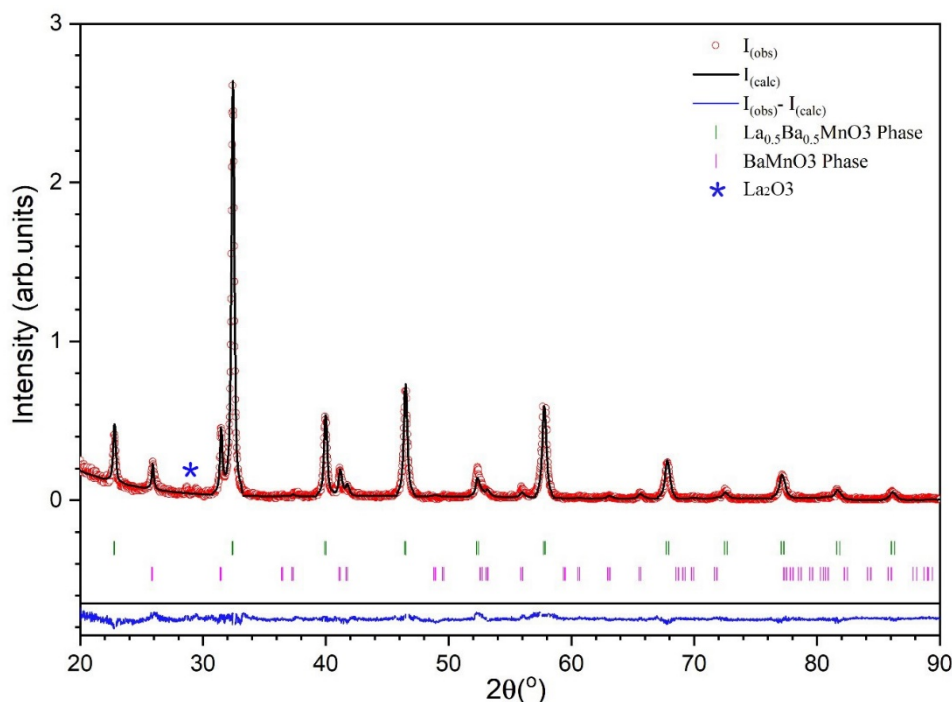


Figure 1. Observed and calculated XRD data and Rietveld refinement for $La_{0.5}Ba_{0.5}MnO_3$ – $BaMnO_3$

Table 1. X-ray analysis of sample $La_{0.5}Ba_{0.5}MnO_3$ – $BaMnO_3$ unit cell parameters for Rietveld refinements

	$La_{0.5}Ba_{0.5}MnO_3$	$BaMnO_3$
Crystal Structure	Cubic	Hexagonal
Space Group	$Pm\bar{3}m$	$P6_3/mmc$
$a(\text{Å})$	3.9108	5.6954
$b(\text{Å})$	3.9108	5.6954
$c(\text{Å})$	3.9108	4.8224
$V(\text{Å})^3$	59.8115	135.4692
$Mn-O-Mn$ (°)	180	-
$Mn-O1$ (Å)	1.95538	-
GoF	1.3	1.3
Phase Fract (%)	80.25	19.75
Rp	13.9	13.9
Rwp	17.9	17.9
Re	12.1	12.1
X^2	2.4	2.4

3.1.2. SEM-EDS Analysis

Figure 2 presents SEM images of the LBMO sample surface at various magnifications. In the



SEM image (Figure 2a) taken at 15 kX magnification, two different structures stand out. The main phase exhibits a granular structure, while the second phase was formed in the form of rod-like structures. These randomly distributed rod-like structures were investigated in detail by SEM. On the other hand, in figure 2 g and h, in order to better understand and investigate rod-like structures, a single nanorod was isolated onto the adhesive carbon conductive tape surface for structural analysis using SEM techniques. The graph in Figure 2 a shows the result obtained in the ImageJ program used to calculate the particle distribution analysis revealed that the average particle size for the main phase was 59.83 nm (~60 nm). To gain a better understanding of the nanorods formed on the surface and to determine their formation within the main structure, SEM images were captured at various magnifications from different regions of the sample surface (Figure 2-b,c,d,e,f). In the SEM image taken at 30 kX magnification in Figure 2e, it is observed that the main structure is distributed homogeneously and the particle size is almost equal everywhere, while the other phase (BMO) grows randomly and moving away the structure. It is also observed that these structures are not uniform and their thickness and length vary from place to place. Figure 2f depicts an SEM image with magnification values of up to 140 kX, revealing a homogeneous distribution of particles in the main structure. Additionally, another phase (BMO) with regular cross-sections and a smooth surface is observed. These SEM images (Figure 2: a-f , respectively) revealed a distinct structure formed outside the main LBMO. The smooth morphology of the rod-like structures and the underlying granular LBMO matrix suggest a random distribution throughout the sample surface. The SEM images in Figure 2g and h illustrate the presence of a nanorod structure with smooth cross-sections, distinct from the main structure. In Figure 2h, the underlying surface is the adhesive carbon conductive tape.

In Figure 3, an attempt was made to select the largest area by going to the 5 kX value of the sample at low magnification. For EDS analysis, area and point scans were made for approximately 12 different regions. The EDS detector collected characteristic X-rays and provides elemental composition (by weight percentage) data in the table in Figure 3. The random distribution of the rods on the surface in the region taken for SEM–EDS analysis is noteworthy. Overall, the average composition value of the compound $\text{La}_{0.5}\text{Ba}_{0.5}\text{MnO}_3$ confirms that the desired stoichiometry has been achieved. In particular, the purple colored areas in the table (spectrums 7 and 10) correspond to regions on rod-like structures and exhibit lower La content and higher Ba content compared to the average composition. The XRD analysis suggests that the absence of trace amounts of La element in these two regions is attributed to the formation of the La_2O_3 phase and its subsequent removal from the structure. Consequently, the x-ray reflections collected from the nanorods on the surface are more pronounced, leading to the detection of an excess of Ba content with EDS detector.

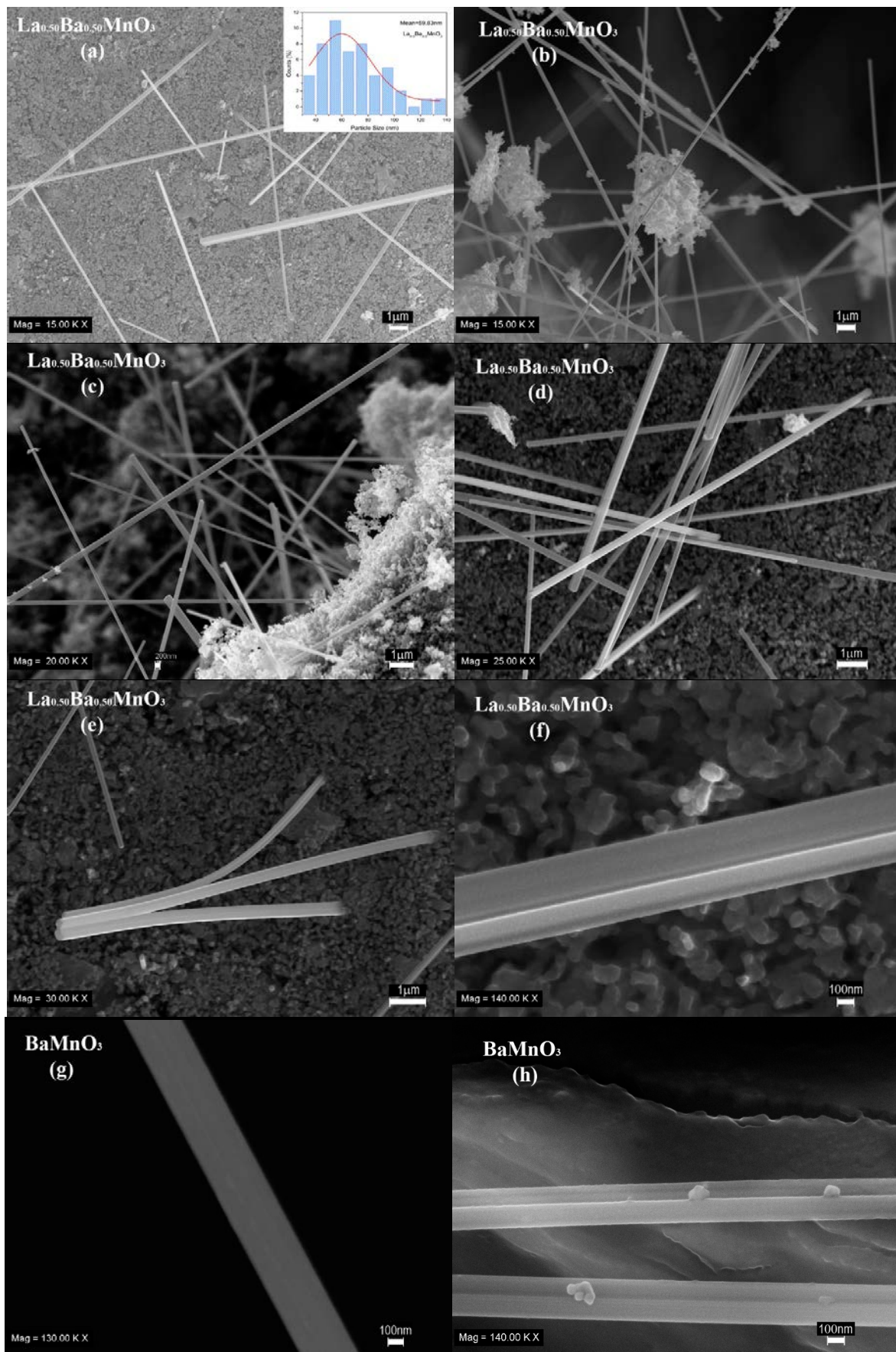


Figure 2. Magnifications of SEM images, a,b) 15kX c) 20kX d) 25kX e) 30kX c) 140kX $\text{La}_{0.5}\text{Ba}_{0.5}\text{MnO}_3$ and g) 130kX, h) 140kX is BaMnO_3 nanorod.

To accurately determine the composition of these nano-sized structures, EDS analysis was conducted on a single nanorod extracted from the surface (Figure 2g). As shown in Figure 3, EDS analysis of the isolated nanorod was taken from four different regions, confirming that this nanostructure is BaMnO₃ as a result of the EDS. This finding supports the two-phase structure observed in the XRD analysis and correlates the presence of rod-like structures observed in the SEM images with the BaMnO₃ phase. Therefore, BaMnO₃ nanorods can be defined as impurities formed independently on the surface of the LBMO perovskite manganite. Particle size analysis revealed that these nanorods had a thickness range of 100 to 250 nm and a length of 5 to 20 μm. This comprehensive analysis of SEM and EDS results revealed the homogeneity of the sample, both in terms of phase distribution and adherence to the desired stoichiometric ratio.

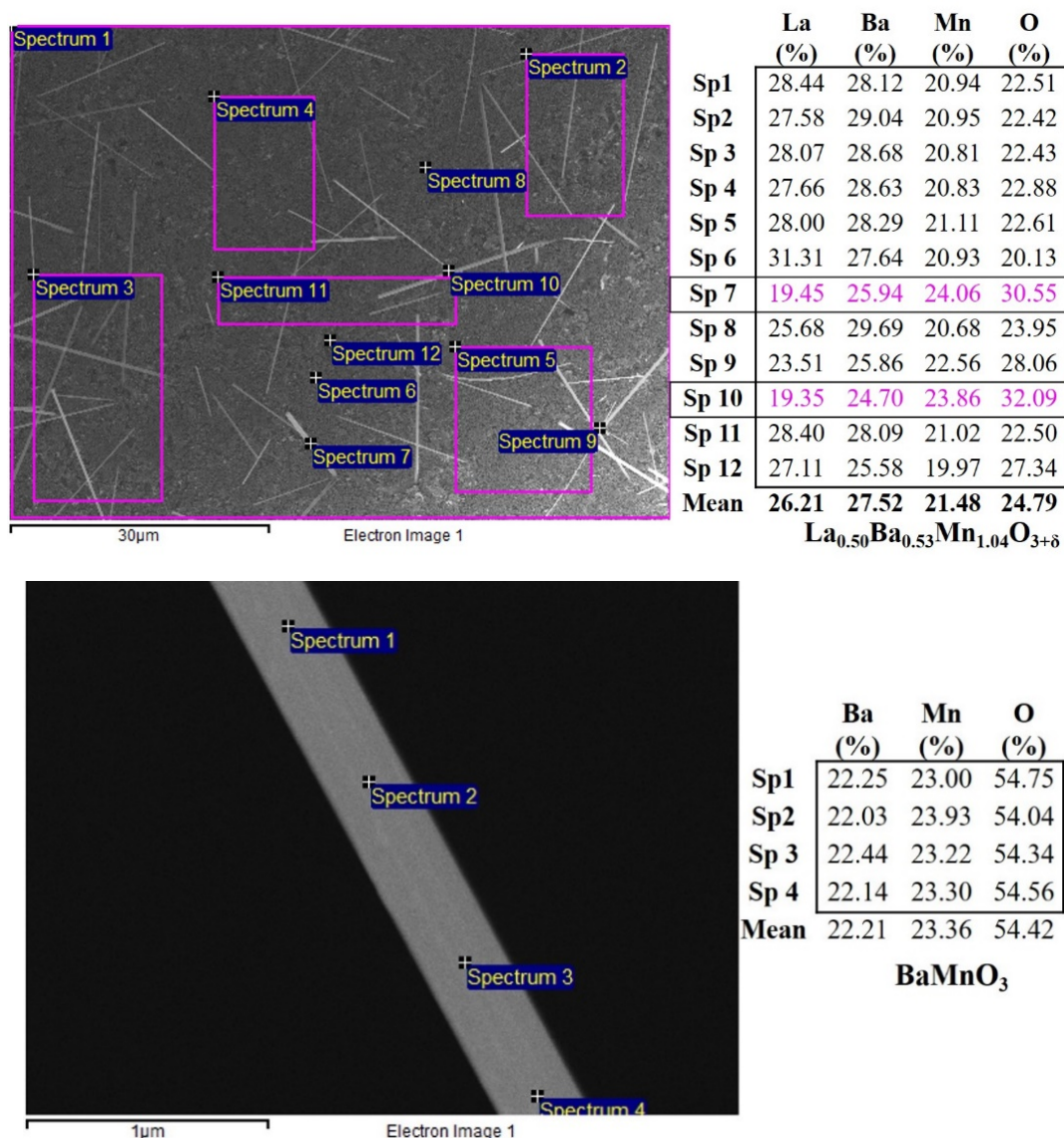


Figure 3. EDS analysis % Weight for La_{0.5}Ba_{0.5}MnO₃ perovskite nanoparticles and BaMnO₃ nanorod.

3.1.3. Magnetic Properties

The investigation encompassed magnetization measurements as functions of both temperature and magnetic field, denoted as M(T) and M(H) respectively. These analyses were executed using the Quantum Design Physical Properties Measurement System (PPMS) in conjunction with a closed-

cycle helium cryostat, ensuring an environment of controlled thermal stability. Figure 4a showcases $M(T)$ measurements conducted under various conditions, including zero field cooling (ZFC) and field cooling (FC) at a magnetic field strength of 50 Oe (5 mT). This extensive procedure covered a temperature range from 5 K to 400 K. Based on both XRD and SEM–EDS data, it is evident that two distinct phases are formed in the structure upon Ba doping. This observation has also influenced magnetic measurements. Spin-glass interactions may arise due to the presence of antiferromagnetic regions (BMO) within a compound (LBMO) predominantly exhibiting ferromagnetic properties. Furthermore, the significant gap between the ZFC and FC curves at lower temperatures supports this interaction. By analyzing the FC curve in Figure 4a, the T_C value was determined to be 323K, corresponding to the peak of the dM/dT curve [19], [20], [29].

To evaluate the effect of the paramagnetic phase using the Curie–Weiss law in equation (1), we examined the slope of the reverse susceptibility ($1/\chi$) as a function of temperature using the FC curve (Fig. 4b). The red line in the graph represents the Curie-Weiss fit, while the θ_{CW} value represents the paramagnetic Curie-Weiss temperature value (where C in the equation is the Curie constant). If θ_{CW} is greater than T_C , it indicates the presence of magnetic inhomogeneity [12], [30]. Furthermore, $M(H)$ measurements Figure 4c were executed meticulously for the sample. This process involved intervals of 4 K, encompassing temperatures both above and below the T_C value. The magnetic field strength extended up to 6 T, thereby encapsulating a substantial range of magnetic conditions. The intricate assessment of the magnetic entropy change ($-\Delta S_M$) values necessitated the utilization of data derived from the $M(H)$ measurements (Figure 4c). Central to this analysis was Maxwell's thermodynamic equation (2) and if the system is in thermodynamic equilibrium, this formula turns into an integral (3), (4) this equation played a pivotal role in the precise calculation of the magnetic entropy change values. For simplicity, the integral expression (2) was approximated using a summation, wherein the derivative within the integral was discretized using finite differences [31], [32]. These calculations were based on discrete magnetization values acquired at distinct temperatures and applied magnetic fields, as outlined in the following expression (5) Here, ($-\Delta S_M$) represents the magnetic entropy change at temperature T_i . The values of M_i and M_{i+1} correspond to the experimental magnetization at temperatures T_i and T_{i+1} , respectively, under the influence of the magnetic field H_i , employing this comprehensive methodology, the precise quantification of $-\Delta S_M$ values was achieved (Figure 4d). $-\Delta S_M$ was observed to be 0.62 J/kgK at a magnetic field of 1 T and 2.25 J/kgK at a magnetic field of 6 T, as determined from the $M(H)$ curves. The wide maximum value distribution of $-\Delta S_M$ around the T_C in LBMO is a desirable property for electronic applications. Future studies will investigate whether the T_C is increased or decreased by the formation of $BaMnO_3$ nanorods. This approach provided invaluable insights into the magnetic characteristics of the examined materials, thus enriching our understanding of their potential applications within novel magnetic cooling prototype.

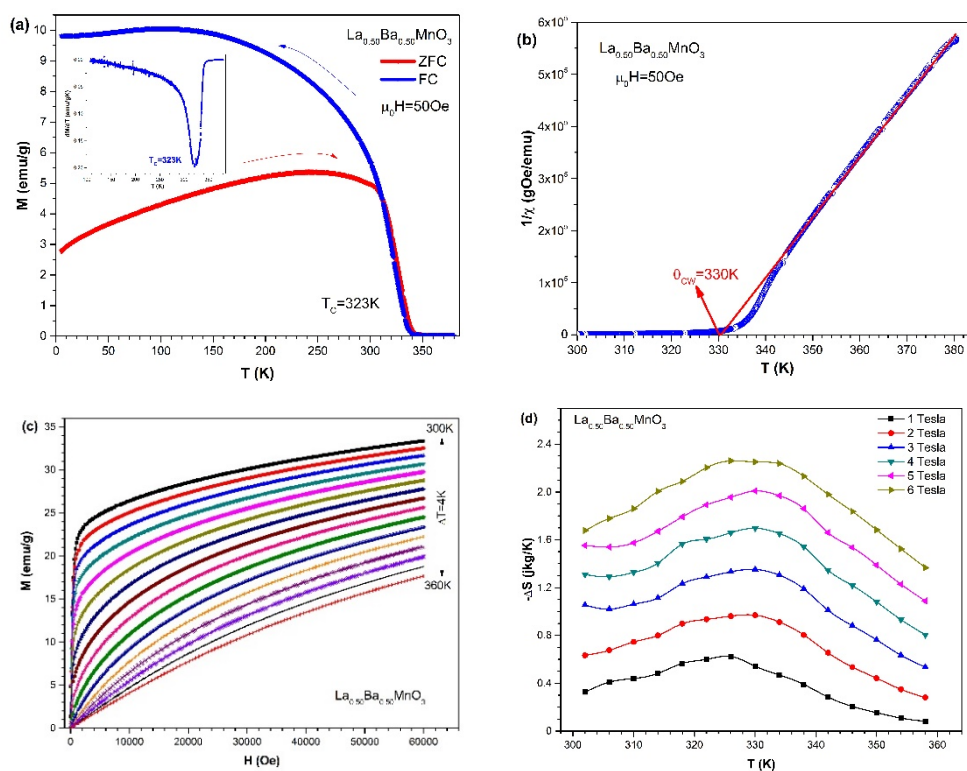


Figure 4. a) $M(T)$ curves of the compounds obtained using ZFC and FC, insets: dM/dT (T) curve b) $1/\chi$ (T) curve and c) $M(H)$ curves of the compounds at 1T to 6 T for both below and above T_C , d) Temperature dependences of $-\Delta S_M$ at several magnetic field changes for $\text{La}_{0.5}\text{Ba}_{0.5}\text{MnO}_3$.

4. Conclusions

In this study, half-doped $\text{La}_{0.5}\text{Ba}_{0.5}\text{MnO}_3$ perovskite manganite compound was successfully obtained using the sol-gel method. It was confirmed by SEM-EDS analysis that the main compound showed a homogeneous particle distribution and the presence of BMO nanorods, regardless of the main structure. XRD refinement revealed that the crystal structure of the synthesized material comprised two distinct phases: the main phase consisting of 80.25% LBMO and a secondary phase comprising 19.75% BMO nanorods. Additionally, it was determined that the trace amount of La element not incorporated into the main structure existed in the form of La_2O_3 . Detailed SEM analysis revealed that the secondary phase was present in the form of nanorods randomly distributed on the surface, with varying lengths and widths. Furthermore, EDS analysis confirmed the composition of these nanorods, with the composition identified XRD analysis as BaMnO_3 . It is worth noting that each nanorod exhibits a uniform width along its entire length, a characteristic commonly observed in the hydrothermal production method, not seen in the sol-gel method [33]. Magnetization measurements revealed that the Curie transition temperature of the LBMO sample was determined to be 323 K. Literature reports have shown Curie transition temperature values for LBMO samples ranging from 270 K to 335 K [7]–[9], [33], [35]–[37]. The aim is to produce a material exhibiting a magnetic phase transition close to room temperature. Discrepancies in Curie temperatures among LBMO samples in the literature stem from variations in production methods, sintering temperature and sintering time. Moreover, it was observed that the formation of BMO nanorods on the surface of the LBMO sample obtained in this study resulted in the removal of a certain amount of Mn atoms. It is hypothesized that alterations in the bond angle and lengths (Mn–O–Mn) of Mn atoms departing from this structure, along with the reduction in Mn atoms, which serve as magnetic moment carriers,

contribute to raising the ferromagnetic to paramagnetic phase transition in LBMO above to room temperature [34]. The isothermal magnetic entropy change of the LBMO sample was calculated using magnetization measurements. The sample exhibited a magnetic entropy change ($-\Delta S_M$) of 0.62 J/kgK and 2.25 J/kgK at applied fields of 1 T and 6 T, respectively. Examination of the $-\Delta S_M$ graph reveals a very wide distribution around T_c . This broad distribution is a desirable characteristic for magnetic cooling applications in perovskite materials. While the LBMO sample demonstrates a T_c close to room temperature, making it a candidate for magnetic cooling materials, its relatively low entropy change suggests limitations in achieving high relative cooling power (RCP). The formation of BMO nanorods in LBMO was identified as another key factor affecting its magnetic properties. These nanorods can provide new magnetic interactions for nanosensors, field effect transistor (FET), ferroelectricity, energy storage, biosensors, dielectric materials and are thought to provide useful information in future studies [18]–[23]. Overall, this work adds new insights into the interaction between Ba substitution and the formation of BMO nanorods on LBMO. Additionally, our findings suggest that LBMO is a promising candidate for various applications, including spintronic devices, magnetic sensors, and other electronic devices. Moreover, the substitution of La with Ba in LBMO resulting in the formation of BaMnO₃ nanorods as the second step is thought to be due to the effect of a relatively low sintering temperature and rapid cooling process on the composite. This is a new observation and may have important implications in the development of new materials with specific magnetic properties. Our findings indicate that LBMO is a promising candidate for a wide range of applications and that Ba substitution can be used to tailor the magnetic properties of LBMO to specific applications.

Equations:

$$\chi = \frac{C}{T - \theta_{CW}} \quad (1)$$

$$\left(\frac{\partial S(H,T)}{\partial H}\right)_T = \left(\frac{\partial M(H,T)}{\partial T}\right)_H \quad (2)$$

$$\Delta S_M(T)_{\Delta H} = \int_0^H dS_M(T, H)_T = \int_{H_0}^{H_1} \left(\frac{\partial M(T, H)}{\partial T}\right)_H dH \quad (3)$$

$$-\Delta S_M(T, M) = \int_0^H \left(\frac{\partial M}{\partial T}\right)_H dH \quad (4)$$

$$-\Delta S_M(H, T) = \sum_i \frac{M_i - M_{i+1}}{T_{i+1} - T_i} \Delta H_i \quad (5)$$

Peer-review: Externally peer - reviewed.

Author contributions: Concept; Data Collection &/or Processing; Literature Search; Writing - Y. SAMANCIOĞLU.

Conflict of Interest: No conflict of interest was declared by the authors. (This paper has been presented at the ICENTE'23 (7th International Conference on Engineering Technologies) held in Konya (Turkey), November 23-25, 2023.)

Financial Disclosure: This investigation, Project No: 15/145, was supported by the Scientific Research Projects Coordination Unit (BAP) of Muğla Sıtkı Koçman University.

References

- [1] Keshri, S., Kumar, V., Wiśniewski P. & Kamzin, A.S. (2014). Synthesis and characterization of LSMO manganite-based biocomposite. *Phase Transitions*, 87 (5), 468-476.
- [2] Coşkun, A.T., Çetin, S. K. & Ekicibil, A. (2022). The investigation of the effect of K doping on the structural, magnetic, and magnetocaloric properties of $\text{La}_{1.4-x}\text{K}_x\text{Ca}_{1.6}\text{Mn}_2\text{O}_7$ ($0.0 \leq x \leq 0.4$) double perovskite manganite. *J Mater Sci: Mater Electron*, 33, 10990–11001.
- [3] Autreta, C., Martina, C., Hervieua, M., Maignana, A., Raveaua, B., Andreb, G., Bouree, F. & Jirakc, Z. (2003) From A-type antiferromagnetism to ferromagnetism in half-doped perovskite manganites. *Journal of Magnetism and Magnetic Materials*, 270, 194–202.
- [4] Trukhanov, S.V., Trukhanov, A.V., Stepin, S.G., Szymczak, H. & Botez, C.E. (2008). Effect of the Size Factor on the Magnetic Properties of Manganite $\text{La}_{0.5}\text{Ba}_{0.5}\text{MnO}_3$. *Physics of the Solid State-Magnetism and Ferroelectricity*, 50, 5, 886-893.
- [5] Gan, J., Hou, N., Yao, T., Fan, L., Gan, T., Huang, Z., Zhao, Y. & Li, Y. (2020). A high performing perovskite cathode with in situ exsolved Co nanoparticles for H_2O and CO_2 solid oxide electrolysis cell. *Catalysis Today*, 364, 89–96.
- [6] Liang, S., Xu, T., Teng, F., Zong, R. & Zhu, Y. (2010). The high activity and stability of $\text{La}_{0.5}\text{Ba}_{0.5}\text{MnO}_3$ nanocubes in the oxidation of CO and CH_4 . *Applied Catalysis B: Environmental*, 96, 267–275.
- [7] Spooen, J., Walton, R.I. & Millange, F. (2005). A study of the manganites $\text{La}_{0.5}\text{M}_{0.5}\text{MnO}_3$ (M= Ca, Sr, Ba) prepared by hydrothermal synthesis. *J. Mater. Chem.*, 15, 1542–1551.
- [8] Millange, F., Caignaert, V., Domenge`s, B. & Raveau, B. (1983). Order-Disorder Phenomena in New $\text{LaBaMn}_2\text{O}_{6-x}$ CMR Perovskites. *Crystal and Magnetic Structure*. *Chem. Mater.* 10, 1977.
- [9] Pękała, M., Drozd, V., Fagnard, J. F., Vanderbemden, P., & Ausloos, M. (2009). Magnetotransport of $\text{La}_{0.5}\text{Ba}_{0.5}\text{MnO}_3$. *Journal of Applied Physics*, 105(1).
- [10] Trukhanov, S.V., Trukhanov, A.V., Botez, C.E. & Szymczak, H. (2009). Magnetic Properties of the $\text{La}_{0.5}\text{Ba}_{0.5}\text{MnO}_3$ Nanomanganites. *Solid State Phenomena*, 152/153, 135-138.
- [11] Millange, F., Suard, E., Caignaert, V. & Raveau, B. (1999). YBaMn_2O_5 : crystal and magnetic structure reinvestigation. *Materials Research Bulletin*, 34, 1, 1-9.
- [12] Trukhanov, S. V., Trukhanov, A. V., Botez, C. E., & Szymczak, H. (2009). Magnetic properties of the $\text{La}_{0.50}\text{Ba}_{0.50}\text{MnO}_3$ nanomanganites. *Solid State Phenomena*, 152, 135-138.
- [13] Zhou, R., Yin, Y., Dai, H., Yang, X., Gu, Y., & Bi, L. (2023). Attempted preparation of $\text{La}_{0.5}\text{Ba}_{0.5}\text{MnO}_{3-\delta}$ leading to an in-situ formation of manganate nanocomposites as a cathode for proton-conducting solid oxide fuel cells. *Journal of Advanced Ceramics*, 12(6)
- [14] Xia, W., Leng, K., Tang, Q., Yang, L., Xie, Y., Wu, Z., & Zhu, X. (2021). Structural characterization and magnetic properties of single-crystalline $(\text{La}_{0.6}\text{Pr}_{0.4})_{0.67}\text{Ca}_{0.33}\text{MnO}_3$ nanowires. *Journal of the American Ceramic Society*, 104(10), 5402-5410.
- [15] Modeshia, D. R., & Walton, R. I. (2010). Solvothermal synthesis of perovskites and pyrochlores: crystallisation of functional oxides under mild conditions. *Chemical Society Reviews*, 39(11), 4303-4325.
- [16] Zhu, D., Zhu, H., & Zhang, Y. (2002). Hydrothermal synthesis of $\text{La}_{0.5}\text{Ba}_{0.5}\text{MnO}_3$ nanowires. *Applied physics letters*, 80(9), 1634-1636.

- [17] Chai, P., Liu, X., Wang, Z., Lu, M., Cao, X. & Meng, J. (2007). Tunable synthesis, growth mechanism, and magnetic properties of $\text{La}_{0.5}\text{Ba}_{0.5}\text{MnO}_3$. *Crystal Growth and Design*, 7(12), 2568-2575.
- [18] Hu C.G., Liu H., Lao C.S., Zhang L.Y., Davidovic D. & Wang Z.L. (2006). Size-manipulable synthesis of single-crystalline BaMnO_3 and $\text{BaTi}_{1/2}\text{Mn}_{1/2}\text{O}_3$ nanorods/nanowires. *J Phys Chem B.*, 110(29):14050-4.
- [19] Rondinelli, J. M., Eidelson, A. S. & Spaldin, N. A. (2009). Non-d 0 Mn-driven ferroelectricity in antiferromagnetic BaMnO_3 . *Physical Review B*, 79(20), 205119.
- [20] Kandemir, A., Akça, G., Kılıç Çetin, S., Ayaş, A. O., Akyol, M. & Ekicibil, A. (2023) Effects of Ca substitution on magnetic and magnetocaloric properties in $\text{PrBa}_{1-x}\text{Ca}_x\text{Mn}_2\text{O}_6$ system. *Journal of Solid State Chemistry*, 324, 124086.
- [21] Thakur, P., Kumari, S., Chaudhary, S., Sharma, N., & Lal, M. (2024). Multifunctional tuning of structural, dielectric, and magnetic properties of Ti-doped BaMnO_3 ceramics. *Emergent Materials*, 1-20.
- [22] Roisnel, T. & Rodriguez-Carvajal, J. (2003) Computer Program FULLPROF, LLB-LCSIM.
- [23] Terenti, N., Melnic, E., Fruth, V., Nedelko, N., Aleshkevych, P., Lewińska, S., Ślowska-Waniewska, A., Kravtsov, V. Ch., Lazarescu, A. & Lozan, V. (2023). Synthesis and microstructure of BaMnO_3 oxide obtained from coordination precursor, *Journal of Solid State Chemistry*, 324
- [24] Razmara, Z. (2019) Lanthanum (III) complex as ferromagnetic supraprecursor for preparation of La_2O_3 nanoparticles by thermal decomposition method. *Research on Chemical Intermediates*, 45, 2887-2901.
- [25] Pathan, A. A., Desai, K. R., Vajapara, S. & Bhasin, C. P. (2018) Conditional Optimization of Solution Combustion Synthesis for Pioneered La_2O_3 Nanostructures to Application as Future CMOS and NVMS Generations. *Advances in Nanoparticles* 7, 1, 28-35.
- [26] Mustofa, K., Yulizar, Y., Saefumillah, A. & Apriandanu, D.O.B. (2020). La_2O_3 nanoparticles formation using *Nothopanax scutellarium* leaf extract in two-phase system and photocatalytic activity under UV light irradiation. *IOP Conference Series: Materials Science and Engineering*, 902, 1, 012018.
- [27] Hu, C. G., Liu, H., Dong, W. T., Zhang, Y. Y., Bao, G., Lao, C. S. & Wang, Z. L. (2007). $\text{La}(\text{OH})_3$ and La_2O_3 Nanobelts- Synthesis and Physical Properties. *Advanced Materials*, 19, 3, 470-474.
- [28] Hu, C., Liu, H. & Wang, Z. L. (2008). Synthesis of Oxide Nanostructures. *BioNanofluidic MEMS*, 11-36.
- [29] Chau, N., Hanh, D. T., Tho, N. D. & Luong, N. H. (2006). Spin glass-like behavior, giant magnetocaloric and giant magnetoresistance effect in PrPb manganites. *Journal of Magnetism and Magnetic Materials*, 303(2), e335-e338.
- [30] Munazat, D. R., Kurniawan, B., Razaq, D. S., Manawan, M., Shon, W. H., Rhyee, J. S. & Nanto, D. (2024). Effect of Zn substitution on magnetic properties and magnetic entropy change in $\text{La}_{0.7}\text{Ba}_{0.25}\text{Nd}_{0.05}\text{Mn}_{1-x}\text{Zn}_x\text{O}_3$ ($x= 0.03$ and 0.05) synthesized by using sol-gel method. *Physica B: Condensed Matter*, 415800.
- [31] Al-Shahumi, T. M., Al-Omari, I. A., Al-Harathi, S.H. & Myint, M. T. Z. (2023) Synthesis, structure, morphology, magnetism, and magnetocaloric-effect studies of $(\text{La}_{1-x}\text{Pr}_x)_{0.7}\text{Sr}_{0.3}\text{MnO}_3$ nanocrystalline perovskites. *SN Applied Sciences*, 5, 121.

- [32] Iqbal, M., Nasir Khan, M., A.Khan, A., Zaka, I., Mehmood, A. & Ahmad, I. (2018). Investigation of Magnetic, Magnetocaloric, and Critical Properties of $\text{La}_{0.5}\text{Ba}_{0.5}\text{MnO}_3$ Manganite. *Journal of Superconductivity and Novel Magnetism*, 31, 3535–3544.
- [33] Zhu, D., Zhu, H., & Zhang, Y. (2003). Microstructure and magnetization of single-crystal perovskite manganites nanowires prepared by hydrothermal method. *Journal of Crystal Growth*, 249(1-2), 172-175.
- [34] Dinçer, İ. (2005). $\text{PrMn}_{1.6}\text{Fe}_{0.4}\text{Ge}_2$ Alaşımının Curie Sıcaklığı Üzerindeki Antiferromanyetik Yapısı. *Selçuk Üniversitesi Fen Fakültesi Fen Dergisi*, 1(26), 33-42.
- [35] Nakajima, T., Yoshizawa, H., & Ueda, Y. (2004). A-site randomness effect on structural and physical properties of Ba-based perovskite manganites. *Journal of the Physical Society of Japan*, 73(8), 2283-2291.
- [36] Kawasaki, Y., Minami, T., Fujishima, M., Kishimoto, Y., Ohno, T., Zenmyo, K., & Ueda, Y. (2006). Ground state properties of the A-site ordered/disordered manganites $\text{LaBaMn}_2\text{O}_6/\text{La}_{0.5}\text{Ba}_{0.5}\text{MnO}_3$ probed by NMR. *Physica B: Condensed Matter*, 378, 525-526.
- [37] Nagao, M., So, Y. G., Yoshida, H., Isobe, M., Hara, T., Ishizuka, K., & Kimoto, K. (2013). Direct observation and dynamics of spontaneous skyrmion-like magnetic domains in a ferromagnet. *Nature nanotechnology*, 8(5), 325-328.

Development Of Aluminum Matrix Rgo Reinforced Composites By Electric Current Assisted Sintering

*¹Yakup Pehlivan , ¹ Harun Gül 

¹ Sakarya Uygulamalı Bilimler Üniversitesi, Metalurji ve Malzeme Mühendisliği Bölümü, Sakarya, Türkiye.

* Sorumlu yazar, e-mail: yakuppehlivan@subu.edu.tr, <https://orcid.org/0000-0001-5412-1324>

Submission Date: 30.04.2024

Acceptation Date: 28.06.2024

Abstract

In this study, reduced graphene oxide (rGO) reinforced composites with aluminium matrix were fabricated by using powder metallurgy method by current assisted sintering (ECAS). The average grain size of aluminium used in the produced samples is 20 microns and composite materials were obtained by means of 2 to 5 layers of reduced graphene oxides. For this purpose, pure aluminium, 3%, 8% and 16% rGO doped composite materials were produced by ECAS method under 2000A/14 min conditions. Scanning electron microscopy (SEM) and X-ray diffraction analysis (XRD) techniques were used for the characterisation of the composites. Corrosion tests were also carried out to determine the electrochemical behaviour of the composites. Aluminium matrix composite structures with homogeneous distribution were obtained with increasing rGO reinforcement. The presence of rGO phase was also confirmed by XRD analysis. As a result of electro chemical tests, it was determined that corrosion resistance increased with increasing rGO reinforcement. It was revealed that the material with the highest corrosion resistance was obtained with aluminium matrix composite material containing 16% rGO. However, the highest hardness value in composite materials was found in the composite material containing 3% rGO, while the optimum result in terms of wear resistance and friction coefficient was reached in the composite material with the lowest graphene oxide content (3% rGO).

Keywords: Aluminium, rGO, ECAS, Sintering, Corrosion, Wear resistance

Elektrik Akım Destekli Sinterleme Yöntemiyle Alüminyum Matrisli Rgo Takviyeli Kompozitlerin Geliştirilmesi

Öz

Bu çalışma da toz metalürsiji yönteminden faydalanarak alüminyum matrisli indirgenmiş grafen oksit (rGO) takviyeli kompozitler akım destekli sinterleme yöntemi ile (ECAS) üretilmiştir. Üretilen numularda kullanılan alüminyumun ortalama tane boyutu 20 mikron olup 2 ile 5 tabakalı indirgenmiş grafen oksitler aracılı ile kompozit malzemeler elde edilmiştir. Bu amaçla saf alüminyum, %3, %8 ve %16 rGO katkılı kompozit malzemeler ECAS yöntemi ile 2000A/14 dk şartlarında üretilmiştir. Üretilen kompozitlerin karakterizasyonu için taramalı elektron mikroskobu (SEM) ve X ışınları kırınım analizi (XRD) tekniklerinden faydalanılmıştır. Ayrıca kompozitlerin elektro kimyasal davranışlarını belirlemek amacıyla korozyon testi yapılmıştır. Artan rGO takviyesi ile homojen dağılıma sahip alüminyum matrisli kompozit yapılar elde edilmiştir. rGO fazının varlığı XRD analizi ile de doğrulanmıştır. Elektro kimyasal testler sonucunda artan rGO takviyesi ile korozyon dayanımının arttığı tespit edilmiştir. En yüksek korozyon dayanımına sahip malzemenin de

¹ Corresponding author: Tel: 0 264 616 01 63

E-mail: yakuppehlivan@subu.edu.tr

%16 rGO içeren alüminyum matrisli kompozit malzeme ile elde edildiği ortaya konmuştur. Bununla birlikte kompozit malzemelerde en yüksek sertlik değeri %3 rGO içeren kompozit malzemede olduğu, aşınma dayanımı ve sürtünme katsayısı açısından ise optimum sonuca yine en düşük grafen oksit içeren (%3 rGO) kompozit malzemede ulaşılmıştır.

Anahtar kelimeler: Alüminyum, rGO, ECAS, Sinterleme, Korozyon, Aşınma

1. Giriş

Alüminyum, kimyasal sembolü Al olan ve 13 numaralı atomu bulunan bir metaldir. Doğada genellikle bauxit adı verilen bir mineral içerisinde bulunur ve bauxit madenciliği ve işlenmesi yoluyla elde edilir (Compston et al., 2004). Bu metal, hafifliği, iletkenlik özelliği, korozyona direnci ve şekillendirilebilirliği ile bilinir (Aluminium - Element Information, Properties and Uses | Periodic Table).

Alüminyumun geniş kullanım alanları ve avantajları, endüstriyel ve tüketici ihtiyaçlarını karşılamak için önemli bir malzeme haline gelmesini sağlar (Callister & Rethwisch, 2018).

Grafit: Karbon bazlı bir mineral olan grafit, atomları aralıklı yatay katmanlar halinde düzenlenmiş altı karbon halkasından oluşan katmanlı bir yapıya sahiptir. Oktahedral veya tetrahedral sistemde kristalleşen elmasların aksine, grafit altıgen sistemde kristalleşerek bu element formları arasında belirgin bir yapısal varyasyon sergiler. Dimorfik çiftler genellikle benzer fiziksel özellikler sergiler; ancak grafit ve elmas söz konusu olduğunda kayda değer farklılıklar ortaya çıkar. Grafit doğal olarak oluşan, koyu griden siyaha kadar değişen renklerde, opak ve son derece yumuşak (Mohs ölçeğine göre 1 1/2 puan) bir yapıya sahipken, elmaslar şeffaf ve renksiz olabilir ve olağanüstü sertlikleriyle tanınırlar. Grafit ayrıca yağlı bir doku sergiler (Bi et al., 2023).

Grafen oksit, karbon ve oksijen atomlarından oluşan bir karbon nanomaterialidir. Bu materyal, grafenin oksitlenmiş bir formudur ve grafenin bir türevidir (Flora et al., 2023). Grafen, tek atom kalınlığında karbon atomlarının düzenli bir şekilde düzlem halinde bir araya gelmesiyle oluşurken, grafen oksit ise grafen yapısının bazı karbon atomlarının oksijen atomlarıyla yer değiştirmesi ya da oksijen gruplarının grafen tabakasının üzerine yerleştirilmesi sonucu elde edilir (Edokali et al., 2023).

Doğal grafit öğütülerek saf hale getirilir ve sonra oksitlenme işlemine tabi tutulur. Bu işlem, grafen tabakalarının oksitlenmesini sağlayarak grafen oksit oluşturur (Rudenko et al., 2023). Oluşan grafen oksit yıkanarak temizlenir ve ardından kurutulur. Üretilen grafen oksit örnekleri daha sonra incelenerek özellikleri belirlenir. Grafen oksit üretimi karmaşık bir süreç olup, son ürünün özellikleri üretim adımlarına ve kullanılan tekniklere bağlı olarak değişebilir (Le et al., 2023).

Grafen oksit, grafit tabakalarının oksitlenerek ayrılmış tek katmanlı bir forma dönüşmesidir (Schniepp et al., 2006). Bu materyal, genellikle karbon ve oksijen atomlarından oluşur ve genellikle C:O oranı 3'ten düşüktür, tipik olarak ise yaklaşık olarak 2'ye yakın bir orana sahiptir. Grafen oksit, çeşitli fonksiyonel grupları içerir (Kerli et al., 2017).

Grafenin büyük miktarlarda üretimi için öne çıkan bir yöntem, kimyasal proseslerle üretilen grafen oksidin farklı yöntemlerle indirgenmesidir (Chen et al., 2010). Verimli üretim için düşük maliyetli grafit hammaddelerinin tercih edilmesi, aynı zamanda elde edilen grafitin suya karşı çekim gücünü artırarak stabil çözeltiler hazırlama imkanı tanır. Bu yöntem, grafenin ölçeklendirilebilir ve maliyet etkin olarak üretilmesini sağlar (Bianco et al., 2013).

Grafen oksitin indirgenmesi, oksijen içeren grupların parçalanmasıyla grafen oksidin yalnızca karbon içeren bir forma dönüşümünü ifade eder. Grafen oksidin indirgenmesi sadece yüksek sıcaklıkla gerçekleştirilerek mümkündür, bu işleme termal tavlama yöntemi adı verilir. Grafenin ilk

araştırma aşamalarında, ani ısıtma ($2000\text{ }^{\circ}\text{C}$) yöntemi grafen oksitin eksfoliasyonu için kullanılıyordu. Ani ısıtılan grafit oksit tabakaları arasında CO ve CO₂ gazlarının oluşturduğu basınç, eksfoliasyonu sağlıyordu. Bu yöntemde eksfoliye edilen tabakalar, doğrudan grafen olarak adlandırılabilir çünkü ani ısıtma işlemi oksijen içeren grupların ayrışmasını ve gaz halinde grafitin oksit tabakalarından uzaklaşmasını sağlayarak bir indirgeme işlemi gerçekleştirir. Bu yöntem, hem eksfoliasyon hem de indirgeme sağladığı için başlangıçta avantajlı gibi görünse de, üretim miktarlarının az olması ve yüksek sıcaklıkta grafitin tabakalarının kısmen bozulması gibi nedenlerle tercih edilen bir yöntem değildir (Schniepp et al., 2006).

Grafitin oksitin grafene indirgenmesi sürecinde, görsel olarak renkte kahverengiden siyaha doğru bir değişim gözlemlenir. Bu değişim, oksijen içeren grupların grafitin oksit yapısından uzaklaşmasıyla bağlantılıdır (Fernández-Merino et al., 2010). Bu süreç aynı zamanda aglomerasyona, yani partiküllerin bir araya gelerek küme oluşturmaya da neden olabilir. Çözeltinin rengindeki değişim, oksijen oranının azalması ve iletkenliğin artması gibi faktörlerle ilişkilidir. Bu değişimler, indirgeme işleminin ne ölçüde gerçekleştirildiğine dair birer gösterge olarak kabul edilir. Örneğin, daha az oksijen içeriği ve artan iletkenlik, grafitin oksitin grafitte indirgenmesinin gerçekleştiğini işaret edebilir (Chua & Pumera, 2014).

Çeşitli kimyasal yöntemler, grafitin oksitin indirgenmesi için kullanılan farklı indirgeyici ajanları içermektedir. Bu yöntemlerin arasında hidrazinler, borhidritler, alüminyumhidritler ve sülfür içeren maddeler gibi bir dizi seçenek bulunmaktadır. Bunların yanı sıra, çevre dostu yaklaşımların bir parçası olarak askorbik asit gibi maddeler de grafitin oksitin indirgenmesinde tercih edilmektedir. Bu farklı indirgeyici maddeler, grafitin oksit yapısının indirgenmesi sürecinde kullanılarak, grafitin özelliklerinde ve son uygulamalarda sağladığı etkilerde farklılıklar ortaya çıkarılabilir (Chen et al., 2010; Fernández-Merino et al., 2010).

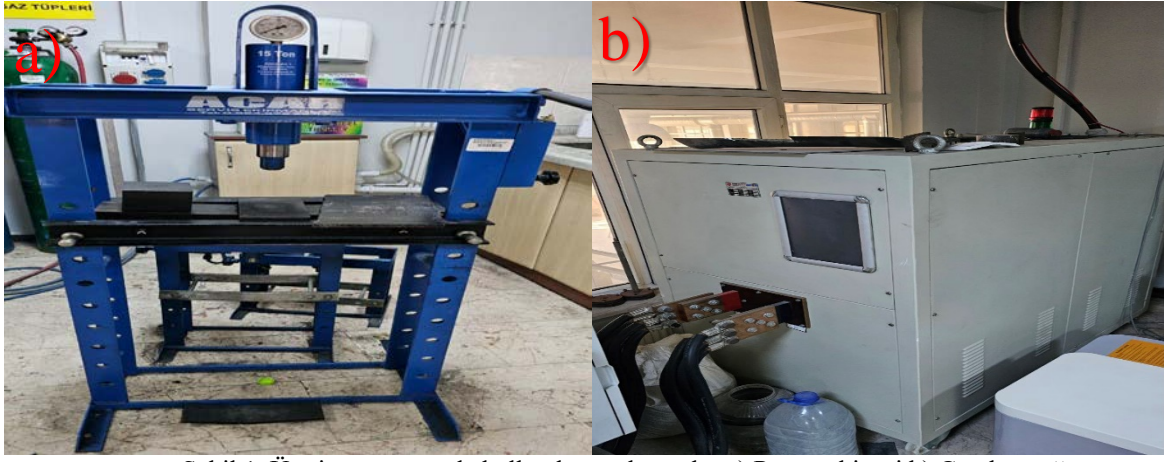
2. Deneysel Çalışmalar

Bu çalışmada, alüminyum matrisli rGO takviyeli kompozitlerin üretiminde elementel tozlar kullanılarak hazırlanan toz karışım elektrik akımı destekli sinterleme (1400-2000A/14 dak) yöntemleriyle üretilmiştir. Üretimi gerçekleştirilen numunelerin, SEM görüntüleri ile mikroyapıları, kantitatif noktasal EDS analizleri ve x-ışın paternleri ile faz yapıları, vickers mikrosertlik testleri ile sertlik değişimleri, ball on disc yöntemiyle aşınma özellikleri ve elektro-kimyasal korozyon çalışmaları ile korozyon özellikleri tespit edilmiştir. Elde edilen kompozit kaplamaların hem yüzey hem de kesitleri mikroyapısal olarak incelenmiştir. Bu amaçla SEM (Jeol JSM-6060 LV) cihazları kullanılarak görüntüleme yapılmıştır. Mikrosertlik ölçümü WILSON HARDNESS 402M VD marka model cihaz kullanılarak yapılmıştır. Kompozit kaplamalarda elde edilen kompozit yapıların fazlarının belirlenmesi için RIGAKU D MAX 2200 PC marka x-ışınları difraktometresi kullanılmıştır. Korozyon ölçümleri, oda sıcaklığında, Gamry marka bilgisayar kontrollü test cihazıyla yapılmıştır. Deneysel, üç elektrot tekniği kullanılarak bir deney cam hücresinde gerçekleştirilmiştir. Korozyon testlerinde %3,5'lik bir NaCl çözeltisi kullanılmıştır. Numunelerin nihai şeklini alması ve ECAS tekniğiyle üretim için bu haznelerde şekillendirme işleminin gerçekleştirilmesi amacıyla tasarlanmış olan şekillendirme kalıpları, talaşlı imalat yöntemleriyle üretilmiştir. Kalıplar, AISI 4140 malzemesinden yapılmış olup matris çapı 30 mm ve yüksekliği 45 mm ölçülerindedir. Üretim sonrası elde edilen numuneler, 5 mm kalınlık ve 30 mm çapta nihai şekle sahiptir.

Bu çalışmada Alüminyum ile indirgenmiş Grafitin oksit bir bileşik oluşturacak şekilde tasarlanmış ve içeriğine %3, 8 ve 16 oranında rGO ilavesi yapılarak özelliklerindeki değişim incelenmiştir. Üretimi gerçekleştirilen numunelerin kompozisyon aralığı Tablo 1'de verilmiştir. Kullanılan grafitin oksit tozlarının ortalama tane boyutu 20 mikrondur. Ayrıca üretim aşamasında kullanılan pres ve güç kaynağı şekil 1'de gösterilmiştir.

Tablo 1. Üretim aşamasında kullanılan tozlar ve ağırlıkça dağılımları

Numune	Elementlerin % Dağılımları (Ağırlıkça %)	
	Al	rGO
1	100	-
2	97	3
3	92	8
4	84	16



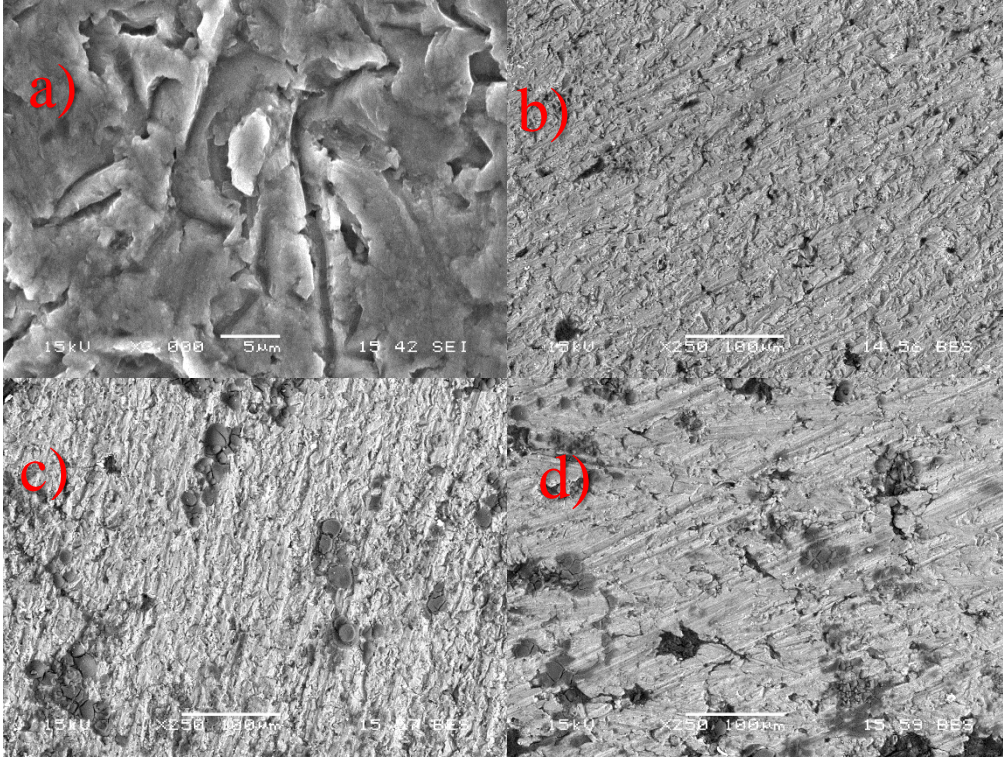
Şekil 1. Üretim aşamasında kullanılan malzemeler a) Pres makinesi b) Güç kaynağı

3. Deneysel Sonuçlar

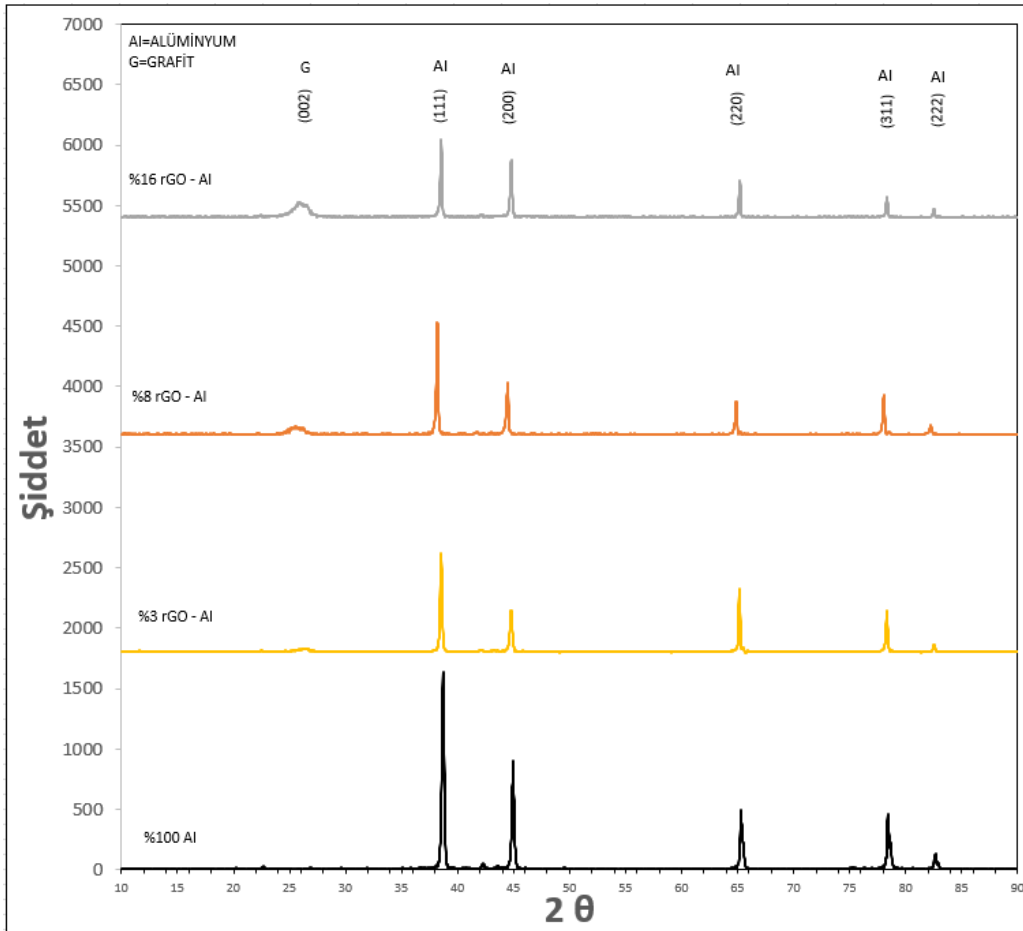
Şekil 2’de saf alüminyum ve %3, %8 ve %16 rGO takviyeli kompozit malzemelere ait SEM görüntüleri görülmektedir. SEM görüntüleri incelendiğinde artan rGO takviyesi ile birlikte daha fazla rGO karbon yapısı içine girmiş ve homojenliğin arttığı görülmüştür. Beyaz açık renkli parlak gözüken alanlar alüminyumu gösterirken siyah koyu renkli alanlar da karbonu yani rGO’yu ifade etmektedir.

ECAS tekniğiyle hazırlanan, elementel tozların homojen karışımıyla elde edilen saf Alüminyum ve rGO takviyeli kompozit malzemede oluşan farklı fazları belirlemek için X-ışını difraksiyon yöntemi kullanılmıştır. Şekil 2’de saf alüminyum ve sırasıyla %3, %8 ve %16 rGO takviyeli kompozitlerin XRD analizleri sunulmuştur.

Şekil 3. de verilen XRD analizi incelendiğinde saf Alüminyum için farklı düzlemlerde alüminyum pikleri yer almaktadır. Kompozit malzemeler için bir değerlendirme yapıldığında ise yaklaşık 2 teta=25 derecede grafitte ait piklerin varlığı grafen oksit varlığını doğrulamaktadır. Kompozit malzemelerde artan rGO miktarı ile birlikte 25 derecede yer alan grafit piklerinin şiddetlerinin arttığı anlaşılmaktadır. Özellikle ağırlıkça % 8 rGO (0,25g) içeren ve daha yüksek konsantrasyonlarda grafit piklerinin daha belirgin hale geldiği görülmektedir. Bu durum da daha fazla grafen oksitin alüminyum matris içerisine girdiğini doğrulamaktadır. Grafen oksit takviyesi aynı zamanda farklı düzlemlerdeki alüminyum piklerinin şiddetinin de azalmasına sebep olduğu görülmektedir. Özellikle (111) ve (220) düzlemlerinde bu pik şiddetlerinde ki azalma bariz bir şekilde görülmektedir.



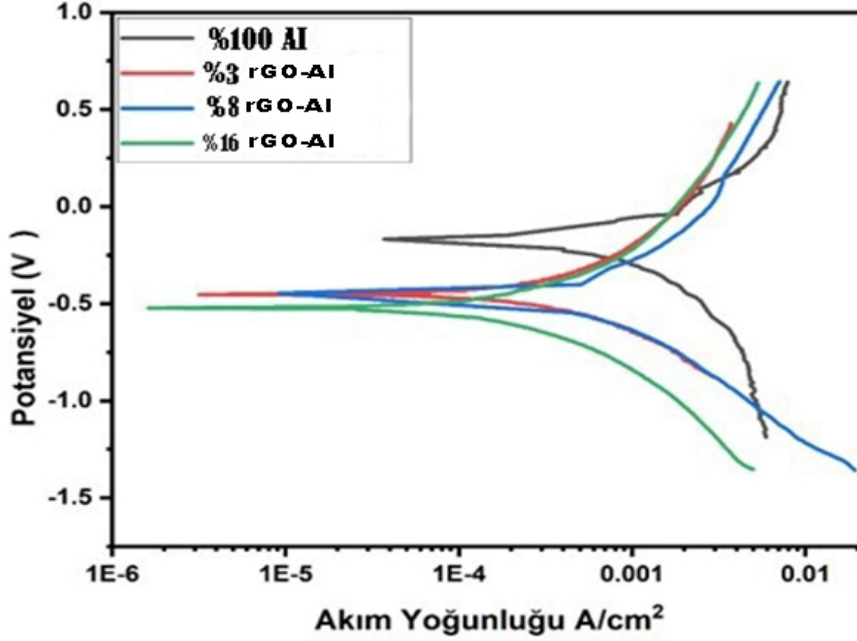
Şekil 2. Alüminyum alaşım ve rGO takviyeli kompozit malzemelerin mikroyapı görüntüleri a) Saf Al, b) %3 rGO-Al, c) %8 rGO-Al, d) %16 rGO-Al



Şekil 3. Saf Alüminyum ve rGO takviyeli kompozit malzemelerin XRD analizi

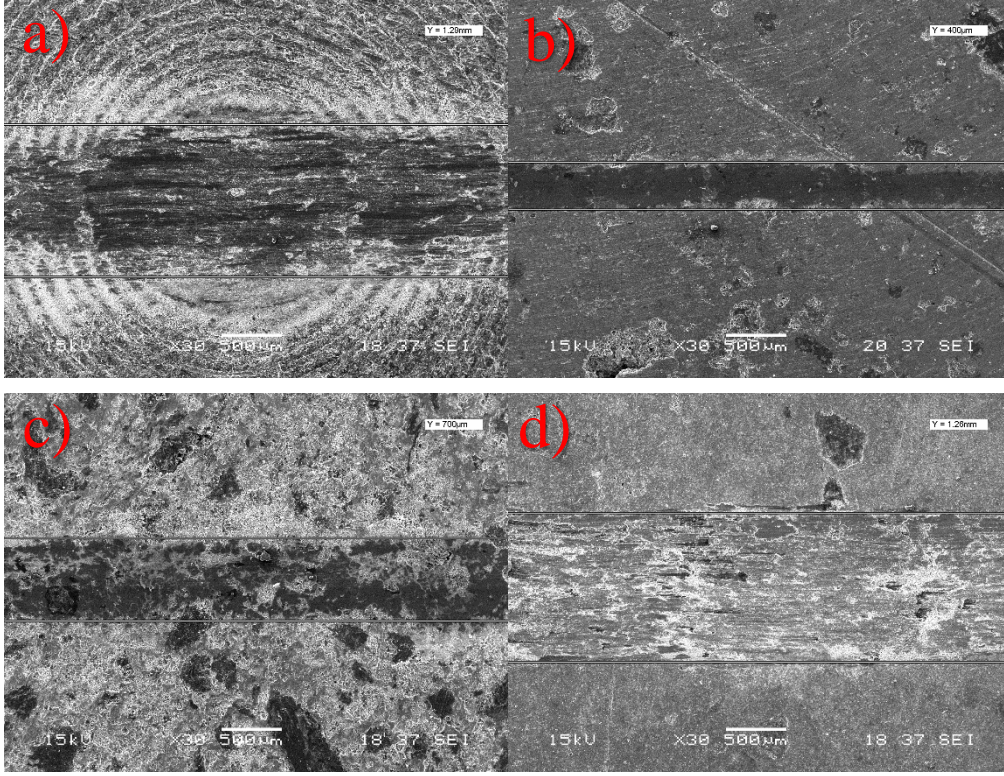
Grafen oksit takviyesi aynı zamanda Alüminyum piklerinin şiddetinin de azalmasına sebep olduğu görülmektedir.

ECAS tekniğiyle oluşturulan, elementel tozların homojen karışımıyla elde edilen saf alüminyum ve rGO takviyeli kompozit malzemelerin %3.5'lik NaCl çözeltisinde elektrokimyasal korozyon deneyleri gerçekleştirilmiştir. -1V ile +1V arasında değişen potansiyel aralığında 0,5mV/sn tarama hızıyla Tafel eğrileri elde edilmiştir. Saf alüminyum ve rGO takviyeli kompozitlerin Tafel eğrileri Şekil 4'de gösterilmiştir.



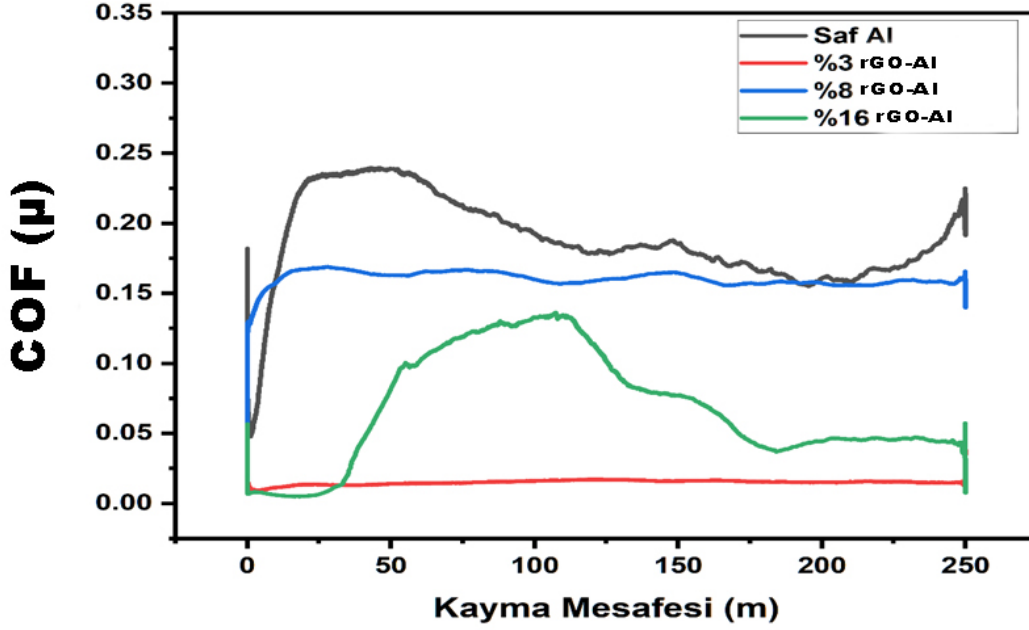
Şekil 4 : %3,5 NaCl çözeltisi ile yapılan elektrokimyasal test sonuçları - tafel eğrileri

Saf alüminyum ve rGO takviyeli kompozitler için tafel eğrileri değerlendirildiğinde saf alüminyumda her ne kadar enpozitif potansiyel söz konusu olsa da akım açısından değerlendirildiğinde en yüksek akım değerine sahip olduğu anlaşılmaktadır. Bu durumda korozyon davranışı kötü olacaktır. Kompozit malzemeler kendi içerisinde değerlendirildiğinde ise %16 rGO takviyeli kompozit malzemedeki en düşük akım yoğunluğu söz konusu olduğu görülmektedir. Buna rağmen potansiyel açısından diğer katkılı yüzdeleri kompozitlere yakın olmakla beraber en negatif potansiyel değeri en yüksek katkılı kompozit malzemenin sergilediği anlaşılmaktadır. Sonuç olarak potansiyel ve akım açısından değerlendirildiğinde en yüksek katkılı kompozitin (%16) en yüksek korozyon direncine sahip olacağı anlaşılmaktadır.



Şekil 5: Numunelerin Sem görüntüleri a) % 100 Al, b) %3 rGO, c) %8 rGO, d) % 16 rGO

Aşınma testleri sonrası yüzeyden alınan SEM görüntülerinden aşınma izlerinin genişlikleri tespit edilmiş olup grafen oksit konsantrasyonuna bağlı olarak iz genişliklerinde ki değişim şekil 5.4.'de verilmiştir. Sem görüntüleri incelendiğinde takviyesiz yani saf alüminyum, aşınma sonrası yaklaşık 1,30 mm iz genişliğine sahip olduğu anlaşılmaktadır. Grafen oksit takviyeli kompozitlerde ise takviye fazının artışına bağlı olarak ters orantılı bir ilişki söz konusudur. En düşük grafen oksit konsantrasyonu olan %3 GO takviyeli alüminyum matrisli kompozit malzemede aşınma sonrası iz görüntüsü incelendiğinde (Şekil 5/b) iz genişliğinin 400 μ m değerine kadar düştüğü görülmektedir. Ancak artan konsantrasyon ile sırası ile 700 μ m ve 1,26 mm lik iz genişlikleri elde edilmiştir. Azalan konsantrasyon ile iz genişliklerinde meydana gelen düşüş aşınma dayanımında artışı ortaya koymaktadır. Artan konsantrasyon ile aşınma dayanımında meydana gelen düşüşün sebepleri ortaya konmaya muhtaçtır. Muhtemel sebepler olarak artan konsantrasyon ile ara yüzey mukavemetindeki muhtemel bozulma ve yine artan konsantrasyon ile mikro gözeneklilik-porozitedeki artışlar sayılabilir.



Şekil 6: Sürtünme katsayısı -Kayma mesafesi

Sürtünme katsayıları ile kayma mesafeleri kompozit ve alaşım için Şekil 6.'da verilmiştir. Grafik incelendiğinde saf alüminyumun en yüksek sürtünme katsayısı sergilediği görülmektedir. Kompozit malzemeler için grafik incelendiğinde ise şekil 5'de verilen iz genişliklerindeki ilişki ile örtüşen şekilde en düşük sürtünme katsayısı en düşük grafen oksit konsantrasyonu içeren kompozit malzemede (%3 GO) elde edildiği görülmektedir. Daha yüksek konsantrasyonlarda ise sürtünme katsayısında artış ve sürtünme katsayısı kararlılıklarında bozulma olduğu anlaşılmaktadır. Ayrıca en yüksek konsantrasyon olan %16 grafen oksit içeren kompozit malzemedeki davranışın daha düşük katsayısına sahip olmak ile birlikte saf alüminyuma benzer olduğu görülmektedir.

Sertlik değerlerinin tespiti, numunelerin mekanik özellikleri hakkında bilgi vermesi açısından oldukça önemlidir. Mikrosetrlilik cihazında Vickers sertlik ucu kullanılarak yapılan ölçümlerin sonucunda saf Alüminyum malzemesinin sertlik değeri 47,8 HV, %3 GO içeriğine sahip malzemenin sertlik değeri 44.5 HV, %8 GO içeriğine sahip malzemenin sertlik değeri 39.7 HV, %16 GO içeriğine sahip malzemenin sertlik değeri 33.5 HV olarak tespit edilmiştir. Bu deneyler sonucunda numunede GO içeriğinin artması ile sertlik değerinin azaldığı tespit edilmiştir.

4. Sonuçlar

- ECAS yöntemiyle saf Alüminyum ve rGO takviyeli kompozitleri (%3, %8 ve %16) başarılı bir şekilde üretilmiştir. Elde edilen sonuçlar aşağıda maddeler halinde sunulmuştur.
- XRD analizi ile rGO katkılı kompozitlerin üretildiği ve rGO fazının varlığı 2 teta=25 derecede doğrulanmıştır.
- Üretilen kompozitlere ait mikro yapı görüntüleri SEM aracılığı ile verilmiş olup görüntülerden kompozitlerin başarılı bir şekilde üretildiği anlaşılmaktadır. Takviye miktarına bağlı olarak takviye fazının yapı içerisinde homojen bir şekilde dağıtıldığı ortaya konmuştur.
- Saf Alüminyum ve kompozitlerden alınan korozyon test sonuçları en yüksek korozyon direncine sahip malzemenin en yüksek katkılı kompozite ait olduğunu göstermiştir. Artan takviye oranı korozyon dayanımının artmasına sebep olmuştur.

- Kompozit malzemelerde en yüksek sertlik değeri %3 rGO içeren kompozit malzemede 44.5 HV olarak elde edilmiştir.
- Aşınma dayanımı ve sürtünme katsayısı açısından optimum sonuca en düşük grafen oksit içeren (%3 rGO) kompozit malzemede ulaşılmıştır.

Hakem değerlendirmesi: Harici hakem değerlendirmesi.

Yazar katkıları: Veri Toplama ve/veya İşleme - Y.P.; Literatür Taraması, Yazım -H.G.

Çıkar Çatışması: Yazarlar tarafından herhangi bir çıkar çatışması beyan edilmemiştir

Finansal Açıklama: Yazarlar bu çalışmanın finansal destek almadığını beyan etmişlerdir

Kaynaklar

- Aluminium - Element information, properties and uses | Periodic Table. (n.d.). Retrieved November 21, 2023, from <https://www.rsc.org/periodic-table/element/13/aluminium>
- Bi, Y., Xing, Y., He, J., Qin, Y., Zhao, H., & Li, Y. (2023). Effect of graphite addition on microstructure and properties of TiC–Ti5Si3–SiC composite coatings reacted from Ti–SiC-graphite powders. *Journal of Materials Research and Technology*, 27, 6211–6224. <https://doi.org/10.1016/J.JMRT.2023.11.032>
- Bianco, A., Cheng, H. M., Enoki, T., Gogotsi, Y., Hurt, R. H., Koratkar, N., Kyotani, T., Monthieux, M., Park, C. R., Tascon, J. M. D., & Zhang, J. (2013). All in the graphene family – A recommended nomenclature for two-dimensional carbon materials. *Carbon*, 65, 1–6. <https://doi.org/10.1016/J.CARBON.2013.08.038>
- Callister, W. D., & Rethwisch, D. G. (2018). *Materials Science and Engineering AN INTRODUCTION*. [https://ftp.idu.ac.id/wp-content/uploads/ebook/tdg/TEKNOLOGI%20REKAYASA%20MATERIAL%20PERTAHANAN/Materials%20Science%20and%20Engineering%20An%20Introduction%20by%20William%20D.%20Callister,%20Jr.,%20David%20G.%20Rethwisch%20\(z-lib.org\).pdf](https://ftp.idu.ac.id/wp-content/uploads/ebook/tdg/TEKNOLOGI%20REKAYASA%20MATERIAL%20PERTAHANAN/Materials%20Science%20and%20Engineering%20An%20Introduction%20by%20William%20D.%20Callister,%20Jr.,%20David%20G.%20Rethwisch%20(z-lib.org).pdf)
- Chen, W., Yan, L., & Bangal, P. R. (2010). Chemical reduction of graphene oxide to graphene by sulfur-containing compounds. *Journal of Physical Chemistry C*, 114(47), 19885–19890. https://doi.org/10.1021/JP107131V/ASSET/IMAGES/MEDIUM/JP-2010-07131V_0005.GIF
- Chua, C. K., & Pumera, M. (2014). Chemical reduction of graphene oxide: A synthetic chemistry viewpoint. *Chemical Society Reviews*, 43(1), 291–312. <https://doi.org/10.1039/C3CS60303B>
- Compston, P., Cantwell, W. J., Cardew-Hall, M. J., Kalyanasundaram, S., & Mosse, L. (2004). Comparison of surface strain for stamp formed aluminum and an aluminum-polypropylene laminate. *Journal of Materials Science*, 39(19), 6087–6088. <https://doi.org/10.1023/B:JMISC.0000041707.68685.72/METRICS>
- Edokali, M., Bocking, R., Mehrabi, M., Massey, A., Harbottle, D., Menzel, R., & Hassanpour, A. (2023). Chemical modification of reduced graphene oxide membranes: Enhanced desalination performance and structural properties for forward osmosis. *Chemical Engineering Research and Design*, 199, 659–675. <https://doi.org/10.1016/J.CHERD.2023.10.022>
- Fernández-Merino, M. J., Guardia, L., Paredes, J. I., Villar-Rodil, S., Solís-Fernández, P., Martínez-Alonso, A., & Tascón, J. M. D. (2010). Vitamin C is an ideal substitute for hydrazine in the reduction of graphene oxide suspensions. *Journal of Physical Chemistry C*, 114(14), 6426–6432. https://doi.org/10.1021/JP100603H/SUPPL_FILE/JP100603H_SI_001.PDF
- Flora, B., Kumar, R., Tiwari, P., Kumar, A., Ruokolainen, J., Narasimhan, A. K., Kesari, K. K., Gupta, P. K., & Singh, A. (2023). Development of chemically synthesized hydroxyapatite composite with reduced graphene oxide for enhanced mechanical properties. *Journal of the Mechanical Behavior of Biomedical Materials*, 142, 105845. <https://doi.org/10.1016/J.JMBBM.2023.105845>
- Kerli, S., Sistemleri Mühendisliği Bölümü, E., Teknoloji Fakültesi, E., Sütçü İmam Üniversitesi, K., & Geliş, T. (2017). İNDİRGENMİŞ GRAFEN OKSİT-ÇİNKO OKSİT-TİTANYUM DİOKSİT KOMPOZİT MALZEME ÜRETİMİ VE UYGULAMASI. *Niğde Ömer Halisdemir Üniversitesi Mühendislik Bilimleri Dergisi*, 6(1), 220–225. <https://doi.org/10.28948/NGUMUH.298162>

- Le, H. N., Thai, D., Nguyen, T. T., Dao, T. B. T., Nguyen, T. Do, Tieu, D. T., & Ha Thuc, C. N. (2023). Improving safety and efficiency in graphene oxide production technology. *Journal of Materials Research and Technology*, 24, 4440–4453. <https://doi.org/10.1016/J.JMRT.2023.04.050>
- Rudenko, R. M., Voitsihovska, O. O., & Poroshin, V. N. (2023). Enhancement of electrical conductivity of hydrazine-reduced graphene oxide under thermal annealing in hydrogen atmosphere. *Materials Letters*, 331, 133476. <https://doi.org/10.1016/J.MATLET.2022.133476>
- Schniepp, H. C., Li, J. L., McAllister, M. J., Sai, H., Herrera-Alonson, M., Adamson, D. H., Prud'homme, R. K., Car, R., Seville, D. A., & Aksay, I. A. (2006). Functionalized single graphene sheets derived from splitting graphite oxide. *The Journal of Physical Chemistry. B*, 110(17), 8535–8539. <https://doi.org/10.1021/JP060936F>

Blood Glucose Level Estimation Using Photoplethysmography (PPG) Signals with Explainable Artificial Intelligence Techniques

*¹Gökhan ADIGÜZEL  0009-0004-1545-5427,

²Ümit ŞENTÜRK  0000-0001-9610-9550,

³Kemal POLAT  0000-0002-7201-6963.

¹ Bolu Abant İzzet Baysal University, Faculty of Engineering, Computer Engineering Depart., Bolu, Turkey.

* Corresponding author, e-mail: gokhanadiguzel1@gmail.com,

² Bolu Abant İzzet Baysal University, Faculty of Engineering, Computer Engineering Depart., Bolu, Turkey.
e-mail: umit.senturk@ibu.edu.tr,

³ Bolu Abant İzzet Baysal University, Faculty of Engineering, Electric and Electronic Engineering Depart., Bolu, Turkey. e-mail: kpolat@ibu.edu.tr.

Submission Date: 24.04.2024

Acceptation Date: 28.04.2024

Abstract - Estimating blood sugar levels is a critical task in effective diabetes management. This study focuses on leveraging the power of machine learning models such as CatBoost, XGBoost, and Extra Trees Regressor, along with explainable AI techniques like SHAP values and confusion matrices, to predict blood sugar levels using Photoplethysmography (PPG) signals. The dataset used in this research is carefully selected for glucose prediction from PPG signals and consists of data from 217 individuals. Information for each individual includes laboratory glucose measurements and approximately one minute of recorded finger PPG signals. Among the various machine learning models tested, CatBoost emerged as the best-performing model in predicting blood sugar levels. The CatBoost model demonstrated its efficiency and accuracy in glucose level predictions by achieving an impressive coefficient of determination (R^2) of 0.71 and a mean absolute error (MAE) of 25.21. Feature importance analysis highlighted the significance of specific features like median deviation and kurtosis in the predictive model built with CatBoost, emphasizing their critical role in determining blood sugar levels. The inclusion of explainable AI techniques enhanced the interpretability and transparency of predictive models. In conclusion, this research underscores the potential of machine learning-based approaches in predicting blood sugar levels from PPG signals. By leveraging advanced models like CatBoost and utilizing explainable AI methods, this study paves the way for improved diabetes management through accurate, non-invasive, and data-driven predictive methodologies.

Keywords: Blood Sugar Prediction, Photoplethysmography, Machine Learning, SHAP, XAI

Açıklanabilir Yapay Zeka Teknikleri ile Fotopletismografi (PPG) Sinyalleri Kullanarak Kan Glikoz Seviyesi Tahmini

Öz - Kan şekeri seviyelerinin tahmini, diyabetin etkili yönetiminde kritik bir görevdir. Bu çalışma, Fotopletismografi (PPG) sinyallerini kullanarak kan şekeri seviyelerini tahmin etmek için CatBoost, XGBoost ve ekstra ağaç regresör gibi makine öğrenimi modellerinin gücünden, SHAP değerleri ve karışıklık matrisi gibi açıklanabilir yapay zekâ teknikleriyle birlikte yararlanmaya odaklanıyor. Bu çalışmada kullanılan veri seti, PPG sinyallerinden glikoz tahmini için dikkatlice seçilmiştir ve 217 kişiden alınan verilerden oluşmaktadır. Her bireyin bilgileri, laboratuvar glikoz ölçümlerini ve yaklaşık bir dakikalık kaydedilen parmak PPG sinyallerini içerir. Test edilen çeşitli makine öğrenimi modelleri arasında CatBoost, kan şekeri seviyelerini tahmin etmede en iyi performansı gösteren model olarak ortaya çıktı. CatBoost modeli, 0.71'lik etkileyici bir determinasyon katsayısı (R^2) metriğine ve 25.21'lik ortalama mutlak hataya (MAE) ulaşarak glikoz seviyesi tahminlerindeki verimliliğini ve doğruluğunu ortaya koydu. Özellik önemi analizi, CatBoost ile oluşturulan tahmin modelinde medyan fark ve basıklık gibi belirli özelliklerin önemini vurgulayarak bunların kan şekeri seviyelerinin belirlenmesindeki önemli rolünün altını çizdi. Açıklanabilir yapay zekâ tekniklerinin dâhil edilmesi, tahmine dayalı modellerin yorumlanabilirliğini ve şeffaflığını arttırdı. Sonuç olarak bu araştırma, PPG sinyallerinden kan şekeri seviyelerinin tahmin edilmesinde makine öğrenimine dayalı yaklaşımların potansiyelini vurgulamaktadır. CatBoost gibi gelişmiş modellerden yararlanan ve açıklanabilir yapay zekâ yöntemlerini kullanan bu çalışma, doğru, invaziv olmayan ve veriye dayalı tahmine dayalı metodolojiler yoluyla gelişmiş diyabet yönetiminin yolunu açıyor.

Anahtar kelimeler: Kan Şekeri Tahmini, Fotopletismografi, Makine Öğrenmesi, SHAP, Açıklanabilir Yapay Zeka

1. Introduction

Diabetes is a significant health issue that affects both individuals and society on a global scale[1]. According to the World Health Organization (WHO), diabetes is considered a major global

health problem and an escalating epidemic[2]. In 2000, the global prevalence of diabetes across all age groups was 2.8%, approximately affecting 171 million people. By 2030, it is estimated to rise to 4.4%, impacting around 366 million people[3]. Diabetes occurs when the pancreas fails to produce enough insulin, or when the body's cells and tissues are unable to effectively use the insulin that is produced[4]. This leads to abnormal levels of glucose in the blood. In healthy individuals, blood glucose levels typically range between 70 and 99 mg/dL. Those with a glucose concentration ranging from 100 to 125 mg/dL are classified as being prediabetic[5]. Refer to Table 1 for the diabetes diagnosis values.[6]

Table 1. Diabetes diagnosis values

Condition	Fasting Blood Sugar (mg/dL)	Oral Glucose Tolerance Test (OGTT) 2 hours after (mg/dL)	Hemoglobin A1c (HbA1c) (%)
Normal	70-99	< 140	< 5.7
Prediabetes	100-125	140-199	5.7-6.4
Diabetes	≥ 126	≥ 200	≥ 6.5

Fasting Blood Sugar (FBS): Blood sugar level measured after at least 8 hours of fasting.

Oral Glucose Tolerance Test (OGTT): Blood sugar level measured 2 hours after consuming 75 grams of glucose.

Hemoglobin A1c (HbA1c): A blood test that indicates the average blood sugar level over the past 2-3 months.

Diabetes can have lasting effects on a person's quality of life. It is a physiological dysfunction characterized by high blood sugar levels due to insufficient insulin, insulin resistance, or excessive glucagon production [7]. Long-term diabetes can lead to chronic complications such as heart disease, kidney disease, stroke, vision loss, and nervous system damage [8]. It can also be a cause of early death for patients with long-term complications. Higher blood sugar levels, known as hyperglycemia, can cause the thickening of blood vessels, leading to kidney damage, vision loss, and sometimes even organ failure. Diabetes is also associated with limb amputation, peripheral vascular diseases, and myocardial issues.

Today, both invasive and non-invasive methods are used to measure blood sugar. These methods describe different approaches for medical diagnosis or monitoring. Invasive Measurement Method: Invasive measurement methods involve gathering information by entering the body or penetrating the skin. These methods typically offer direct access to the patient's internal organs and are used in various medical procedures. For instance, cardiac catheterization is commonly used for diagnosing heart diseases and conducting surgical procedures, while blood sampling is a standard practice for laboratory tests. In general, invasive measurement methods provide more accurate results by directly accessing the target organ or tissue inside the body. As a result, they are preferred for the diagnosis and treatment of critical illnesses. Non-Invasive Measurement Method: Non-invasive measurements gather information without penetrating the body or with minimal contact. Patient preferences often lean towards less invasive non-invasive methods due to the potential risks and discomfort associated with invasive methods, especially for the monitoring of chronic diseases. Non-invasive methods are generally preferred for monitoring chronic diseases because they are more frequently used and less invasive. Non-invasive measurement methods generally provide less accurate results compared to invasive methods because they collect information from outside the body. However, advancements in technology are improving the accuracy of non-invasive methods.

Both invasive and non-invasive measurement methods require physical contact. However, non-invasive methods are limited to the skin surface, causing less discomfort than invasive methods. Patients often prefer non-invasive methods due to their lower invasiveness, reduced risk, and increased comfort. Factors such as patient comfort, lower costs, and reproducibility contribute to the popularity of non-invasive methods. However, the severity of the disease and specific monitoring parameters may sometimes necessitate the use of invasive methods. Table 2 displays the features of invasive and non-invasive blood glucose measurement methods currently in use.

Table 2. Invasive and non-invasive blood glucose measurement methods

Method	Description	Invasive/Non-invasive
Fingerstick Testing (Blood Glucose Test) [6]	Uses a needle or lancet to collect a blood sample from the fingertip, which is measured with a glucose meter.	Invasive
Continuous Glucose Monitoring (CGM) [9]	A sensor placed under the skin continuously measures blood glucose levels and transmits data to a monitor or smartphone.	Non-invasive
Intravenous Blood Sampling [10]	Blood samples are taken intravenously for laboratory tests and analysis.	Invasive
Electrochemical Methods [11]	Uses electrodes to measure glucose levels in a blood sample. Glucose reacts with an enzyme, producing an electrical signal proportional to glucose amount.	Invasive
Transdermal Glucose Monitoring [12]	A device placed on the skin measures glucose levels through the skin using technologies like electromagnetic waves or ultrasound.	Non-invasive
Saliva or Tear Analysis [13]	Measures glucose levels in body fluids like saliva or tears, still in research and development stages.	Non-invasive.
Optical Sensors[14]	Uses optical sensors, like laser light or infrared light, to determine glucose levels.	Non-invasive
Bioelectrical Impedance Analysis[15]	Measures electrical properties of the body to determine glucose levels with electrodes placed on the skin's surface.	Non-invasive

Non-invasive methods are preferable for continuous glucose monitoring compared to invasive and semi-invasive methods[16]. Optical methods have been found to be more reliable and accurate in glucose measurement[17]. Common optical methods for non-invasive measurements include Raman spectroscopy, near-infrared spectroscopy, polarimetry, scattering spectroscopy[18], photoacoustic spectroscopy [19], and others. Non-invasive measurements can address previous issues and provide painless and accurate solutions [16]. By using a non-invasive method, blood sampling is eliminated, reducing the risk of bacterial and viral infections, as well as alleviating patient discomfort. The following are the application steps for invasive and non-invasive methods.

Traditional Blood Glucose Measurement System: This system is invasive and is generally used as part of the initial insulin-based treatment. These types of devices are typically glucose monitors used in conjunction with active medication therapy and rely on advanced optical sensor technology. Optical sensor technology, applied solely for the detection of glucose, allows for the direct acquisition of data. The primary purpose of a glucose monitor is to detect the maximum glucose level in the body. However, since these monitors can increase the risk of infections, there is a need for alternative methods. For patients to measure their blood sugar levels at home, they require the devices and equipment shown in Figure 1. Once the devices and equipment are obtained, the patient begins a difficult and sometimes painful process. The traditional blood sugar measurement procedure is usually not something the patient can do alone.



Figure 1: Blood glucose measurement device and equipment.

Precautions need to be taken both before and after the measurement. The finger from which the measurement will be taken must be kept sterile to prevent infection. The stages of blood sugar measurement at home are shown in Figure 2 below.

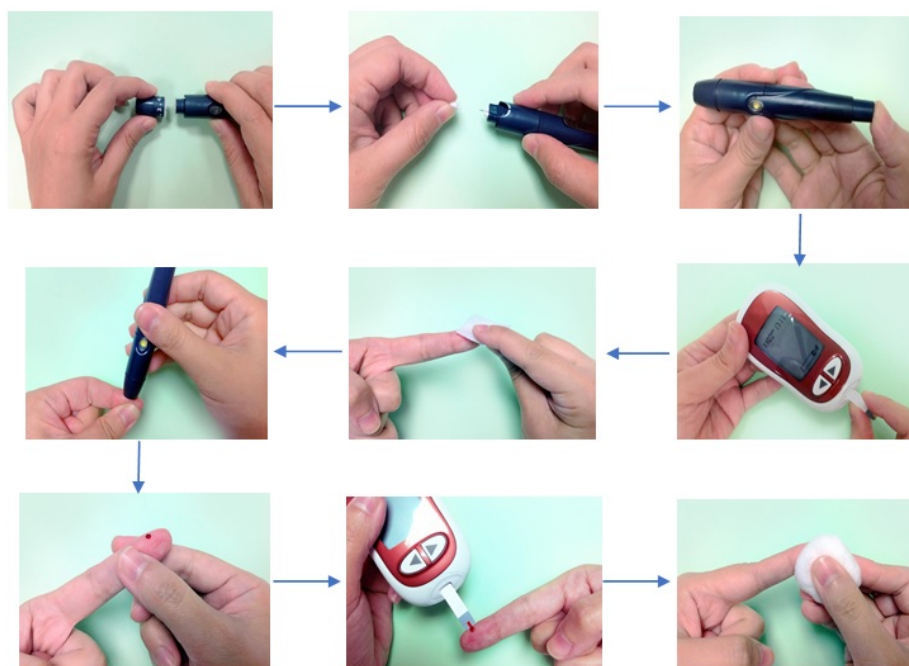


Figure 2. Stages of blood sugar measurement at home.

Traditional methods for determining blood glucose levels include using subcutaneous measurements and invasive interventions. In cases where continuous monitoring is necessary, a sensor is implanted under the patient's skin to constantly track glucose levels. These sensors continuously take and record measurements. This procedure is typically carried out in a hospital setting under the supervision of a physician. Research on electrochemical measurement systems aims to reduce sensor sizes and improve measurement accuracy. In a study conducted by Kubilay A., Hakan B., and their colleagues, a reusable and enzyme-free sensor was developed. The absence of enzymes in these sensors helps to reduce potential complications in the body. [20]

In a study by Fatemeh Karimi and colleagues, economical production methods were used to create enzyme-free sensors[21]. The developed sensor was found to be extremely stable, discriminative, and sensitive, indicating its potential as a glucose sensor for the market. These sensors are designed to overcome the disadvantages of traditional glucose sensors and invasive methods, offering the potential to improve glucose detection systems in the future.

In addition to electrochemical measurements, it's important for patients to measure blood sugar without invasive interventions. Continuous measurements are necessary to prevent the disease from reaching severe levels. Although the size of interventional method sensors has been reduced and enzyme-free sensors have been developed, traditional methods are uncomfortable for the patient and time-consuming. Therefore, the development of noninvasive blood glucose measurement systems is crucial. Measures can be taken to achieve noninvasive blood sugar measurement in the least painful and shortest time by utilizing signals received from the body. Photoplethysmography (PPG) sensors are used to measure these signals. These sensors work by using light to measure blood flow and volume and are often used to monitor heart rate, blood oxygen saturation (SpO₂) and other cardiovascular parameters [22]. The signal measurement system of the PPG sensor is shown in Figure 3. The potential of artificial intelligence is revealed when analyzing PPG signals. As shown in Figure 4, signals measured with the PPG sensor require interpretation that involves a complex set of mathematical operations. This process is difficult and cumbersome to accomplish with human intelligence and effort alone.

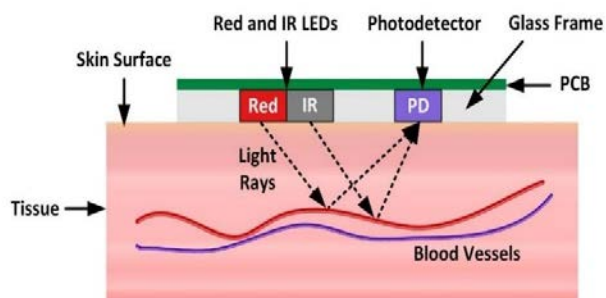


Figure 3: PPG signal measurement system

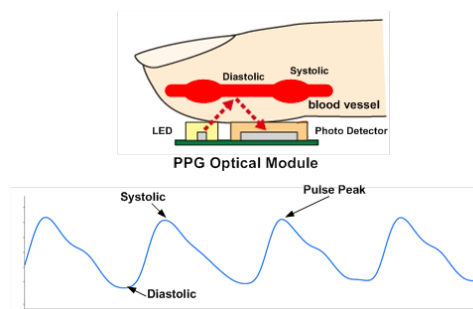


Figure 4: PPG sensor signal

With the advancement of AI algorithms, it is now feasible to improve the accuracy of non-invasive blood sugar measurements. This study seeks to gauge blood sugar levels without invasive procedures, such as drawing blood. The use of non-invasive systems is expected to provide unbiased data, potentially enhancing the effectiveness of diabetes treatment.

2. Materials and Methods

The methodological steps in the study were started with the data set being read and the data being preprocessed. The signals were first passed through a filter. This step usually involves the data being cleaned, noise being removed, and the signals being converted into a format suitable for further processing. After filtering, the cleaned signals were subjected to feature extraction. This step involves relevant features or characteristics being identified and extracted from the signals that are informative and useful. In the next phase, the training phase, the relationship between the features and the target variable was learned by the model. Finally, the final output of the process was a trained regression model. This model was used to predict blood glucose levels based on new input signals using the relationships learned during the training phase. These steps are illustrated in Figure 5.

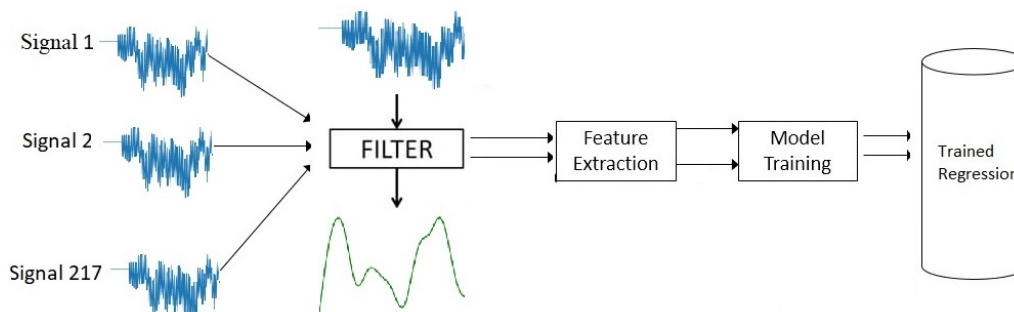


Figure 5: Workflow Steps

2.1. Dataset

In the development of the proposed system, the database in the literature was taken into account [23]. This database contains glucose values from 217 participants (127 women and 90 men) and PPG signal values from a clinical-chemical and immunology analysis unit (Cobas 6000) at a hospital in Cuenca, Ecuador. The PPG signal was collected for an average of 2.5 minutes at a sampling frequency of 64 Hz using the Empatica E4 wristband. The wristband uses green (550 nm) and red (650 nm) lights to optimize pulse wave detection [24]. The glucose value obtained in the laboratory environment was also assigned as the target variable.

2.2. Data Preprocessing

The first 10 seconds of data were removed from the signal to avoid errors due to device initial parameters. Signal preprocessing was performed using the NeuroKit2 library [25] and the Elgendi [26] method was used to remove noise and artifacts in PPG signals. In Figure 6, the Elgendi method,

known as broadband amplitude integration, was used to display the raw signal and the cleaned signal. The Elgendi method is used to evaluate the broadband characteristics of the PPG signal. Additionally, this method is effective in improving the quality of the PPG signal and integrating amplitudes into specific frequency bands.

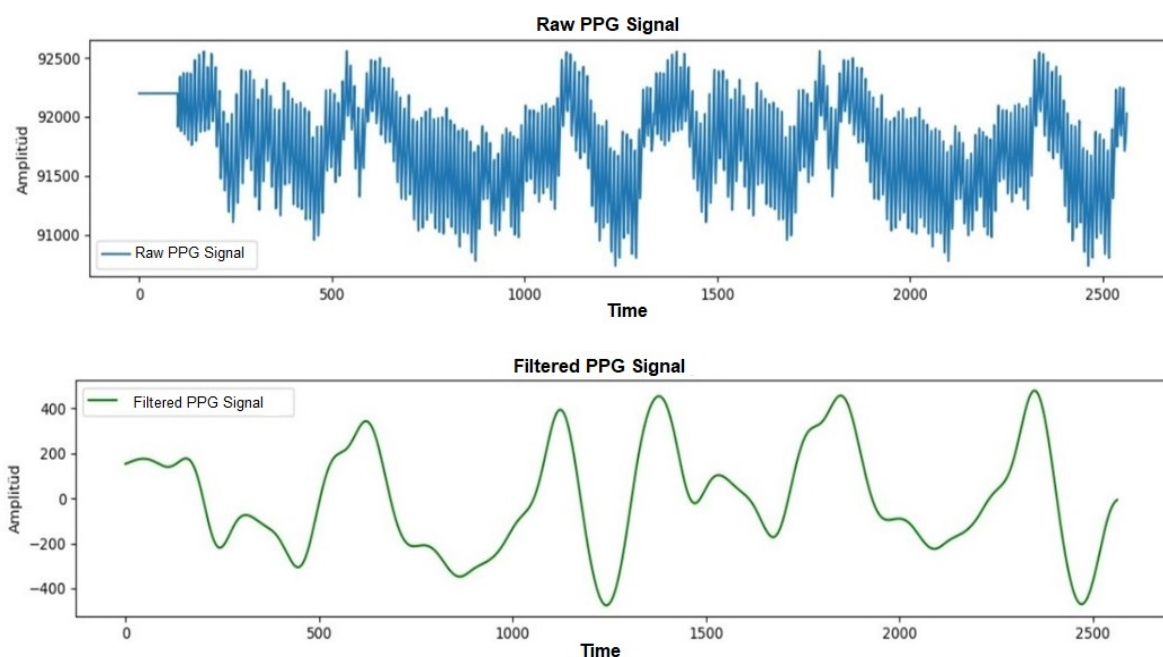


Figure 6: Signal Processing Steps

The PPG signal is obtained by detecting light that is reflected or absorbed from tissues and blood vessels in the body. This signal is commonly used in pulse measurements and medical monitoring applications. The Elgendi method is employed in the analysis of pulse waves in PPG signals, aiming to determine the frequency, amplitude, and phase changes of the pulse waves. This method relies on a customized wavelet transform technique to extract prominent features of the pulse waves. The Elgendi method is a widely used and effective technique in processing PPG signals. It plays a significant role in various application domains such as medical diagnosis, health monitoring, and sports performance monitoring, as it allows for the extraction and analysis of prominent features of pulse waves.

2.3. Segmentation

The segmentation of a Photoplethysmography (PPG) signal involves dividing it into specific events or periods. This signal typically represents the heart cycle, and segmentation is used to identify particular events or features within the cycle. Various methods can be used for PPG signal segmentation, such as R-peak detection, inverted peak detection, start and end of heartbeats, and frequency domain analysis. In this study, PPG signals were segmented based on the start and end intervals of heartbeats, as shown in Figure 7.

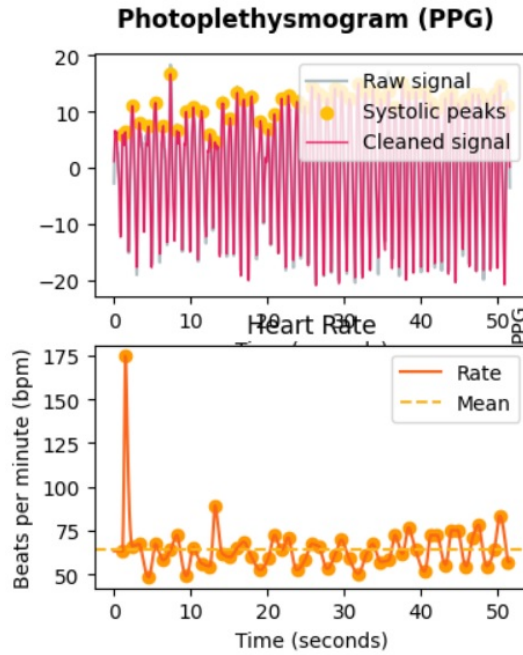


Figure 7: Segmentation Process

Segmented PPG signals were averaged to make it easier to analyze specific events or conditions. Averaging is particularly useful when working with repeated cycles, such as a PPG signal, as it allows us to identify the characteristics of each cycle. Figure 8 showed the starting and ending values as well as the average value of the heartbeat of patient number 3. The dark red line represents the average heart rate, and the light thin lines represent all heartbeats of the patient.

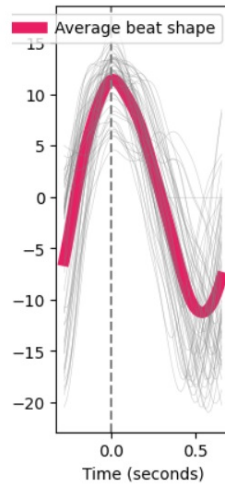


Figure 8: Segmentation Process

2.4. Feature Extraction and Selection

PPG signals were preprocessed using the TSFEL[27] library, a Python library designed to extract various features from time series data, and then converted them into features. The library provides a wide range of feature extraction functions and capabilities for generating a feature matrix. Available features are divided into three categories: statistical, temporal and spectral. In the study, temporal and statistical features were used to divide the PPG signal into 230 features. Some features, such as the maximum value of a signal, ECDF value calculated over time (empirical cumulative distribution function), and signal entropy, were excluded from the study because they did not

contribute to blood glucose prediction. A total of 51 signal features were ultimately used for the prediction calculation, and Table 3 contains a list of some of the features used.

Table 3. Some of the Features to be Used

PPG Features	Description
1	Peak value
2	Peak-to-peak
3	Mean value
4	Standard deviation
5	Root Mean Square (RMS)
6	Skewness
7	Kurtosis
8	Crest factor
9	Impulse factor

- 1- **Peak Value:** It represents the highest value of a time series. This value determines the peak of the time series and represents the maximum value that occurs over a certain period. Identifying the highest value in time series is especially important in areas such as anomaly detection, signal processing, and data mining.[28]
- 2- **Peak-to-Peak:** It refers to the difference between the highest (peak) and lowest (trough) points of a time series. This metric is used to measure the fluctuation amplitude of the signal and represents the variability or fluctuation range of the time series.[28]
- 3- **Mean Value:** It is the value obtained by dividing the sum of the elements of a time series or data set by the number of elements. The mean is used as a measure of central tendency and represents the overall trend or typical value of the data set.[28]
- 4- **Standard Deviation:** It is a statistical value that measures how much the elements in the data set deviate from the average. Standard deviation is used to understand the spread or dispersion of a data set and shows how the data is distributed around the mean.[28]
- 5- **Root Mean Square(RMS):** It is a measure defined as the square root of the mean square value of a data set. RMS is used primarily in fields such as signal processing, engineering, and statistics and represents the energy content or amplitude level of a data set.[28]
- 6- **Skewness:** It is a statistical measure that describes the asymmetry of data distribution around the mean. Indicates whether data points are denser on one side of the average than the other. Skewness can be positive, negative, or zero, and each case tells us something different about the shape of the data distribution.[29]
- 7- **Kurtosis:** It is a statistical measure that describes the shape of a distribution's tails about its overall shape. It indicates whether the data points in the tails of the distribution are heavy or light compared to a normal distribution. In other words, kurtosis measures the "tailedness" or the extremity of deviations in a dataset.[29]
- 8- **Crest Factor:** It is a measure expressing the ratio of the peak value of a signal or data set to the average value. It is often used in fields such as electrical engineering, audio engineering, and signal processing. The crest factor determines the relationship between the peak value and average value of a signal and provides information about the amplitude of the signal.[30]
- 9- **Impulse Factor:** This is the ratio of the highest amplitude (peak) value of a signal to the duration of the signal. Impulse factor is used to describe the pulse-shaped characteristic of a signal and provides information about the overall performance of the signal.[28]

The signals, separated according to the determined features, were associated with the glucose values obtained in the laboratory as the target variable and prepared for the machine learning model.

2.5. Machine Learning Model

PPG signals were subjected to preprocessing and feature extraction before being regressed with the target variable. Regression involves modeling and understanding the relationship between



variables, which is commonly used to analyze the relationship between the dependent variable (outcome variable) and the independent variables (predictor variables). In our research, regression models in the Pycaret [31] library were used to model the relationship between the target variable and one or more independent variables. These models help us understand how a variable depends on other variables and predict future values. We used a series of regression models to increase training depth. The performance values of the first seven regression models are presented in Table 4, and the performance values of all regression models are detailed in the results section.

Table 4. Performance Values of the First Seven Regression Models

Model	MAE	MSE	RMSE	R ²	RMSLE	MAPE	TT(Sec)
CatBoost Regressor	25.162	1591.7898	39.1387	0.7191	0.2436	0.1837	31.150
Light Gradient Boosting Machine	28.6411	1941.9567	43.4559	0.6553	0.2692	0.2029	0.0250
Extra Trees	26.9872	2095.2192	44.5275	0.6428	0.2790	0.1996	0.0770
Gradient Boosting Regressor	29.9443	2368.1302	47.9978	0.5960	0.2870	0.2084	0.0880
AdaBoost Regressor	36.7854	2400.9081	48.2477	0.5890	0.2951	0.2612	0.0420
Random Forest Regressor	29.5800	2493.4937	48.9901	0.5693	0.2932	0.2089	0.1030
Extreme Gradient Boosting	30.9313	2833.0924	52.1906	0.5263	0.3067	0.2164	0.2100

The table includes various metrics that measure the performance of different machine-learning models. For each model, mean absolute error (MAE), mean square error (MSE), root mean square error (RMSE), coefficient of determination (R²), root mean square logarithmic error (RMSLE), mean absolute percentage error (MAPE) and training It is seen that it is evaluated with metrics such as duration (TT). MAE (Mean Absolute Error): Indicates the average absolute difference between the actual values and the predicted values by the model. A lower value indicates better prediction performance [32]. MSE (Mean Squared Error): Indicates the average squared difference between the actual values and the predicted values by the model. A lower value indicates better prediction performance [33]. RMSE (Root Mean Squared Error): Obtained by taking the square root of MSE. It represents the square root of the average squared difference between the actual and predicted values. A lower value indicates better prediction performance [34]. R² (R-squared): Indicates the percentage of variation in the dependent variable explained by the independent variables. Values range from 0 to 1, where a higher value indicates a better fit of the model [35]. RMSLE (Root Mean Squared Logarithmic Error): Represents the square root of the average squared difference between the logarithms of the actual and predicted values. Particularly useful when there are large values in the dataset [36]. MAPE (Mean Absolute Percentage Error): Represents the average absolute percentage difference between the actual and predicted values. A lower value indicates better prediction performance [37]. TT (Training Time): Represents the training time of the model. A shorter time indicates faster training time. In the trained system used in the study, two models with the highest performance among regression models were analyzed: CatBoostRegressor [38] and LightGBM (Light Gradient Boosting Machine) [39]. CatBoost directly supports categorical variables in regression tasks. This allows users to use categorical variables without the need for special handling or conversion. CatBoost is based on the gradient boosting algorithm. Gradient boosting aims to create a strong model by combining weak learners, usually decision trees. LightGBM (Light Gradient Boosting Machine) provides fast training on large datasets and datasets with high-dimensional features by using parallel processing and a specialized histogram-based learning method.

2.6. Explainable Artificial Intelligence (SHAP)

In this study, Feature Importance Graph was used instead of performance data. Figure 9 shows the Feature Importance Graph of the CatBoostRegressor algorithm, which achieved the highest performance metric. A Feature Importance Graph is a graph that visualizes the contribution of features (variables or attributes) in a machine learning model to the model's performance. It helps understand the impact on the model's output by ranking each feature in order of importance.

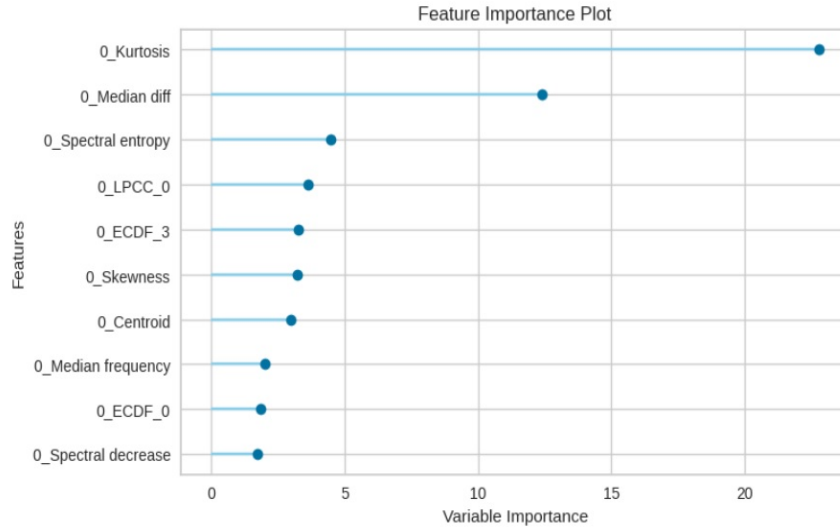


Figure 9: Feature Importance Plot for the CatBoostRegressor Algorithm

In the study, the performance of the Light Gradient Boosting Machine algorithm, which is the second high-performance algorithm used, was analyzed. In examinations of both training and testing data, the algorithms showed similar performance metrics. However, differences were observed in the Feature Importance Graph. Comparison of the CatBoostRegressor algorithm with the Light Gradient Boosting Machine algorithm revealed differences in feature ranking between the two regression algorithms. These differences in feature importance rankings are shown in Figure 10.

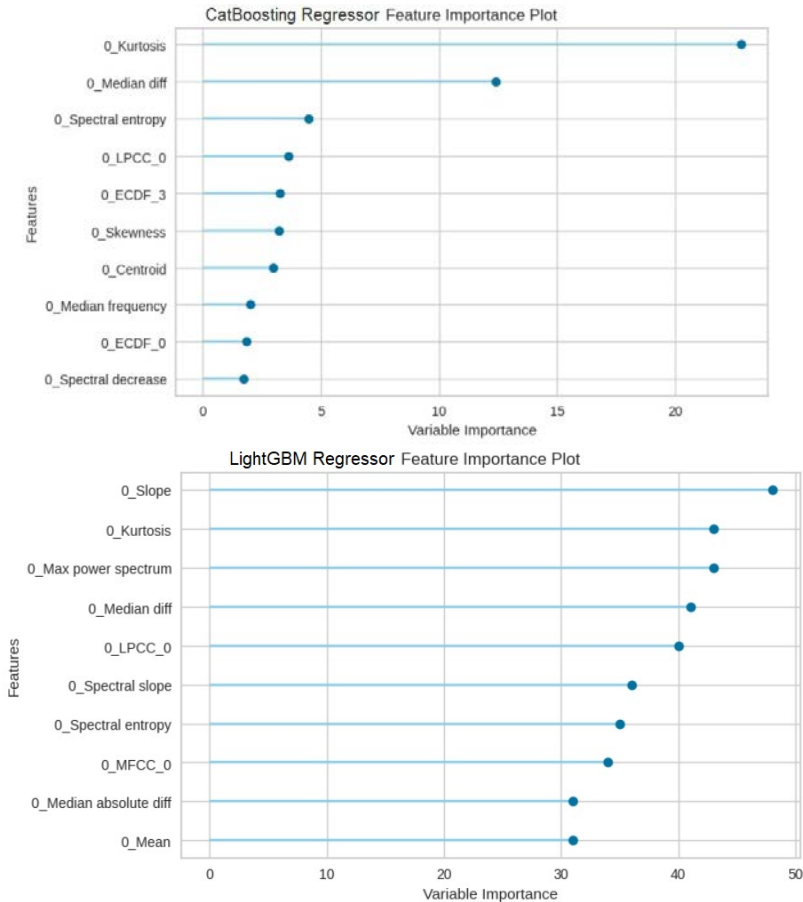


Figure 10: CatBoostRegressor - Light Gradient Boosting Machine Feature Importance Plot Comparison

The two graphs show the varying cardinality of the CatBoost and LightGBM regression algorithms. Both algorithms work on a specific data set to determine which features are more important when predicting the target variable.

Kurtosis: It is seen as a very important feature in both models. Kurtosis formulas given formula 1. This suggests that this feature plays a critical role when predicting the target variable in the dataset.

Median Diff: While it is very important in the CatBoost model, it ranks fourth in the LightGBM model. This difference may be due to the different algorithmic structures of the two models. **Slope:** While it is considered the most important feature in LightGBM, it is not even among the top 10 features in the CatBoost model. This may give a clue as to how features are evaluated in different models.

Other Features: Different features stand out in both models. For example, while 0_Spectral entropy was found to be significant in both models, 0_Spectral decrease was only significant in the CatBoost model. This analysis is useful for understanding which features are consistently important across both models and which features vary from model to model. This information can be taken into account during model selection and improvement.

The Kurtosis [40] value, the most important determining feature in the CatBoostRegressor algorithm, is a measure that represents how peaked or flat a data set is, typically compared to a normal distribution. It indicates the degree to which data points are more or less sharply distributed.

$$\text{Kurtosis} = \frac{n * \sum_{i=1}^n i \Sigma n_i (Y_i - \bar{Y})^4}{(\sum_{i=1}^n i (Y_i - \bar{Y})^2)^2} \quad (1)$$

Y_i: Distribution Variable i

\bar{Y} : Mean of the Distribution

n: Number of Variables in the Distribution

In the Light Gradient Boosting Machine algorithm, the most significant determining feature is the Slope [40] function. The Slope function calculates the slope of a data series. The slope represents the rate of change in a data series and indicates the steepness of a line or curve in two-dimensional space.

$$y = ax + b,$$

y = Dependent Variable

a = Coefficient

x = Independent Variable

b = Constant Value

2.7. Blood Glucose Level Prediction

The study aimed to evaluate the performance of various regression models and select the best performers for further analysis. After evaluating different metrics, the regression models with the highest performance were determined. These models were then retrained using the dataset to ensure optimal performance. A “prediction error” plot was used to gain insight into the performance of the selected models and to understand how well they predicted the target variable. This type of chart is commonly used in data analysis and machine learning to visualize disparities between actual values

and predicted values generated by the model. In general, the prediction error chart serves as a visual tool to evaluate the performance of regression models and identify areas for improvement. It helps researchers and analysts make informed decisions about the reliability and effectiveness of models in predicting the target variable.

3. Results and Discussions

The study compared regression models trained with relevant settings and parameters in the data. The performance metrics used were Mean Absolute Error (MAE), Mean Square Error (MSE), Root Mean Square Error (RMSE), R-squared (R^2), Root Mean Square Logarithmic Error (RMSLE), and Mean Absolute Percentage Error. (MAPE). Performance metrics for all regression models are shown in Table 5.

Table 5. Performance Metrics Based on Regression Models

Model	MAE	MSE	RMSE	R^2	RMSLE	MAPE	TT(Sec)
CatBoost Regressor	25.16	1591.78	39.13	0.71	0.24	0.18	31.15
Light Gradient Boosting Machine	28.64	1941.95	43.45	0.65	0.26	0.20	0.02
Extra Trees	26.98	2095.21	44.52	0.64	0.27	0.19	0.07
Gradient Boosting Regressor	29.94	2368.13	47.99	0.59	0.28	0.20	0.08
AdaBoost Regressor	36.78	2400.90	48.24	0.58	0.29	0.26	0.04
Random Forest Regressor	29.58	2493.49	48.99	0.56	0.29	0.20	0.10
Extreme Gradient Ba)sting	30.93	2833.09	52.19	0.52	0.30	0.21	0.21
Lasso Regression	38.30	2967.40	537.92	0.48	0.30	0.24	0.01
Ridge Regression	37.09	2795.83	521.44	0.47	0.30	0.24	0.08
Bayesian Ridge	39.49	3075.62	546.58	0.46	0.31	0.25	0.01
Lasso Least Angle Regression	39.93	3209.94	561.38	0.43	0.32	0.26	0.01
Decision Tree Regressor	31.58	3571.12	572.14	0.42	0.33	0.20	0.01
Elastic Net	43.97	3660.27	597.49	0.34	0.34	0.29	0.01
Linear Regression	41.37	3537.18	578.18	0.29	0.37	0.28	0.01
K Neighbors Regressar	43.58	4315.71	649.02	0.20	0.37	0.31	0.01
Orthogonal Matching Pursuit	60.01	5908.77	757.43	0.01	0.44	0.41	0.01
Huber Regressor	60.40	7068.74	820.82	-0.09	0.51	0.36	0.01
Dummy Regressor	70.61	7049.36	834.95	-0.18	0.48	0.50	0.0070

A lower MSE indicates better prediction performance. The best-performing model in terms of MSE is the "CatBoost Regressor" model(1591.78). A lower RMSE indicates better forecast performance. Among the models in the table, the best-performing model in terms of RMSE is the "CatBoost Regressor" model(39.13). If the R^2 value, which shows how much of the variance of the dependent variable is explained by the independent variables, is close to 1, it means a better fit. Among the models in the table, the best-performing model in terms of R^2 is the "CatBoost Regressor" model (0.71). A lower RMSLE, which represents the square root of the logarithmic error amount, indicates a better prediction performance. Among the models in the table, the best-performing model in terms of RMSLE is the "CatBoost Regressor" model (0.24). A lower MAPE value, which represents the average absolute percentage difference between actual values and predicted values, indicates a better prediction performance. Among the models in the table, the best-performing model in terms of MAPE is the "CatBoost Regressor" model (0.18). A lower training time in the Training Time value, which represents the time it takes to train the model, indicates faster model training. Among the models in the table, the best-performing model in terms of training time is the "CatBoost Regressor" model (31.150 seconds).

The primary performance metric used in the study is the R-squared metric. R-squared is a statistical measure used to evaluate the performance of regression models. The R-squared value indicates how well the dependent variable is explained by the independent variables. This measure ranges from 0 to

1, with values closer to 1 indicating a better fit, while values approaching 0 indicate a weaker fit. R-squared is often expressed by the formula 2;

$$R^2 = 1 - \frac{\sum_{i=1}^n (y_i - \hat{y}_i)^2}{\sum_{i=1}^n (y_i - \bar{y})^2} \quad (2)$$

y_i = Actual Values, \hat{y}_i = Predicted Values, \bar{y} = Mean of the Dependent Variable, $\sum_{i=1}^n$ = Sum , Number of Observations.

In the prediction error plot for the R2 metric, the x-axis represents the actual values and the y-axis represents the predicted values. Each point represents the true value of an observation and the model's prediction for that observation. Ideally the points should be aligned along the 45-degree line. A skewed distribution or irregular patterns in such charts may indicate that the model is making an error on certain data points. The R2 prediction error graph of the CatBoostRegressor model, which has the highest performance, is shown in Figure 11. The R2 performance metric value was found to be 0.71.

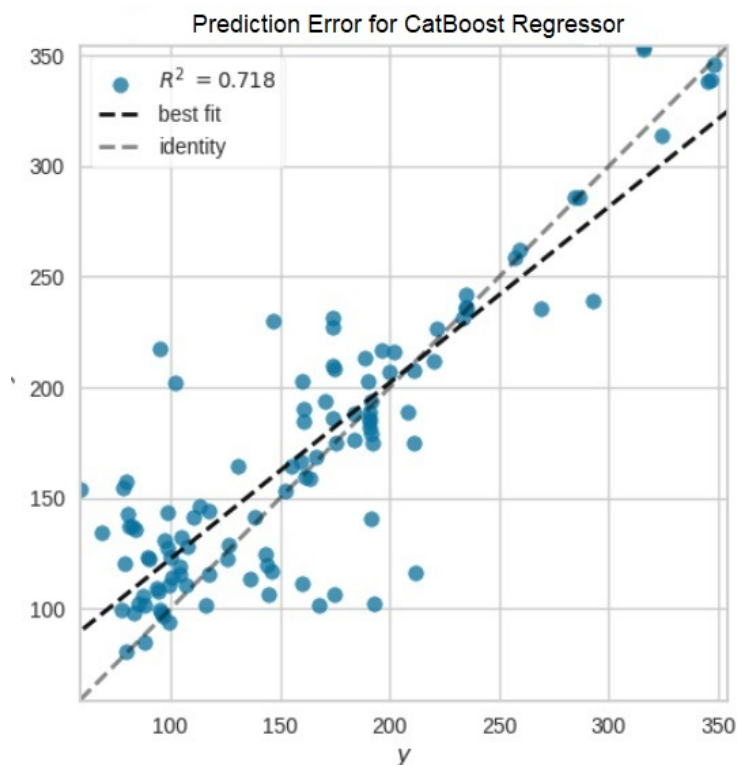


Figure 11: Performance Metrics Based on Regression Models

Below, Table 6 displays five studies from the literature.

Table 6. Five studies from the literature.

Reference	Subject of Study	Classifier	Performance
Geshwaree Huzooree et al. – 2017[41]	Glucose Prediction Data Analytics for Diabetic Patients Monitoring	Autoregressive (ARX)	$R^2 = 0.342$
Guillermo Edinson et all. – 2020 [42]	Application of Artificial Intelligence Techniques for the Estimation of Basal Insulin in Patients with Type I Diabetes	NNs and BNs	NNs $R^2 = 0.067$ BNs $R^2 = 0.634$
Nanayakkara et al. - 2018 [43]	Non-Invasive Blood Glucose Monitoring using a Hybrid Technique	BIS + NIRS	$R^2 = 0.58$

Rui Sun et al. – 2023 [44]	Time in Range Estimation in Patients with Type 2 Diabetes is Improved by Incorporating Fasting and Postprandial Glucose Levels	Linear Regression	$R^2 = 0.36$
Chowdhury Azimul Haque et al. – 2020 [45]	Noninvasive In Vivo Estimation of Blood-Glucose. Concentration by Monte Carlo Simulation	XGBoost	$R^2 = 0.68$
Pappada, S. M. et al. - 2011 [46]	Neural network-based real-time prediction of glucose in patients with insulin-dependent diabetes.	Neural Network	RMSE= 43.9
Aishah, A. F. Q. A. et al. -2011 [47]	Multiple linear regression model analysis in predicting fasting blood glucose level in healthy subjects.	Multiple linear regression	$R^2=0.59$
Our proposed method		CatBoost Regressor	$R^2=0.71$, RMSE= 39.13

Table 6 presents a comparative analysis of several studies on glucose prediction and monitoring in diabetic patients, along with a proposed model. Geshwaree Huzooree et al. (2017) used an autoregressive (ARX) model, achieving an R^2 of 0.342, indicating moderate accuracy. Guillermo Edinson et al. (2020) applied AI techniques, with Neural Networks (NNs) performing poorly ($R^2 = 0.067$) and Bayesian Networks (BNs) performing well ($R^2 = 0.634$). Nanayakkara et al. (2018) utilized a hybrid technique (BIS + NIRS) with an R^2 of 0.58, showing good accuracy. Rui Sun et al. (2023) employed linear regression for time-in-range estimation, yielding an R^2 of 0.36. Chowdhury Azimul Haque et al. (2020) used XGBoost, achieving the highest R^2 of 0.68 among these studies. Pappada et al. (2011) used a neural network with an RMSE of 43.9, and Aishah et al. (2011) used multiple linear regression with an R^2 of 0.59. The proposed model, using a CatBoost Regressor, outperforms all others with an R^2 of 0.71 and an RMSE of 39.13, indicating superior predictive accuracy and lower error.

4. Conclusions

Machine learning is an effective method for predicting blood sugar levels based on PPG signals. PPG is a type of signal obtained from the skin through the absorption or reflection of light, which changes according to the heartbeat. These signals reflect changes in blood circulation and provide information about glucose levels in the blood. Machine learning algorithms can analyze the complexity of PPG signals and predict individuals' blood sugar levels using data from these signals. This method can be considered an alternative to traditional blood sugar measurements because it works noninvasively and can improve individuals' quality of life. However, more research and development are needed to ensure the reliability and accuracy of such systems.

When the success of this study was compared with similar studies, it was seen that the success rate was high. It is possible to increase the success rate by making adjustments such as parameter setting and reducing the noise characteristic during signal measurement. This study used PPG signals to estimate blood sugar levels. Signals were preprocessed to remove noise and artifacts, followed by segmentation based on peaks. The segmented signals were then averaged to prepare for feature extraction. Feature extraction aimed to identify and represent important information from the dataset, incorporating statistical and temporal methods. Specifically, 160 statistical features were extracted and 51 features were selected based on their relevance to the target variable. The pre-processed, segmented, and feature-separated signals were then trained using machine learning models. The system demonstrated success with regression models, achieving an R-squared performance measure of 0.71.

This study focused on explainability and interpretability using explainable artificial intelligence techniques (SHAP) to analyze high-performance models. Feature Importance Plot was used to visualize the contribution of features to the performance of the model. It has been noted that the ranking of features that have the most significant impact on performance varies between machine learning models. The study concluded that analyzing signal properties not only with statistical and temporal attributes, but also with frequency domain attributes can positively affect the results. Additionally, it was stated that increasing the number of samples will significantly affect the feature results. It has been suggested that the small number of extracted features that are highly relevant to the target variable will be important for future Internet of Things (IoT) studies and will enable integration into embedded systems.

Peer-review: Externally peer-reviewed.

Conflict of Interest: This paper has been presented at the INERS'2024 (5th International Engineering Research Symposium) held in Düzce (Turkey), March 7-9, 2024.)

Financial Disclosure: The authors declared that this study has received no financial support.

References

- [1] International Diabetes Federation. (IDF 2009c). Diabetes Prevalence. Online Access <http://www.idf.org/home/index.cfm?node=264> (Access:12.05.2009)
- [2] Diyabet Çığ Gibi Büyüyor. (2008). *Diyabete Bakış*, 7, 6-7.
- [3] K. Wikblad, L. Wibell, , K. Montin (1990). "The Patient's Experience Of Diabetes And Its Treatment: Construction Of An Attitude Scale By A Semantic Differential Technique." *Journal Of Advanced Nursing*, 15(9), 1083-1091.
- [4] American Diabetes Association. Diagnosis and classification of diabetes mellitus, *Diabetes Care*, 32 (1), 62–67, 2009.
- [5] O. Sevli. Diyabet hastalığının farklı sınıflandırıcılar kullanılarak teşhisi, *Journal of the Faculty of Engineering and Architecture of Gazi University*, 38:2 (2023) 989-1001
- [6] American Diabetes Association. (2023). Standards of Medical Care in Diabetes—2023. *Diabetes Care*, 46(Suppl. 1): S1-S291.
- [7] Lam, B. Q., Srivastava, R., Morvant, J., Shankar, S., Srivastava, R. K. 2021. Association of DM and Alcohol Abuse with Cancer: Molecular Mechanisms and Clinical Significance. *Cells* 2021, Vol. 10, 10(11):, 3077. <https://doi.org/10.3390/CELLS10113077>
- [8] Quinones, S., Robert Roberts, C. C., David Cistola, C.-C., Narayan, M., Crites, S. L. 2021. Non-invasive in-vitro glucose monitoring using an optical sensor and machine learning techniques for diabetes applications, Texas.
- [9] Beck, R. W., Riddlesworth, T., Ruedy, K., & Kollman, C. (2018). Continuous glucose monitoring versus usual care in patients with type 2 diabetes receiving multiple daily insulin injections: a randomized trial. *Annals of Internal Medicine*, 169(6), 379-387.
- [10] Karon, B. S. (2016). Why is there still no international standard for glucose in blood? *Clinical Chemistry and Laboratory Medicine (CCLM)*, 54(6), 975-977.
- [11] Newman, J. D., & Turner, A. P. (2005). Home blood glucose biosensors: a commercial perspective. *Biosensors and Bioelectronics*, 20(12), 2435-2453.

- [12] Sieg, A., Guy, R. H., & Delgado-Charro, M. B. (2012). Non-invasive and minimally invasive methods for measuring glucose. In *Advances in Noninvasive Electrocardiographic Monitoring Techniques* (pp. 259-277). Springer, Berlin, Heidelberg.
- [13] Lee, Y. H., Wong, D. T., & Saliva: An emerging biofluid for early detection of diseases. (2009). *American Journal of Dentistry*, 22(4), 241-248.
- [14] Rohleder, D., von Ribbeck, H. G., Brenner, T., Giessen, H., & Lemmer, U. (2012). Noninvasive continuous glucose monitoring by photoacoustic spectroscopy. *Analytical Chemistry*, 84(16), 6558-6565.
- [15] Lukaski, H. C. (1987). Methods for the assessment of human body composition: traditional and new. *American Journal of Clinical Nutrition*, 46(4), 537-556.
- [16] Gusev, M., Poposka, L., Spasevski, G., Kostoska, M., Koteska, B., Simjanoska, M., Ackovska, N., Stojmiski, A., Tasic, J., Trontelj, J. 2020. Noninvasive Glucose Measurement Using Machine Learning and Neural Network Methods and Correlation with Heart Rate Variability. *Journal of Sensors*. <https://doi.org/10.1155/2020/9628281>
- [16] Kossowski, T., Stasinski, R. 2016. Robust IR attenuation measurement for non-invasive glucose level analysis. *International Conference on Systems, Signals, and Image 75 Processing : International Conference on Systems, Signals, and Image Processing (Vol. 2016-June)*. <https://doi.org/10.1109/IWSSIP.2016.7502770>
- [17] Sharma, N. K., Singh, S. 2012. Designing a non invasive blood glucose measurement sensor. 2012 IEEE 7th International Conference on Industrial and Information Systems, ICIIIS 2012 : 2012 IEEE 7th International Conference on Industrial and Information Systems, ICIIIS 2012. <https://doi.org/10.1109/ICIIIS.2012.6304818>
- [18] Zhao, X., Zheng, Q., Yang, Z. M. 2016. Two types of photonic crystals applied to glucose sensor. . <https://doi.org/10.1109/inec.2016.7589369>
- [19] Tanaka, Y., Purtil, C., Tajima, T., Seyama, M., Koizumi, H. 2017. Sensitivity improvement on CW dual-wavelength photoacoustic spectroscopy using acoustic resonant mode for 79 noninvasive glucose monitor. *Proceedings of IEEE Sensors : Proceedings of IEEE Sensors*. <https://doi.org/10.1109/ICSENS.2016.7808685>
- [20] Arikan , K., Burhan, H., Sahin , E., Sen, F., A sensitive, fast, selective, and reusable enzyme-free glucose sensor based on monodisperse AuNi alloy nanoparticles on activated carbon support, *Chemosphere*, 291, 3 2022 , <https://doi.org/10.1016/j.chemosphere.2021.132718>
- [21] Karimi, F., Zare, N., Bekmezci, M., Akin, M., Bayat, R., Seyitoğlu, B., Arikan, K., Isik, I., Sen, F., Enzyme-free glucose detection via scalable and economical fabrication of nickel-polyvinylpyrrolidone-modified multi-walled carbon nanotubes, *Elektrochimica Acta* , 496 , 8 2024 <https://doi.org/10.1016/j.electacta.2024.144341>
- [22] Allen, J. (2007). Photoplethysmography and its application in clinical physiological measurement. *Physiological Measurement*, 28(3), R1-R39
- [23] C. Salamea, E. Narvaez and M. Montalvo, “Database Proposal for Correlation of Glucose and Photoplethysmography Signals”, *Advances in Intelligent Systems and Computing*, pp. 44-53, 2019. , Available: 10.1007/978-3-030-32033-1_5.
- [24] Online: “Utilizing the PPG/BVP signal”, support.empatica.com, 2021, Available: <https://support.empatica.com/hc/en-us/articles/204954639-Utilizing-the-PPGBVP-signal>
- [25] D. Makowski, T. Pham, ZJ. Lau, JC. Brammer JC, F. Lespinasse, H . Pham, C. Scholzel, SHA. Chen. NeuroKit2 A Python toolbox for neurophysiological signal processing. *Behavior* 2021

- [26] M. Elgendi, 2012. On the Analysis of Fingertip Photoplethysmogram Signals, *Current Cardiology Reviews*, 8, 14-25, Available: [10.2174/157340312801215782](https://doi.org/10.2174/157340312801215782)
- [27] M. Barandas, D. Folgado, L. Fernandes, S. Santos, M. Abreu, P. Bota, H. Liu, T. Schultz, H. Gamboa. TSFEL: Time Series Feature Extraction Library, *SoftwareX* 11 (2020). <https://doi.org/10.1016/j.softx.2020.100456>.
- [28] Fraunhofer Portugal AICOS. (n.d.). TSFEL: Time Series Feature Extraction Library. GitHub Repository. Retrieved from <https://github.com/fraunhoferportugal/tsfel>
- [29] DeCarlo, L. T. (1997). On the meaning and use of kurtosis and skewness. *Psychological Methods*, 2(3), 292-307.
- [30] R. M. Kimmel, S. I. Rubin. (1997). *Crest Factor*. CRC Press.
- [31] Ali, M. (2020). PyCaret: An open-source, low-code machine learning library in Python. Available at: <https://pycaret.org>.
- [32] T. Nguyen, N. Tran, B. M. Nguyen, G. Nguyen, 2018. A resource usage prediction system using functional-link and genetic algorithm neural network for multivariate cloud metrics. In 2018 IEEE 11th conference on service-oriented computing and applications (SOCA), 49–56. IEEE,
- [33] James, G., Witten, D., Hastie, T., & Tibshirani, R. (2013). *An Introduction to Statistical Learning: with Applications in R*. Springer Science & Business Media.
- [34] Root Mean Square Value A Dictionary of Physics (6 ed.). Oxford University Press. 2009. ISBN 9780199233991
- [35] Kutner, M. H., Nachtsheim, C. J., Neter, J., & Li, W. (2004). *Applied Linear Statistical Models*. McGraw-Hill/Irwin.
- [36] Chen, T., & Guestrin, C. (2016). XGBoost: A Scalable Tree Boosting System. *Proceedings of the 22nd ACM SIGKDD International Conference on Knowledge Discovery and Data Mining*, 785–794.
- [37] Hyndman, R. J., & Koehler, A. B. (2006). Another look at measures of forecast accuracy. *International Journal of Forecasting*, 22(4), 679-688.
- [38] Anna Veronika Dorogush, Andrey Gulin, Gleb Gusev, Nikita Kazeev, Liudmila Ostroumova Prokhorenkova, Aleksandr Vorobev "Fighting biases with dynamic boosting". arXiv:1706.09516, 2017.
- [39] Qi Meng, Guolin Ke, Taifeng Wang, Wei Chen, Qiwei Ye, Zhi-Ming Ma, Tie-Yan Liu. "A Communication-Efficient Parallel Algorithm for Decision Tree". *Advances in Neural Information Processing Systems* 29 (NIPS 2016), pp. 1279-1287.
- [40] Moore, D. S., McCabe, G. P., & Craig, B. A. (2019). *Introduction to the Practice of Statistics*. W. H. Freeman.
- [41] G. H Huzooree, K.K. Khedo, N. Joons, 2017. Glucose prediction data analytics for diabetic patients monitoring, 2017 1st International Conference on Next Generation Computing Applications (NextComp) 10.1109/NEXTCOMP.2017.8016197
- [42] G. Edinson, G. Go´mez , L. E. B. Agredo, V. Marti´nez, O. F. B. Leiva. Application of Artificial Intelligence Techniques for the Estimation of Basal Insulin in Patients with Type I Diabetes, *Research Article Open Access* <https://doi.org/10.1155/2020/7326073>
- [43] N.D Nanayakkara, S.C Munasingha, G.P. Ruwanpathirana, 2018. Non-Invasive Blood Glucose Monitoring using a Hybrid Technique, In *Proceedings of the 2018 Moratuwa Engineering Research Conference (MERCon)*, Moratuwa, Sri Lanka, pp. 7–12. , 10.1109/MERCon.2018.8421885

[44] R. Sun, Y.L. Duan, Y.M. Zhang, L.G. Feng, B. Ding, R.N. Yan, J.H. Ma, X.F. Su. Time in Range Estimation in Patients with Type 2 Diabetes is Improved by Incorporating Fasting and Postprandial Glucose Levels, *DIABETES THERAPY*, Volume14Issue8Page1373-1386, DOI10.1007/s13300-023-01432-2

[45] S. S. Gupta, S. Hossain, C. A. Haque and K. -D. Kim, 2020. In-Vivo Estimation of Glucose Level Using PPG Signal, 2020 International Conference on Information and Communication Technology Convergence (ICTC), Jeju, Korea (South), 2020, pp. 733-736, doi: 10.1109/ICTC49870.2020.9289629

[46] Pappada, S. M., Cameron, B. D., Rosman, P. M., Bourey, R. E., Papadimos, T. J., Olorunto, W., & Borst, M. J. (2011). Neural network-based real-time prediction of glucose in patients with insulin-dependent diabetes. *Diabetes technology & therapeutics*, 13(2), 135-141.

[47] Aishah, A. F. Q. A., Zainuriah, M. R., & Norhilda, A. K. (2019). Multiple linear regression model analysis in predicting fasting blood glucose level in healthy subjects. In *IOP Conference Series: Materials Science and Engineering* (Vol. 469, No. 1, p. 012050). IOP Publishing.

Sonochemical Removal of Highly Toxic Aqueous Cd²⁺ and Cr⁶⁺ Ions Using Dandelion-like Co₃O₄ Nanoflowers

¹Elif Aybike Berberoğlu , ^{2,3}Mümin Mehmet Koç , ¹Nurdan Kurnaz Yetim , *¹Cemile Özcan 

¹ Kırklareli University, Department of Chemistry, Faculty of Literature and Sciences, Kırklareli, Türkiye.

² Kırklareli University, Department of Medical Service and Techniques, School of Medical Service, Kırklareli, Türkiye.

³ Kırklareli University, Department of Physics, Faculty of Literature and Sciences, Kırklareli, Türkiye.

* Corresponding author, e-mail: cemilebal.ozcan@klu.edu.tr

Submission Date: 20.10.2022

Acceptation Date: 05.01.2023

Abstract –In this work, cobalt(II/III) oxide (Co₃O₄) nano/microflowers were practically synthesized in laboratory conditions. Adsorbance properties of the nanoflowers were investigated for the removal of cadmium and chromium heavy metal ions. To assess the chemical and morphological characteristics of Co₃O₄ nanoflowers, Fourier transform infrared spectroscopy (FTIR), X-ray diffractometry (XRD), field emission electron microscopy (FESEM), Energy dispersive spectroscopy (EDS), and was used. To determine the adsorbance mechanism in detail, eluent concentration, eluent type, solution pH, adsorbent amount, solution volume, and adsorption duration were studied. In these assessments, flame atomic absorption spectroscopy (FAAS) was used. For Cr⁶⁺, adsorption optimum parameters were determined as 3M HNO₃, pH 6.5, 150mg, 30mL, 60min. For Cd²⁺, optimum parameters were determined as 3M HNO₃, pH 6.0, 100mg, 10mL, 30min. Co₃O₄, nanoflowers are eco-friendly adsorbent materials for the adsorption of Cd⁶⁺ and Cd²⁺ heavy metal ions since the production method is affordable and practical.

Keywords: Co₃O₄ Nanoflowers; Solid phase extraction; FAAS; Cr⁶⁺; Cd²⁺

Yüksek Toksikiteye Sahip Cd²⁺ and Cr⁶⁺ İyonlarının Karahindiba Şeklindeki Co₃O₄ Nanoçiçek Yapılar Kullanılarak Sonokimyasal Yöntemle Sudan Ayrıştırılması

Öz - Bu çalışmada, hidrotermal yöntem ile kobalt(II/III) oksit (Co₃O₄) nano/mikroçiçek yapılar laboratuvar şartlarında pratik bir şekilde sentezlendi. Krom ve kadmiyum gibi ağır metal iyonlarının uzaklaştırılması için bu nanoflowerların adsorban olarak uygulanması araştırıldı. Co₃O₄ nanoçiçeklerinin, morfolojik analizi ve kimyasal bileşimini karakterize etmek için X ışını kırınım analizi (XRD), alan emisyonlu taramalı elektron mikroskopisi (FESEM), enerji dağılım X-ışınları spektroskopisi (EDS) ve FTIR teknikleri kullanılarak gerçekleştirildi. Adsorpsiyon sisteminin optimum koşullarını belirlemek amacı ile elüent derişimi ve türü, çözeltinin pH'ı, adsorban miktarı, çözelti hacmi ve adsorpsiyon süresi gibi parametrelerin etkisi incelendi. Elde edilen çözeltide metal iyonlarının alevli atomik adsorpsiyon spektrometrisi (FAAS) analiz sonuçları doğrultusunda optimumum parametreler belirlendi. Bu parametre sonuçları sırasıyla Co₃O₄ nanofloweri ile Cr⁶⁺ için 3 M HNO₃, pH 6.5, 150 mg, 30 mL, 60 dk; Cd²⁺ için 3 M HNO₃, pH 6.0, 100 mg, 10 mL, 30 dk olarak bulundu. Co₃O₄ nanoçiçekleri; adsorpsiyon kapasitelerinin yüksek olması, kolayca sentezlenebilir ve imalat maliyetlerinin nispeten düşük olmasından dolayı krom, kadmiyum ve diğer ağır metal iyonlarının sulu sistemlerden uzaklaştırılmasında verimli ve çevre dostu adsorbanlar olabileceğini göstermektedirler.

Anahtar kelimeler: Co₃O₄ Nanoçiçekler; Katı faz ekstrasyonu; FAAS; Cr⁶⁺; Cd²⁺

¹ Corresponding author: Tel: +90 028 824 6173 - Extension: 1150
E-mail: cemilebal.ozcan@klu.edu.tr

1. Introduction

Heavy metals were detected different water sources around the world, and they can be used in different industrial products including dyes, pharmaceuticals, personal hygiene products, etc [1, 2]. Contamination of fresh waters and aquatic systems by heavy metals is becoming an emerging problem for the world. Such contaminated waters could include different heavy metal ions such as Hg(II), Pb(II), Cr(VI), Cd(II), and Ni [2]. Such heavy metal ions were found to be toxic and can be dangerous to marine life and aquatic animals [3–5]. Different research illustrates that, several unit operations such as adsorption, membrane filtration, chemical precipitation, coagulation - flocculation and floatation, ion exchange, or liquid-liquid extraction can be utilized to separate heavy metals from the samples [5–8]. Among those, adsorption is a common method where a low cost, selective, reusable and simple application was promised [5–8].

Recently, various materials like activated carbon, activated alumina, clay, zeolite, etc. were used for the removal of heavy metal ions [5–8]. However, such materials have limited adsorption capacity and some of them are not reusable. On contrary, metal oxide nanostructures have outstanding adsorption capacity due to their high surface/volume ratio and well-defined surface morphology [9]. Therefore, they found to be promising materials as next generation adsorbent materials.

Nanostructures are becoming attractive materials for the people from different areas since they can be applied to semiconductors and different technological applications due to their interesting chemical and physical properties with outstanding morphology [10]. Recently, three dimensional (3D) nanostructures with well-defined morphologies increases their popularity [11, 12]. Among those, nanoflowers in fiber, tube and flake forms are becoming popular due to their unique structural characteristics [11]. Co₃O₄ nanoflowers are a special kind of nanoflowers with magnetic characteristics which can be used in magnetic applications, gas sensor applications, catalysis applications, etc. [13] Different groups around the world tries to produce Co₃O₄ nanostructures in 3D; some of them managed to produce nanospheres, nanocubes, nanorodes using physical and chemical methods [10]. For this purpose, different production methods like solvothermal synthesis, chemical spray pyrolysis, chemical vapor deposition, sol-gel hydrothermal synthesis, simple precipitation, etc. were reported [14–18]. Hydrothermal synthesis could be used in the production of inorganic or organic/inorganic (hybrid) nanomaterials and/or nanocomposites. While other methods are having different drawbacks like high calcination temperature, toxic reactants, long reaction durations, multiple reaction steps and low production efficiency, hydrothermal synthesis provide affordable and reliable experimental media. Hydrothermal method is a highly efficient production process with minimum production cost which enables researchers to control nanostructure morphology. The method also provide good nanostructure size and shape control [19].

In this work, heavy metal adsorption potential of Co₃O₄ nanoflowers, which were previously reported by our group [20], were investigated for the recovery of chromium and cadmium in sea water (SRM) sample. Co₃O₄ nanoflowers used in the investigation were produced using hydrothermal synthesis method. Structural characterization of the nanoparticles was performed using various characterization techniques such as FESEM, XRD, FTIR and EDS. Then, Cr⁶⁺ and Cd²⁺ heavy metal ion recovery potential of the nanoflowers were assessed. Adsorption processes were optimized where influence of different parameters like eluent type, eluent concentration, pH, adsorbent amount, solution volume adsorption duration, etc. on adsorption characteristics were studied. Analytical recovery activity was also assessed regarding the analysis result of metal ions obtained from flame atomic absorption spectroscopy (FAAS) (See Figure 1).

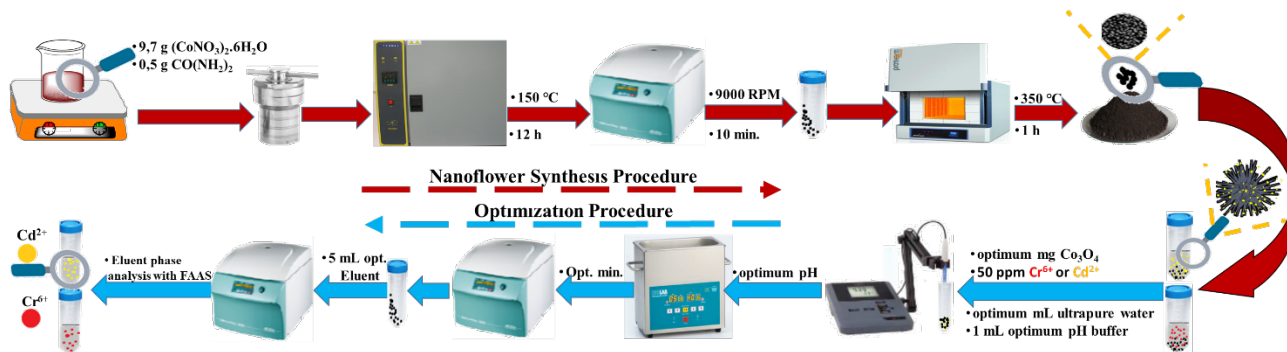


Figure 1. Schematics illustrate the production and investigation process followed in this work.

2. Materials & Methods

2.1. Spectroscopic and crystallographic investigation.

X-ray diffraction investigations were employed using RIKAGU diffractometer. Scanning was conducted between 10 and 90 degrees. Scanning electron microscope used in the structural investigation is FEI Quanta 400F supported with EDS (energy dispersive X-ray spectroscopy). Brunauer–Emmett–Teller (BET) investigation was performed using Quantachrome Nova 4000E. The infrared spectrum was recorded by a JASCO FTIR-6700 spectrometer between wavelengths of 400 and 4000 cm^{-1} . The FAAS investigation was performed using Agilent 240 AA Duo AAS. Cr^{6+} and Cd^{2+} heavy metal ions were assessed using Agilent hollow cathode lamps. Parameters used for the determination of metals are presented in Table 1.

Table 1. Parameters used in the FAAS analysis for the determination of metals

	Cr^{6+}	Cd^{2+}
Air Flow; mL/min	-	13.5
Slit Width (nm)	0.2	0.5
Lamp Current (mA)	7.0	4.0
Acetylene Flow	6.80	2.00
Used Flame	$\text{N}_2\text{O}/\text{Acetylene}$	$\text{Air}/\text{Acetylene}$
Wavelength (nm)	357.9	326.1
N_2O flow; mL/min	10.00	-

All chemicals utilized during the experimental process were analytical level (Merck quality). Ultra-pure water (ELGA, 18.2 $\text{M}\Omega$ cm) is used in the whole experimental process.

For standard metal solution, 1000 mg/L stock solutions (NIST standard) were used. 3; 2; 1; 0.5; 0.25; 0.1; and 0.05 mg/L solutions were prepared from standards of Cr^{6+} and Cd^{2+} which were prepared by dissolving 0.2 M HNO_3 . They were scanned by FAAS.

2.2. Production of Co_3O_4 nanoflowers

Co_3O_4 nanoflowers were synthesized using hydrothermal method in the lab regarding our previous recipe which was reported in our previous papers [20]. In the synthesis process 9.7 gr of cobalt nitride hexahydrate ($\text{Co}(\text{NO}_3)_2 \cdot 6\text{H}_2\text{O}$) and 0.5 gr of urea $\text{CO}(\text{NH}_2)_2$ were stirred in 35 mL of deionized pure water for 1h. Solution was placed into the Teflon autoclave. The autoclave was placed in oven for 12 h at 150 °C. 12 h later autoclave was taken and left for cool. The solution was then centrifuged and several times to collect the precipitate in the solution. Precipitate was washed a couple of times using ethanol and deionized water. The precipitate was transferred to the oven set at 80°C and kept there for 24 hours. Precipitate was then transferred to the ash furnace at 150°C; the temperature of the furnace was increased step by step where 2°C/1 min step increase rate was employed. When the

temperature reach 300 °C, precipitate was kept there for 1 h whereas the calcinated Co₃O₄ nanoflower powder was obtained [20, 21].

2.3. Solid phase extraction methodology

50 mL of falcon tubes were used for the optimization of eluent type, eluent concentration, pH, sample amount, eluent volume and application time where optimum conditions for the removal of Cr⁶⁺ and Cd²⁺ metal ions were determined.

Standard experimental procedure is as follows:

50 mg of nanoflower was placed in 50 mL falcon tube where 10 mL deionized water containing 0.25 mL (50 ppm) heavy metal ion and 1 mL of buffer solution (pH: 6.0) was added. Solution pH was set to pH: 6.0 by adding 0.01M NaOH and 0.01 M HCl. The solution was topped up with ultra-pure water and set to 25 mL. After 10 mins of sonication, the solution was centrifuged at 9000 rpm for 10 mins. Liquid phase was kept for analysis; 5 mL of acid solution was added to the solid phase. Samples were sonicated for 10 mins and centrifuged at 9000 rpm for 10 mins. The second liquid phase was also kept. Each step was repeated for Cr⁶⁺ and Cd²⁺ heavy metal ion concentration.

For the eluent optimization steps of 0.1-1-2-3 M HNO₃ and 1M of HCl were studied. For pH optimization, pH values of 5, 5.5, 6, 6.5, 7, 7.5 and 8 were studied. For adsorbent amount, 50 mg, 100 mg, 150 mg and 200 mg of Co₃O₄ nanoflower amounts were studied. For the fluent volume study, activity in 5 mL, 10 mL, 20 mL and 30 mL pure water was assessed. For the optimization of sonication duration, 5 mins, 10 mins, 30 mins and 60 mins were studied.

2.3.1 Analysis of real samples: NRC-CNRC certified sea water was assessed for the validation of SRM (standard reference material) where standard addition method was used in the assessment. Before the analysis, 0.5 g of solid sample was taken and 5 mL of HNO₃:H₂O₂ (2:1, h/h) were added on them. Wet samples were placed in shaker water bath and kept at 50°C until the samples get dry. For liquid phase samples, samples were centrifuged at 9000 rpm for 20 mins liquid phase was evaporated until samples totally dry. 4.5 mL standard sea water and 0.5 mL HNO₃ solutions were dried at shaker water bath at 50°C.

Table 2. The chemical properties of synthetic natural water.

Concentration	
pH	8.0
Zn	0.200 ± 0.003
Na	9.00 ± 0.01
Ca	40.9 ± 0.3
Mn	0.200 ± 0.001
K	7.50 ± 0.02
Fe	0.200 ± 0.001
Cu	0.050 ± 0.002

2.3.2 Validation of Method-Analytical Performance: RSD (relative standard deviation), LOD (limit of detection), calibration equation, LOQ (the limit of quantification) and linear regression were defined. Determined values were illustrated in Table 3. The LOD and LOQ were calculated as three times the standard deviation (S.D.) (3σ) and (10σ) of the blank signal. The applied method had been confirmed by NRC-CNRC SRM (NASS-6) (Table 5). The method was also employed to the real seawater (see the Table 6). Moreover, the EF (enrichment factor) was assessed by the formula below [22–25] :

$$EF = \frac{Q_T}{Q_M} \cdot \frac{Q_T^0}{Q_M^0} \quad (1)$$

Table 3. Optimum conditions for Cr⁶⁺ and Cd²⁺

	Cr ⁶⁺	Cd ²⁺
Eluent type,	3 M HNO ₃	3 M HNO ₃
Correlation coefficients (R ²)	0.9985	0.9991
Linear regression (y=ax+b)	0.0229x – 0.0006	0.0187x – 0.002
LOD, µg/L	0.6	1.8
LOQ, µg/L	2	6
RSD%	0.2-9.7	0.7-9.2
Amount of nanoflower, mg	150	100
Sonication time, min	60	30
Enrichment factor, fold	6	2
Sample volume, mL	30	10
pH	6.5	6.0

3. Results and Discussions

3.1. Characterization of Co₃O₄ nanoflowers

Co₃O₄ nanoflowers were produced using hydrothermal synthesis, nanoparticles were then analyzed using FTIR, XRD, FESEM, and EDS methods. Figure 2 illustrates FTIR spectrum of Co₃O₄ nanoflowers between 400 and 4000 cm⁻¹. Straight line illustrating the band between 665 and 575 cm⁻¹ illustrate ν(Co-O) tension graph occurs due to Co₃O₄ structure. The large band observed 3400 cm⁻¹ belongs to O-H tension vibration of hydroxyl groups originated from adsorbed water molecules [20].

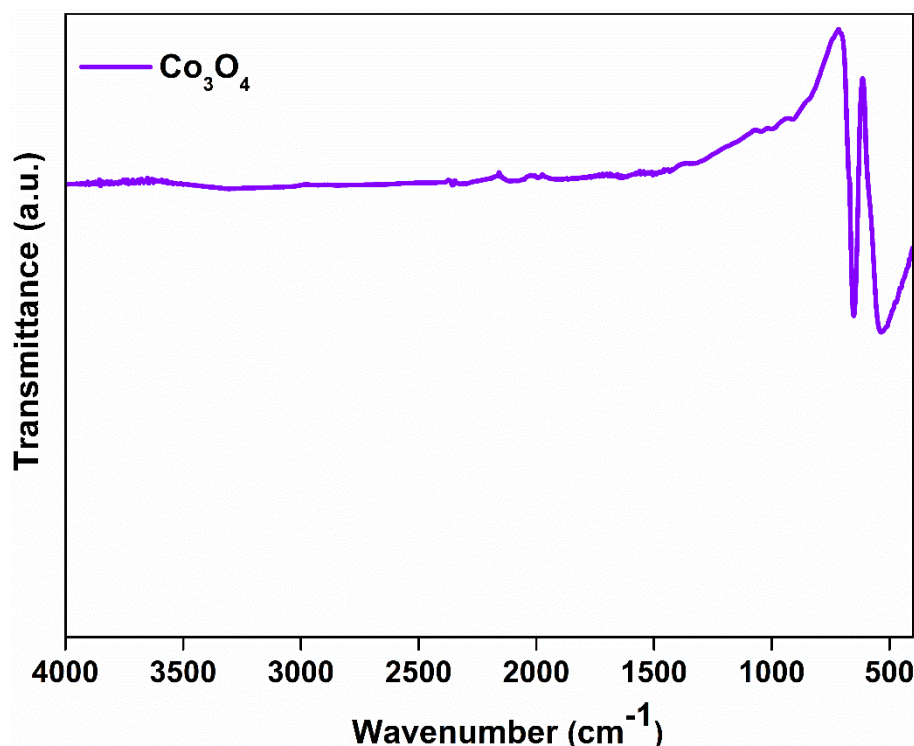


Figure 2. FTIR spectrum of Co₃O₄ nanoflowers.

XRD patterns of Co₃O₄ nanoflowers were presented in Figure 3 where diffraction pattern was plotted in purple color. It was seen that there are various peaks which indicate different types of crystal formations. Peaks at 19,0°, 31,3°, 36,8°, 38,5°, 44,8°, 55,6°, 59,4°, 65,2°, 77,3° degrees were observed; such peaks are corresponding to face centered cubic crystal structures in (111), (220), (311), (222), (400), (422), (511), (440) orientation. Sharp peaks observed in crystal diffraction pattern correspond to face centered cubic crystal formation [20]. It illustrates that the production method can

produce pure crystals in stable crystal type. Therefore, no different types of crystal formation were observed.

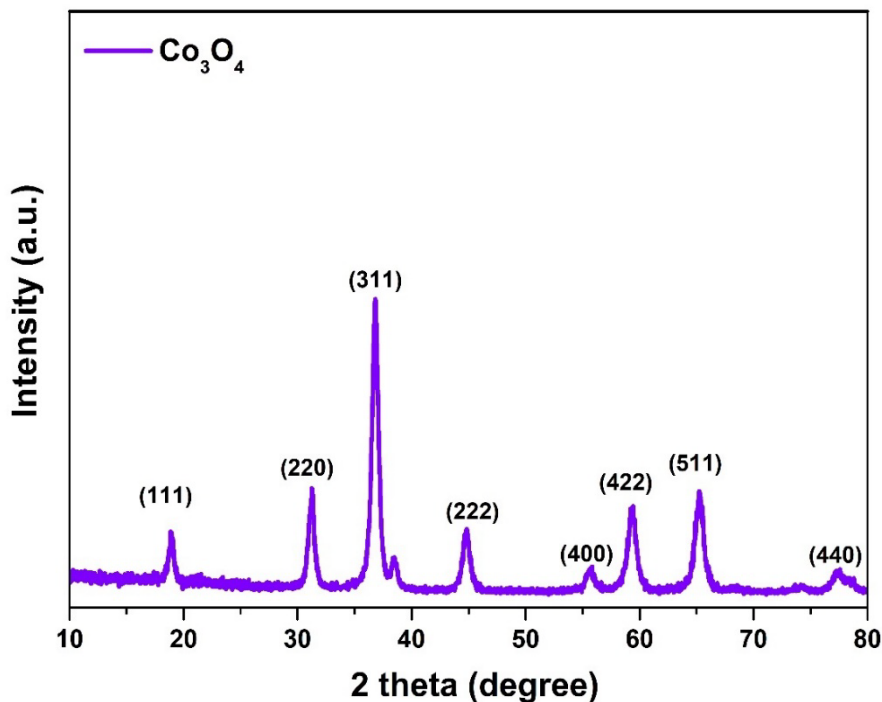


Figure 3. XRD diffraction pattern of Co_3O_4 nanoflowers

FESEM images of nanoflowers were illustrated in Figure 4. In Figure 4, different images were presented. The image on the left illustrates a larger scaled version where different nanoflowers can be seen all of which are in flower form. In the image in the right zoomed version was presented. Co_3O_4 nanoflowers contain fiber like structures that come together and form a dandelion like structure. Nanofibers in the nanoflowers are pointing out such a case enhances the surface area/surface volume rate and porosity. Such a case enables us to obtain enhanced adsorption capacity with outstanding electronic and catalytic activity.

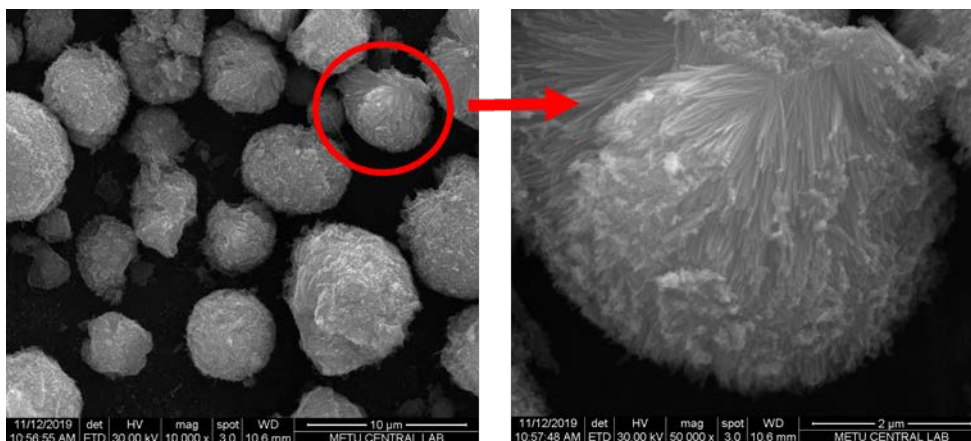


Figure 4. FESEM images of Co_3O_4 nanoflowers.

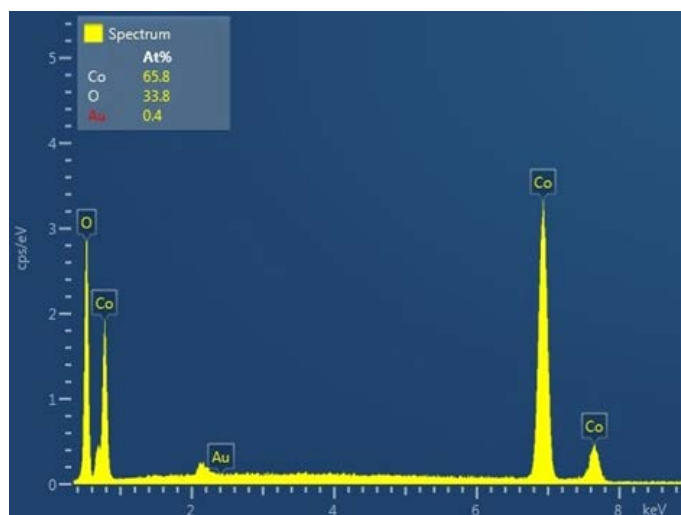


Figure 5. EDS spectra of Co_3O_4 nanoflowers [20].

EDS spectra were presented in Figure 5. Elemental analysis was performed using EDS apparatus of FESEM. Apparent Co and O related peaks could be addressed in the spectra. EDS spectrum confirmed that nanoflowers consisted of Co and O atoms where no residual distortion peaks were seen in the spectra.

Surface area of the nanoflowers were investigated using BET analysis. The surface area of the nanoflowers was measured as $50.73 \text{ m}^2\text{g}^{-1}$. The average pore volume was found to be 168.9913 \AA and the average pore width was determined as 165.819 \AA . Measured surface area was found to be consistent with the results reported for Co_3O_4 nanoflowers in the literature [26, 27]. N_2 adsorption – desorption BET isotherms were presented in Figure 6.

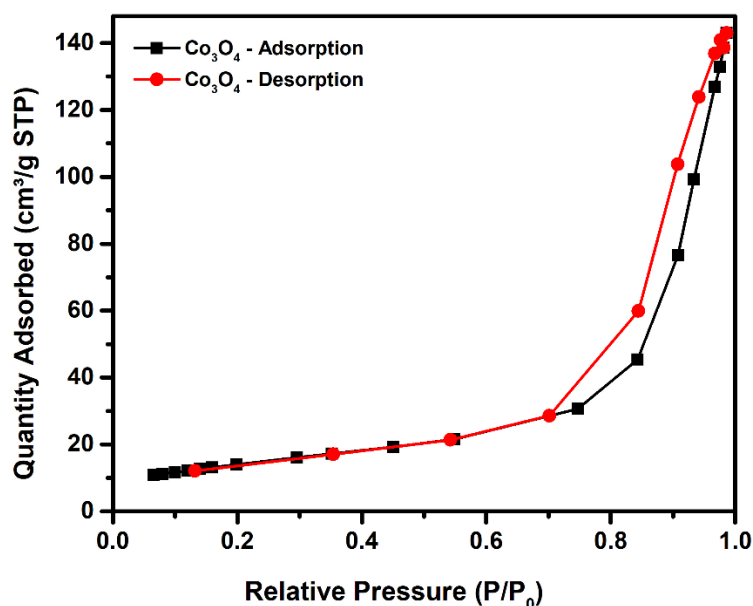


Figure 6. N_2 adsorption – desorption BET isotherm plots of Co_3O_4 nanoflowers.

3.2. Removal of heavy metal ions (Cr^{6+} , Cd^{2+})

3.2.1 Effect of eluent type: To promote the influence between Co_3O_4 nanoflowers and Cr^{6+} , Cd^{2+} heavy metal ions in aqueous media, sonication was employed to the solution. Samples were sonicated at room temperature for 10 mins. After the sonication, centrifugation process was held at 9000 rpm for 10 mins. To assess the Cr^{6+} , Cd^{2+} content, AAS investigation was employed to the filtered supernatants. Eluent type influence for the Co_3O_4 nanoflowers based recovery of Cr^{6+} , Cd^{2+} metal ions were investigated for 1 M HCl and 0.1 M HNO_3 , 1 M HNO_3 , 2 M HNO_3 , and 3 M HNO_3 . Results

were illustrated in Figure 7. Co_3O_4 nanoflowers successfully recovered the 99.7% and 92.8% for 3 M HNO_3 for Cr^{6+} and Cd^{2+} respectively.

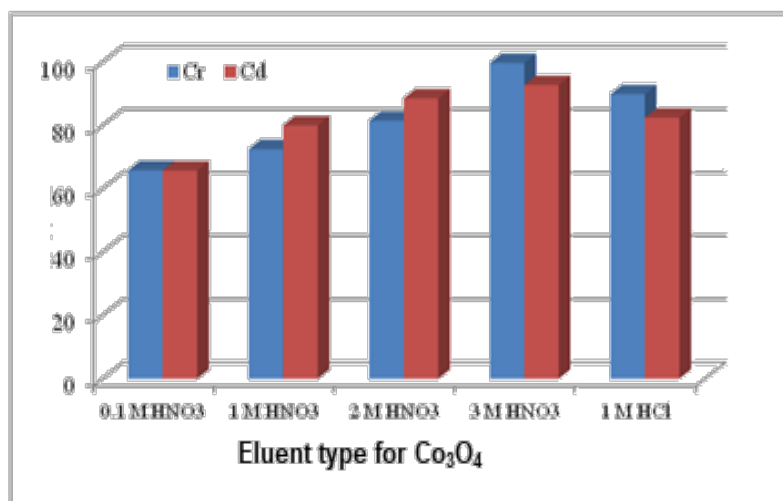


Figure 7. The effect of eluent on Cr^{6+} , Cd^{2+} ion removal.

3.2.2. Effect of pH: pH value has a significant effect on metal ion solubility. Therefore, pH is an important parameter affecting the recovery rate of heavy metals. Thus, pH is an essential parameter that addressed in the recovery studies. Hence, effect of pH on Cr^{6+} , Cd^{2+} heavy metal ion removal in the existence of Co_3O_4 nanoflowers was investigated. pH related Cr^{6+} , Cd^{2+} metal removal rate was illustrated in Figure 8. By scanning between pH 5.5 and 8.0, the pH value with maximum recovery was determined as 6.5 and 6.0 optimum for Cr^{6+} and Cd^{2+} , respectively. Removal percentage starts to decrease by pH 6.0 and 6.5 for Cr^{6+} and Cd^{2+} , respectively. Maximum removal rate for Cr^{6+} and Cd^{2+} were obtained as 97.8% and 93.6%, respectively. We concluded that Cr^{6+} and Cd^{2+} metal ions prefer a soft acidic condition for optimum recovery process.

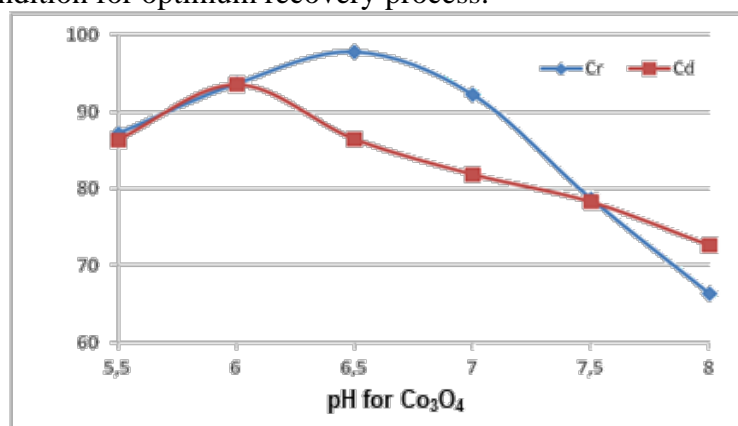


Figure 8. The effect pH for the removal of Cr^{6+} , Cd^{2+} ions

3.2.3. Effect of adsorbent amount: Optimization of Co_3O_4 nanoflower adsorbent amount is a critical parameter for not to overuse the adsorbents. The graph presented below shows recovery percentage of Cr^{6+} and Cd^{2+} ions. Heavy metal ions removal rate depending on nanoflower concentration was illustrated in Figure 9. The best recovery rates for Cr^{6+} and Cd^{2+} were achieved as 99.0% and 96.3% with 150 mg Co_3O_4 and 100 mg Co_3O_4 , respectively.

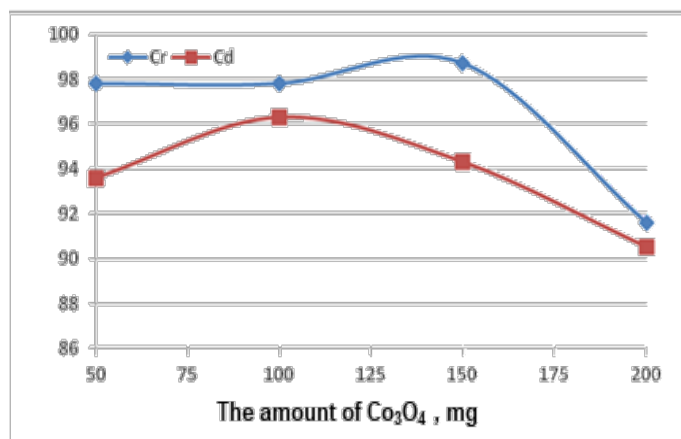


Figure 9. The effect of nanoflower dosage on Cr^{6+} , Cd^{2+} heavy metal ion recovery.

3.2.4. Effect of solvent volume: The plot in Figure 10 illustrates the solvent volume effect on removal rate of Cr^{6+} and Cd^{2+} in the presence of Co_3O_4 . To investigate the influence of solvent volume on removal rates, different volumes 5 mL, 10 mL, 20 mL and 30 mL were studied. The max removal rate for Cr^{6+} and Cd^{2+} were found to be 99.0% and 97.8% with 30 mL and 10 mL, respectively.

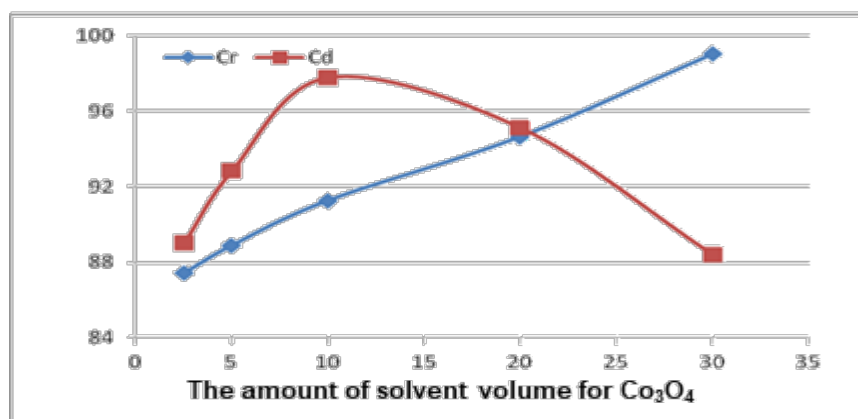


Figure 10. The effect of solvent amount for the removal of Cr^{6+} , Cd^{2+} ions

3.2.5. Influence of sonication duration: To speed up the nanoflower adsorption of metal ions, sonic vibration was applied to samples. To assess the sonication effect on the removal rate of Cr^{6+} and Cd^{2+} , various sonication time periods were studied like 5 mins, 10 mins, 15 mins, 20 mins, 30 mins, and 60 mins. Plots showing the effect of sonication duration on removal rate of Cr^{6+} and Cd^{2+} were illustrated in Figure 11. The graph shows that the optimum removal duration was obtained at 30 mins. The recovery percentage increased gradually till 30 mins of sonication, after that recovery percentage starts to diminish. Removal percentages at 30 mins of sonication is 98.6% and 98.7% for Cr^{6+} and Cd^{2+} , respectively.

3.2.6 Repeatability: In the extraction time optimization, the last remaining solid phase was washed several times using pure water. The optimum conditions were repeated 6 times and the residue was analyzed using FAAS. Results were presented in Table 4. The table clearly illustrates that matrix ions affect the recovery of heavy metal ions. All in all, recovery rates were found to be quite high. Therefore, the presented procedure is able to recover heavy metal ions from the aqueous media and could be used in enrichment applications.

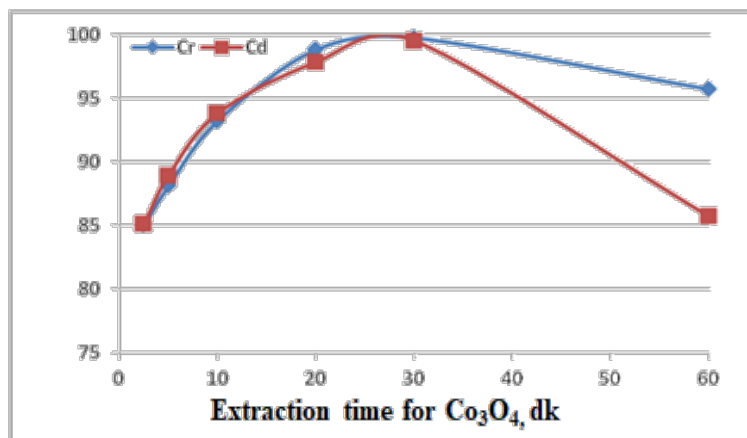


Figure 11. The effect of sonication time for the removal of Cr⁶⁺, Cd²⁺ ions.

Table 4. Influences of matrix ions on the recoveries of Cr⁶⁺ and Cd²⁺ (N = 3)

Ions	Added as	Concentration (mg/L)	Cr ⁶⁺	Cd ²⁺
Na ⁺	NaCl	500	97 ± 2	97 ± 3
K ⁺	KCl	150	95 ± 3	95 ± 3
Ca ²⁺	CaCl ₂	150	96 ± 2	96 ± 2
Mg ²⁺	MgCl ₂	100	97 ± 3	99 ± 1
Na ⁺	NaCl	500	97 ± 2	97 ± 3
Cu ²⁺	Cu(NO ₃) ₂	5	97 ± 3	97 ± 3
Fe ³⁺	Fe(NO ₃) ₂	0.5	98 ± 3	97 ± 3
Mn ²⁺	Mn(NO ₃) ₂	0.5	99 ± 1	98 ± 3
Zn ²⁺	Zn(NO ₃) ₂	1	95 ± 2	96 ± 2
Ni ²⁺	Ni(NO ₃) ₂	0.2	97 ± 2	98 ± 2
Pb ²⁺	Pb (NO ₃) ₂	0.2	97 ± 1	97 ± 2

3.2.7 Reliability of the method and nanoflowers enrichment application on real samples: To check the reliability of the method, results obtained using certified reference material (CRM) were presented in Table 5. These values were quantitative, and it shows that the presented procedure could be applied for the preconcentration of heavy metal ions in real samples. Our results were compared with similar works in literature. Results comparing our work with similar works was presented in Table 7.

Table 5. Analysis result of certified reference materials (N=3).

		Cr ⁶⁺	Cd ²⁺
Sea Water (SRM)	Certified Value (µg/L)	0.118 ± 0.008	0.0311 ± 0.0019
	Result, µg/mL	0,116 ± 0,008	0.0301 ± 0.0019
	Recovery, %	98.3 ± 0.9	96.8 ± 0.5

Results obtained after the application of nanoflowers for real samples in optimum conditions were presented in Table 6.

Table 6. Cr⁶⁺ and Cd²⁺ levels before and after from enrichment in various samples (N=3)

Ions	Before		After	
	Cr ⁶⁺ , µg/L	Cd ²⁺ , µg/L	Cr ⁶⁺ , µg/L	Cd ²⁺ , µg/L
Sample				
Sea Water	35.0 ± 2.1	2.2 ± 0.1	196 ± 9	622 ± 8
Bottled Water	ND	ND	367 ± 2	618 ± 11
Tap Water	ND	ND	231 ± 6	620 ± 11
Soda	ND	3.1 ± 0.2	262 ± 5	634 ± 9

Enrichment factor was Cr^{6+} and Cd^{2+} was determined as 200 fold and 560 fold, respectively. The method is found to be successful on real samples. The method is rapid as compared with previously reported procedures for the enrichment of heavy metal ions. The method is successfully used in the assessment of the ingredient materials.

Table 7. Works reported in the literature used for the removal of heavy metal ions

Materials	Element	Amount of adsorbent	Time	pH	Apparatus	Ref.
ZnO nanoparticles	Cr^{3+} , Co^{2+} , and Ni^{2+}	0.5 g	1.5 mins - 180 mins	2	UV-Vis	[28]
ZnO nanoflowers	Cd and Pb	0.8 g/L	100 mins	6.0	AAS	[29]
MgO nanoparticles	Cd and Pb	2294 mg/g for Cd(II) and 2614 mg/g for Pb(II)	30 min and 15 min for the adsorption of Cd(II) and Pb(II), respectively	2.0 and 3.0	Voltammetry	[30]
Nano-HAP composites	Cr (VI)	20 mg	10 mins	5.0	FAAS	[31]
Mf (magnetite that the modified with triethylenetetramine)-graphene oxide	Cr(VI) and Cr(III)	50 mg	10 mins and 30 mins of Cr(VI) and Cr(III), respectively	2.0 and 8.0 of Cr(VI) and Cr(III), respectively	FAAS	[32]

4. Conclusions

Today, heavy metal ions threatening the natural water sources. Therefore, reliable, and affordable methods are important to fight against this problem. Nanoparticles may have high adsorption rates due to their structural properties and they can be mass produced using conventional methods. Hence, flower-like Co_3O_4 nanostructures were produced using hydrothermal synthesis method and heavy metal removal rates were checked in this work. Structural characteristics of the nanoflowers were assessed using different microscopic and elemental methods. Methods confirmed that nanoflowers consisted of well-ordered Co_3O_4 crystals which are consisting of Co and O molecules. There was not any contamination related signal in EDS spectra. Co_3O_4 nanoflowers were then used for the recovery of Cr^{6+} and Cd^{2+} heavy metal ions. Numerous factors affecting the recovery of heavy metal ions such as pH, eluent type, eluent concentration, adsorbent amount, solution volume and adsorption duration were studied. The optimum conditions to obtain max recovery rate were determined. It was seen that our nanoparticles managed to remove almost 99.0% of Cr^{6+} and Cd^{2+} heavy metal ions. The case was also tasted in real samples where sea water, bottled water, tap water and soda were used. It was seen that our nanoflowers perform similar characteristics where 99.2% of Cd^{2+} and 98.3% Cr^{6+} heavy metal ions were removed from real samples. Our result indicates that Co_3O_4 nanoflowers exhibit outstanding heavy metal removal performance for Cr^{6+} and Cd^{2+} metal ions. It illustrates that Co_3O_4 nanoflowers have potential to be used as a nanomaterial for the removal of heavy metal ions especially in aqueous media.

Peer-review: Externally peer - reviewed.

Author contributions: Cemile ÖZCAN: Concepting the work, defining experimental procedures, preparation of the manuscript; Nurdan KURNAZ YETİM: Concepting the work, collecting experimental data, data processing, preparation of manuscript; Mumin Mehmet KOÇ: Conceptualization, preparation of manuscript; Elif Aybike BERBEROĞLU: Collecting experimental data, preparation of manuscript.

Conflict of Interest: No conflict of interest was declared by the authors. (Part of the data presented in the manuscript has been presented in an oral presentation at the NEM 2022 (2nd International Conference on Engineering Technologies).

Financial Disclosure: The authors declared that this study has received no financial support.

References

1. Barrak, H., Kriaa, A., Triki, M., M'nif, A., Hamzaoui, A.H.: Study of the Adsorption and Desorption of Zn (II) and Pb (II) on CaF₂ Nanoparticles. *Iran J. Chem. Chem. Eng.* 39, 191–201 (2020)
2. Khan, I., Saeed, K., Khan, I.: *Nanoparticles: Properties, applications and toxicities*, (2019)
3. Luan, L., Tang, B., Liu, Y., Wang, A., Zhang, B., Xu, W., Niu, Y.: Selective capture of Hg(II) and Ag(I) from water by sulfur-functionalized polyamidoamine dendrimer/magnetic Fe₃O₄ hybrid materials. *Sep. Purif. Technol.* 257, 117902 (2021). <https://doi.org/10.1016/j.seppur.2020.117902>
4. Mokarram, M., Saber, A., Obeidi, R.: Effects of heavy metal contamination released by petrochemical plants on marine life and water quality of coastal areas. *Environ. Sci. Pollut. Res.* 28, 51369–51383 (2021). <https://doi.org/10.1007/S11356-021-13763-3/FIGURES/9>
5. Kurnaz Yetim, N., Berberoğlu, E.A., Aslan, N., Koç, M.M., Özcan, C.: Sonochemical removal of Pb (II) ions from the water medium using Bi₂S₃ nanostructures. (2022). <https://doi.org/10.1080/03067319.2022.2088288>
<https://doi.org/10.1080/03067319.2022.2088288>
6. Üner, O., Körükçü, B.C., Özcan, C.: Adsorption application of activated carbon from ripe black locust seed pods for wastewater taken from Ergene River, Turkey. *Int. J. Environ. Anal. Chem.* 1–16 (2021). <https://doi.org/10.1080/03067319.2021.1889533>
7. Ozcan, C., Akozcan, S.: Determination of ni, pb and cd in drinking fountain water in kirkclareli/turkey by faas after preconcentration on quercetin modified using granular activated carbon. *Desalin. Water Treat.* 175, 219–228 (2020). <https://doi.org/10.5004/DWT.2020.24900>
8. Klatt, V., Kunze, J., Timur, I., Filiz Senkal, B., Kaplan, O., Kaya, G., Ozcan, C., Karaaslan, N.M., Yaman, M., Jia, W.-P., Han, D.-M., Gao, T., Li, F., Keshav Krishna, A., Rama Mohan, K., Murthy, N., Sudarshan, V., Zhu, L., Chen, S., Lu, D., Cheng, X.: Synthesis of new polymeric resin and its application in solid phase extraction of copper in water samples using STAT-FAAS. *Atom. Spectrosc.* 30, 191–200 (2009)
9. Hemmati, M., Rajabi, M., Asghari, A.: Magnetic nanoparticle based solid-phase extraction of heavy metal ions: A review on recent advances. *Microchim. Acta* 2018 1853. 185, 1–32 (2018). <https://doi.org/10.1007/S00604-018-2670-4>
10. Roduner, E.: Size matters: Why nanomaterials are different. *Chem. Soc. Rev.* 35, 583–592 (2006). <https://doi.org/10.1039/b502142c>
11. L. Johnston, R.: *Atomic and Molecular Clusters*. Taylor & Francis, London, New York (2002)
12. Aslan, N., Ceylan, B., Koç, M.M., Findik, F.: Metallic nanoparticles as X-Ray computed tomography (CT) contrast agents: A review. *J. Mol. Struct.* 1219, 128599 (2020). <https://doi.org/10.1016/j.molstruc.2020.128599>
13. Singh, M., Manikandan, S., Kumaraguru, A.K.: Nanoparticles: A New Technology with Wide Applications. *Res. J. Nanosci. Nanotechnol.* 1, 1–11 (2011).

<https://doi.org/10.3923/rjnn.2011.1.11>

14. Koç, M.M., Aslan, N., Kao, A.P., Barber, A.H.: Evaluation of X-ray tomography contrast agents: A review of production, protocols, and biological applications. *Microsc. Res. Tech.* 82, (2019). <https://doi.org/10.1002/jemt.23225>
15. Kurnaz Yetim, N., Kurşun Baysak, F., Koç, M.M., Nartop, D.: Characterization of magnetic Fe₃O₄@SiO₂ nanoparticles with fluorescent properties for potential multipurpose imaging and theranostic applications. *J. Mater. Sci. Mater. Electron.* 31, 18278–18288 (2020). <https://doi.org/10.1007/s10854-020-04375-7>
16. Tao, Y., Zhang, C., Lü, T., Zhao, H.: Removal of Pb(II) Ions from Wastewater by Using Polyethyleneimine-Functionalized Fe₃O₄ Magnetic Nanoparticles. *Appl. Sci.* 2020, Vol. 10, Page 948. 10, 948 (2020). <https://doi.org/10.3390/APP10030948>
17. Sivalingam, D., Gopalakrishnan, J.B., Rayappan, J.B.B.: Nanostructured mixed ZnO and CdO thin film for selective ethanol sensing. *Mater. Lett.* 77, 117–120 (2012). <https://doi.org/10.1016/J.MATLET.2012.03.009>
18. Fareed, S., Medwal, R., Vas, J.V., Khan, I.A., Rawat, R.S., Rafiq, M.A.: Tailoring oxygen sensing characteristics of Co₃O₄ nanostructures through Gd doping. *Ceram. Int.* 46, 9498–9506 (2020). <https://doi.org/10.1016/J.CERAMINT.2019.12.211>
19. Karaçam, R., Yetim, N.K., Koç, M.M.: Structural and Magnetic Investigation of Bi₂S₃@Fe₃O₄ Nanocomposites for Medical Applications. *J. Supercond. Nov. Magn.* 33, 2715–2725 (2020)
20. Kurnaz Yetim, N., Aslan, N., Sarioğlu, A., Sarı, N., Koç, M.M., Yetim, N.K., Aslan, N., Sarioğlu, A., Sarı, N., Koç, M.M.: Structural, electrochemical and optical properties of hydrothermally synthesized transition metal oxide (Co₃O₄, NiO, CuO) nanoflowers. *J. Mater. Sci. Mater. Electron.* 31, 12238–12248 (2020). <https://doi.org/10.1007/s10854-020-03769-x>
21. Liu, S., Zhang, R., Lv, W., Kong, F., Wang, W.: Controlled Synthesis of Co₃O₄ Electrocatalysts with Different Morphologies and Their Application for Oxygen Evolution Reaction. *Int. J. Electrochem. Sci.* 13, 3843–3854 (2018). <https://doi.org/10.20964/2018.04.54>
22. Ince, M., Kaplan, O., Yaman, M.: Solid-Phase Extraction and Preconcentration of Copper in Mineral Waters with 4-(2-Pyridyl-Azo) Resorcinol-Loaded Amberlite XAD-7 and Flame Atomic Absorption Spectrometry. *Water Environ. Res.* 80, 2104–2110 (2008). <https://doi.org/10.2175/106143008X266805>
23. Soylak, M.: Solid Phase Extraction of Cu(II), Pb(II), Fe(III), Co(II), and Cr(III) on Chelex-100 Column Prior to Their Flame Atomic Absorption Spectrometric Determinations. <http://dx.doi.org/10.1081/AL-120034064>. 37, 1203–1217 (2011). <https://doi.org/10.1081/AL-120034064>
24. Tuzen, M., Soylak, M.: Multi-element coprecipitation for separation and enrichment of heavy metal ions for their flame atomic absorption spectrometric determinations. *J. Hazard. Mater.* 162, 724–729 (2009). <https://doi.org/10.1016/J.JHAZMAT.2008.05.087>
25. Soylak, M., Elçi, M.: Solid phase extraction of trace metal ions in drinking water samples from Kayseri-Turkey. *J. TRACE MICROPROBE Tech.* 18, 343–354 (2000). <https://doi.org/10.2/JQUERY.MIN.JS>
26. Ge, M.Y., Han, L.Y., Wiedwald, U., Xu, X.B., Wang, C., Kuepper, K., Ziemann, P., Jiang, J.Z.: Monodispersed NiO nanoflowers with anomalous magnetic behavior Related content Monodispersed NiO nanoflowers with anomalous magnetic behavior. *Nanotechnology.* 21, 5 (2010). <https://doi.org/10.1088/0957-4484/21/42/425702>

27. Bai, G., Dai, H., Deng, J., Liu, Y., Ji, K.: Porous NiO nanoflowers and nanourchins: Highly active catalysts for toluene combustion. *Catal. Commun.* 27, 148–153 (2012). <https://doi.org/10.1016/j.catcom.2012.07.008>
28. Salem, I.A., Salem, M.A., El-Ghobashy, M.A.: The dual role of ZnO nanoparticles for efficient capture of heavy metals and Acid blue 92 from water. *J. Mol. Liq.* 248, 527–538 (2017). <https://doi.org/10.1016/J.MOLLIQ.2017.10.060>
29. Kataria, N., Garg, V.K.: Optimization of Pb (II) and Cd (II) adsorption onto ZnO nanoflowers using central composite design: isotherms and kinetics modelling. *J. Mol. Liq.* 271, 228–239 (2018). <https://doi.org/10.1016/J.MOLLIQ.2018.08.135>
30. Xiong, C., Wang, W., Tan, F., Luo, F., Chen, J., Qiao, X.: Investigation on the efficiency and mechanism of Cd(II) and Pb(II) removal from aqueous solutions using MgO nanoparticles. *J. Hazard. Mater.* 299, 664–674 (2015). <https://doi.org/10.1016/J.JHAZMAT.2015.08.008>
31. Zhan, M., Gao, W., Nguyen, W., Yu, H., Amador, E., Chen, W.: The investigation of triadic silica-supported polyhexamethylene guanidine@nano-hydroxyapatite nanocomposites for Cr (VI) detection. *Mater. Today Adv.* 15, 100268 (2022). <https://doi.org/10.1016/J.MTADV.2022.100268>
32. Islam, A., Ahmad, H., Zaidi, N., Kumar, S.: A graphene oxide decorated with triethylenetetramine-modified magnetite for separation of chromium species prior to their sequential speciation and determination via FAAS. *Microchim. Acta.* 183, 289–296 (2016). <https://doi.org/10.1007/S00604-015-1641-2/TABLES/3>